Contents lists available at ScienceDirect

Comput. Methods Appl. Mech. Engrg.

journal homepage: www.elsevier.com/locate/cma

An arbitrary Lagrangian-Eulerian semi-implicit hybrid method for continuum mechanics with GLM cleaning

S. Busto [a,b]

[a] Departamento de Matemática Aplicada, Lope Gómez de Marzoa s/n, Universidade de Santiago de Compostela, 15782, Santiago de Compostela, Spain
[b] Galician Center for Mathematical Research and Technology, CITMAga, 15782, Santiago de Compostela, Spain

ARTICLE INFO

Keywords:
GPR model for continuum mechanics
Arbitrary Lagrangian-Eulerian methods
Semi-implicit schemes
Hybrid FV/FE methods
Structure preserving
Unstructured grids

ABSTRACT

This paper proposes a novel semi-implicit arbitrary Lagrangian-Eulerian (ALE) method for the solution of the unified Godunov-Peshkov-Romenski (GPR) model of continuum mechanics. To handle the curl-free-type involutions arising in the solid limit of the model, the original system is augmented by adopting a thermodynamically compatible generalized Lagrangian multiplier (GLM) approach. Next, an operator splitting strategy decouples the computation of fast pressure waves from the bulk velocity of the medium yielding a transport subsystem, containing convective terms and non-conservative products, and a Poisson-type subsystem, for the pressure. A second splitting yields an ODE subsystem comprising only the potentially stiff source terms, responsible for the relaxation of the model between its fluid and solid limits.

The mesh motion can be driven by two sources: the local fluid velocity and a prescribed boundary displacement. For the spatial discretisation, we employ unstructured staggered grids, with the pressure defined on the primal mesh and all remaining variables on the dual grid. The transport subsystem is advanced via an explicit finite volume method, in which integration over closed space-time control volumes ensures verification of the geometric conservation law (GCL). On the other hand, implicit continuous finite elements are used for the discretisation of the pressure subsystem and an implicit DIRK scheme is employed to solve the ODE subsystem. Consequently, the proposed approach is well suited to address all Mach number flows. A comprehensive set of benchmarks is employed to assess the accuracy and robustness of the proposed methodology in tackling both fluid and solid mechanics problems.

1. Introduction

The development of a unified first order model for continuum mechanics began more than sixty years ago with the pioneering work of S. Godunov and E. Romenski on the derivation of a hyperbolic model for solid mechanics [1–5]. Contrary to classical Lagrangian descriptions of solids, this hyperbolic model was derived in the Eulerian frame of reference. This approach naturally lent itself to later extensions including heat conduction [6] and fluid dynamics [7]. The resulting system, known as the Godunov-Peshkov-Romenski (GPR) model for continuum mechanics, relies on relaxation parameters to change across a wide range of media, from elastoplasticity to compressible fluids and porus media [8–11]. An important feature of the GPR model is its compliance with the laws of thermodynamics, placing it in the class of thermodynamically compatible models. Further, it enables a connection with Hamiltonian formulations [12]. In this paper, we focus on the numerical solution of the compressible GPR model for fluids and solids given in the

E-mail address: saray.busto.ulloa@usc.es

https://doi.org/10.1016/j.cma.2026.118824
Received 3 December 2025; Received in revised form 19 January 2026; Accepted 8 February 2026
Available online 17 February 2026

Godunov form. Nevertheless, it is important to notice that this modelling framework is well suited to include electromagnetic effects [13,14], and general relativity [15] while recent advances regard modelling of multiphase phenomena [16–21], and reformulations of non-dispersive systems [22].

The hyperbolic nature of the GPR system has motivated the extension of classical methods for conservation laws to its solution. Among the different approaches proposed, we find, e.g., SPH methods [23], finite volume (FV) and discontinuous Galerkin (DG) thermodynamically compatible schemes [24,25], and ADER methods [26–28]. Most available methodologies consider a fully explicit discretisation of the model so the sound velocity appears in the system eigenvalues. This may lead to a restrictive time step condition even for slow bulk velocity phenomena. In this case, to enhance the performance of numerical approximations, a well-established approach coming from fluid dynamics is to apply an operator splitting strategy allowing for the decoupling of the pressure waves computation [29–34]. Then, the use of semi-implicit schemes frees the method from the sharp time step restriction while retaining an explicit scheme for the treatment of convective terms and non-conservative products. Moreover, this methodology eases the verification of the asymptotic-preserving (AP) property in the low Mach number limit. Further details on the development of the so-called all Mach number flow solvers can be found in [35] and references therein. Recently, this methodology has been successfully extended to the GPR model framework, using either Cartesian grids [36,37] or unstructured staggered meshes [38].

The semi-implicit method in [38] is based on the combination of explicit finite volume and implicit continuous finite element methods for the solution of the incompressible and a weakly compressible GPR models. It belongs to a family of hybrid FV/FE approaches formerly employed for the discretisation of diverse hyperbolic systems such as the Navier-Stokes equations [33,39], the shallow water equations [40], and the magnetohydrodynamics equations [41,42]. In this paper, we will also rely on this methodology proposing its extension to the compressible GPR model in the framework of arbitrary Lagrangian-Eulerian (ALE) methods [43]. Analogously to the asymptotic-preserving methods for the compressible Navier-Stokes equations, considering the low Mach limit of the proposed approach yields the incompressible formulation of the GPR model in [38].

Let us note that, up to now, very few approaches have been developed for the GPR model in the Lagrangian [44,45] or ALE frameworks [26]. Nevertheless, Lagrangian schemes are the standard approach in solid mechanics [46,47] and they excel at tracking moving interfaces and contact discontinuities [48–50]. The more recent ALE methodologies can be seen as a flexible extension of Lagrangian methods where the mesh velocity can be defined independently or as a function of the local velocity of the medium reducing mesh distortion [51–54]. These properties make Lagrangian and ALE methods widely employed tools in the context of fluid-structure interaction [55–57] as well. Therefore, the development of ALE schemes for the GPR model offering a good trade-off between accuracy and computational cost would represent a step toward its use in a wide range of practical applications.

When discretizing the GPR model, we should take into account the curl-free-type involution constraints that arise, for the distortion and thermal impulse fields, in the solid limit of the model. To tackle these properties at the discrete level, one possibility is the development of exactly involution preserving schemes, e.g. using an adequate mesh staggering of the discrete operators and conservative variables, as the one proposed in [36,37] for Cartesian staggered grids. A simpler alternative to exact involution preserving methods are divergence and curl correction techniques as the generalized Lagrangian multipliers (GLM) methods devised to approximately address the divergence free condition of the magnetic field in magnetohydrodynamics [41,58]. In this paper, we adopt this latter methodology and propose a novel augmented GLM GPR model grounded on the seminal ideas in [59,60] concerning thermodynamically compatible GLM formulations.

Another crucial aspect of the GPR model regards the stiffness of the source terms involved in the distortion and thermal impulse equations which may lead to stability issues in the visco-plastic limit of the equations. To overcome this problem, a robust strategy, that will be followed in this paper, consists on splitting the system decoupling the source terms computation. The corresponding subsystem, made of ordinary differential equations (ODE), can be then solved employing unconditionally stable implicit methods, thus allowing larger time steps than classical fully explicit approaches, leading to implicit-explicit (IMEX) approaches compatible with the asymptotic limits of the model [44,61].

In light of the discussion above, the main objective of this article is to propose a novel and mathematically well-founded ALE numerical approach for the solution of the complex GPR model on moving unstructured meshes, with potential applications across a wide range of problems in continuum mechanics. The scope of this work includes the introduction of a thermodynamically compatible GLM-augmented GPR formulation for the enforcement of involution constraints, the design of a semi-implicit hybrid scheme consistent with the asymptotic limits of the governing PDE system, the formulation of a space-time ALE discretisation complying with the GCL and the numerical assessment of the accuracy, robustness, and structural properties of the method through standard benchmark problems in fluid and solid mechanics.

The development of this methodology also provides a general framework for the discretisation of other hyperbolic systems that can be cast in the same PDE form and that share all or a subset of the structural properties of the GPR model, such as, for instance, the compressible Navier-Stokes equations. This generality may open a new way to address real-world continuum mechanics problems involving fluids, solids, and their interactions in a unified computational framework.

The rest of this paper is organised as follows. In Section 2, we recall the Godunov-Peshkov-Romenski model for continuum mechanics and introduce a thermodynamically compatible Generalized Lagrangian Multiplier extension allowing for the cleaning of curl errors in the distortion and thermal impulse fields. Section 3 is devoted to the numerical method. We first introduce the operator splitting approach which divides the system into a transport subsystem for the conservative variables and a Poisson type system for the pressure. The unstructured staggered grid spatial discretisation is introduced and the finite volume method for the solution of the transport equations is described. Next, we detail the variational formulation for the discretisation of the pressure system using continuous finite element methods and the interpolation strategies to pass data between the staggered grids. The proposed

methodology is assessed in Section 4 by a wide set of test cases including both fluid dynamics and solid mechanics benchmarks. Finally, the conclusions and an outlook on future research are drawn in Section 5.

2. Governing equations

To address both fluids and solids within a unified partial differential system, we consider the Godunov-Peshkov-Romenski (GPR) model for continuum mechanics [7,27], that, using Einstein notation, reads

$$\frac{\partial}{\partial t}\rho + \frac{\partial}{\partial x_k}\left(\rho u_k\right) = 0, \tag{1a}$$

$$\frac{\partial}{\partial t}\left(\rho u_i\right) + \frac{\partial}{\partial x_k}\left(\rho u_i u_k\right) + \frac{\partial}{\partial x_i}p + \frac{\partial}{\partial x_k}\sigma_{ik} + \frac{\partial}{\partial x_k}\omega_{ik} = \rho g_i, \tag{1b}$$

$$\frac{\partial}{\partial t}A_{ik} + \frac{\partial}{\partial x_k}\left(u_m A_{im}\right) + u_j\frac{\partial}{\partial x_j}A_{ik} - u_j\frac{\partial}{\partial x_k}A_{ij} = -\frac{1}{\theta_1(\tau_1)}E_{A_{ik}}, \tag{1c}$$

$$\frac{\partial}{\partial t}J_k + \frac{\partial}{\partial x_k}\left(J_m u_m\right) + \frac{\partial}{\partial x_k}T + u_j\left(\frac{\partial}{\partial x_j}J_k - \frac{\partial}{\partial x_k}J_j\right) = -\frac{1}{\theta_2(\tau_2)}E_{J_k}, \tag{1d}$$

$$\frac{\partial}{\partial t}(\rho S) + \frac{\partial}{\partial x_k}\left(\rho S u_k\right) + \frac{\partial}{\partial x_k}\left(\rho E_{J_k}\right) = \frac{\rho}{T}\left(\frac{1}{\theta_1(\tau_1)}E_{A_{ik}}E_{A_{ik}} + \frac{1}{\theta_2(\tau_2)}E_{J_k}E_{J_k}\right) \geq 0, \tag{1e}$$

$$\frac{\partial}{\partial t}(\rho E) + \frac{\partial}{\partial x_k}\left(\rho E u_k\right) + \frac{\partial}{\partial x_k}\left(p u_k\right) + \frac{\partial}{\partial x_k}\left(u_i\sigma_{ik}\right) + \frac{\partial}{\partial x_k}\left(u_i\omega_{ik}\right) + \frac{\partial}{\partial x_k}q_k = \rho g_i u_i, \tag{1f}$$

being ρ the density, $\mathbf{u} = \left(u_1, u_2, u_3\right)^T$ the velocity field, p the pressure, $\mathbf{A} = (A_{i,j}) \in \mathcal{M}_{3\times3}$ the distortion field, $\mathbf{J} = \left(J_1, J_2, J_3\right)^T$ the thermal impulse, S the entropy, and E the total energy. The total energy density $\mathcal{E} := \rho E$ can be divided into four terms as

$$\mathcal{E}(\rho, \mathbf{u}, \mathbf{A}, \mathbf{J}, S) = \mathcal{E}_1(\rho, S) + \mathcal{E}_2(\mathbf{u}) + \mathcal{E}_3(\mathbf{A}) + \mathcal{E}_4(\mathbf{J}). \tag{2}$$

The first one corresponds to the internal energy, related to the kinetic energy of the molecular motion. It enables the consideration of different materials depending on the selected equation of state. In case a gas is assumed, the ideal gas equation of state can be employed, then

$$\mathcal{E}_1(\rho, S) = \frac{\rho^\gamma}{(\gamma-1)}e^{\frac{S}{c_v}}, \qquad \mathcal{E}_1(\rho, p) = \frac{p}{\gamma-1} \tag{3}$$

with $\gamma = \dfrac{c_p}{c_v}$ the ratio of specific heat at constant pressure, c_p, and at constant volume, c_v. Further, for liquids and solids undergoing small deformations, we adopt the stiffened gas EOS

$$\mathcal{E}_1(\rho, S) = \frac{c_0^2}{\gamma(\gamma-1)}\left(\frac{\rho}{\rho_0}\right)^{\gamma-1}e^{\frac{S}{c_v}} + \frac{\rho_0 c_0^2 - \gamma p_0}{\gamma\rho}, \qquad \mathcal{E}_1(\rho, p) = \frac{p}{\gamma-1} + \frac{\rho_0 c_0^2 - \gamma p_0}{\gamma(\gamma-1)}, \tag{4}$$

where ρ_0 is the reference material density, p_0 denotes the reference atmospheric pressure, and c_0 refers to the adiabatic soundspeed. More complex relations could be incorporated into the model as, e.g., the Mie-GrÃ¼neisen equation of state for the thermodynamical study of solid materials [28] or the EOS in [62,63] that would provide a hyperbolic model also for large deformations. The second term in (2) corresponds to the kinetic energy per unit volume,

$$\mathcal{E}_2(\mathbf{u}) = \frac{1}{2}\rho|\mathbf{u}|^2. \tag{5}$$

Finally, the third and fourth terms provide the contribution of the mesoscopic, non-equilibrium, part of $\mathcal{E}$ related to the material deformations and the thermal impulse,

$$\mathcal{E}_3(\mathbf{A}) = \frac{1}{4}c_s^2\rho\mathring{G}_{ij}\mathring{G}_{ij}, \qquad \mathcal{E}_4(\mathbf{J}) = \frac{1}{2}c_h^2\rho J_i J_i, \tag{6}$$

where c_s^2 and c_h^2 are the characteristic velocities for propagation of shear and thermal perturbations while $\mathring{G}_{ik}$ denotes the trace-free part of the metric tensor $G_{ik} = A_{ji}A_{jk}$,

$$\mathring{G}_{ik} = G_{ik} - \frac{1}{3}G_{mm}\delta_{ik}. \tag{7}$$

In the momentum Eq. (1b) the viscous and thermal diffusivity effects are taken into account thanks to the non-isotropic part of the stress tensor, containing both shear and thermal stresses,

$$\sigma_{ik} = A_{ji}\partial_{A_{jk}}\mathcal{E} = \rho c_s^2 G_{ij}\mathring{G}_{jk}, \qquad \omega_{ik} = J_i\partial_{J_k}\mathcal{E} = \rho c_h^2 J_i J_k \tag{8}$$

Further,

$$q_k = \partial_{\rho S}\mathcal{E}\partial_{J_k}\mathcal{E} = \rho c_h^2 T J_k \tag{9}$$

denotes the heat flux, with $T := \partial_{\rho S}\mathcal{E}$ the temperature. Finally, the shear and thermal stress relaxation functions read

$$\theta_1(\tau_1) = \frac{1}{3}\rho_0\tau_1 c_s^2 |\mathbf{A}|^{-\frac{5}{3}}, \qquad \theta_2(\tau_2) = \frac{\rho_0 T_0}{T}\tau_2 c_h^2 \tag{10}$$

with τ_1 and τ_2 the corresponding relaxation times, ρ_0, T_0 reference values for the density and the temperature and $|\mathbf{A}|$ the determinant of $\mathbf{A}$. Let us recall that in the stiff limit, i.e., for $\tau_1,\ \tau_2 \to 0$, we retrieve the Navier-Stokes-Fourier equations for fluids with shear viscosity $\mu = \frac{1}{6}\rho_0 c_s^2\tau_1$ and heat conductivity $\kappa = \rho_0 T_0 c_h^2\tau_2$, see [27] for a formal asymptotic analysis of this property.

It is very important to remark that system (1) is an overdetermined system of PDEs where the energy Eq. (1f) can be obtained as the dot product of all other equations by the corresponding main field or thermodynamical dual variables, $\mathbf{p} = \left(r, u_i, \alpha_{ik}, \beta_k, T\right)^T$, $r = \partial_\rho \mathcal{E}$, $u_i = \partial_{\rho u_i}\mathcal{E}$, $\alpha_{ik} = \partial_{A_{ik}}\mathcal{E}$, $\beta_k = \partial_{J_k}\mathcal{E}$, $T = \partial_{\rho S}\mathcal{E}$. Hence, this system belongs to the class of thermodynamically compatible schemes in the sense of Godunov, [1,5].

2.1. Augmented GLM curl cleaning GPR model

A key aspect of the GPR model is that the distortion field, $\mathbf{A}$, and the thermal impulse field, $\mathbf{J}$, are endowed with natural involution constraints of the curl-type. That is, given initially curl-free fields $\mathbf{A}(\mathbf{x},0)$ and $\mathbf{J}(\mathbf{x},0)$ then $\nabla\times\mathbf{A}_i(\mathbf{x},t) = \mathbf{0}$ and $\nabla\times\mathbf{J}(\mathbf{x},t) = \mathbf{0}$ for all $t \in \mathbb{R}^+$. To deal with this structural property several approaches have been proposed in the last decades including the Godunov-Powell approach, [64–67], and exact involution preserving methods [24,68–71]. An alternative successful strategy to address these constraints in an approximated manner consists on the use of the so-called Generalized Lagrangian Multipliers (GLM). Augmented GLM models follow the seminal ideas put forward in [58,72] for the treatment of the divergence free condition of magnetohydrodynamics (MHD) equations. Then, they have been extended to further systems of conservation laws, as in [73] and [59] where GLM curl cleaning approaches have been presented for the FO-CCZ4 formulation of the Einstein field equations and the turbulent shallow water (TSW) model, respectively. Let us remark that these original GLM cleaning approaches often neglected the important thermodynamically compatible property of the underlying systems. Recently, two families of compatible GLM cleaning models have been proposed in [60,74] for the MHD equations. In this work, we follow the approach in [25,59] and introduce a compatible GLM curl cleaning for the GPR model.

It is important to recall that the distortion field, even if written as a matrix, does not correspond to a classical tensor field but to a non-holonomic basis triad, [75]. Consequently, the curl-free property is verified for each matrix column $\mathbf{A}_i$, $i \in \{1,2,3\}$, and we can design a GLM cleaning approach for each of these vector fields instead of considering a complete tensor. Accordingly, we introduce the cleaning fields $\boldsymbol{\varphi}_{\mathbf{A}} = \left(\boldsymbol{\varphi}_{\mathbf{A}_1} \mid \boldsymbol{\varphi}_{\mathbf{A}_2} \mid \boldsymbol{\varphi}_{\mathbf{A}_3}\right)$ and $\boldsymbol{\psi}_{\mathbf{J}}$ with associated cleaning speeds $c_{\mathbf{A}}$, for the distortion field components, and $c_{\mathbf{J}}$, for the heat flux. The equations for the distortion field, the thermal impulse and the corresponding cleaning variables read

$$\frac{\partial}{\partial t}A_{ik} + \frac{\partial}{\partial x_k}\left(u_m A_{im}\right) + u_j\frac{\partial}{\partial x_j}A_{ik} - u_j\frac{\partial}{\partial x_k}A_{ij} + c_{\mathbf{A}}\epsilon_{ijl}\frac{\partial}{\partial x_j}\varphi_{lk} = -\frac{1}{\theta_1(\tau_1)}E_{A_{ik}}, \tag{11}$$

$$\frac{\partial}{\partial t}\varphi_{ik} + u_j\frac{\partial}{\partial x_j}\varphi_{ik} - c_{\mathbf{A}}\epsilon_{ijl}\frac{\partial}{\partial x_j}A_{lk} = 0, \tag{12}$$

$$\frac{\partial}{\partial t}J_k + \frac{\partial}{\partial x_k}\left(J_m u_m\right) + \frac{\partial}{\partial x_k}T + u_j\left(\frac{\partial}{\partial x_j}J_k - \frac{\partial}{\partial x_k}J_j\right) + c_{\mathbf{J}}\epsilon_{kjl}\frac{\partial}{\partial x_j}\psi_l = -\frac{1}{\theta_2(\tau_2)}E_{J_k}, \tag{13}$$

$$\frac{\partial}{\partial t}\psi_k + u_j\frac{\partial}{\partial x_j}\psi_k - c_{\mathbf{J}}\epsilon_{kjl}\frac{\partial}{\partial x_j}J_l = 0 \tag{14}$$

with ϵ_{ijl} the Levi-Civita symbol. We observe that as $c_{\mathbf{A}} \to \infty$ and $c_{\mathbf{J}} \to \infty$, we recover the sought curl-free relations, $\epsilon_{ijl}\frac{\partial}{\partial x_j}A_{lk} = 0$, $\epsilon_{kjl}\frac{\partial}{\partial x_j}J_l = 0$. To ensure thermodynamical compatibility, we need to include the dependence of the total energy on the cleaning primal variables as

$$\mathcal{E} = \rho E = \mathcal{E}_1 + \mathcal{E}_2 + \mathcal{E}_3 + \mathcal{E}_4 + \mathcal{E}_5 + \mathcal{E}_6, \qquad \mathcal{E}_5 = \frac{1}{4}\rho c_s^2 \mathring{D}_{ik}\mathring{D}_{ik}, \qquad \mathcal{E}_6 = \frac{1}{2}\rho c_h^2 \psi_k\psi_k, \tag{15}$$

with $\mathring{D}$ the deviatoric of tensor $D_{ik} = \varphi_{ji}\varphi_{jk}$. Then, the new vector of thermodynamical dual variables, corresponding to the primal variables

$$\mathbf{q}_{GLM} = \left(\rho, \rho u_i, A_{ik}, \varphi_{ik}, J_k, \psi_k, S\right)^T, \tag{16}$$

results

$$\mathbf{p}_{GLM} = \left(r, u_i, \alpha_{ik}, \gamma_{ik}, \beta_k, \xi_k, T\right)^T$$

with

$$\gamma_{ik} = \partial_{\varphi_{ik}}\mathcal{E} = \rho c_s^2 \varphi_{ij}\mathring{D}_{jk}, \qquad \xi_i = \partial_{\psi_i}\mathcal{E} = \rho c_h^2\psi_i. \tag{17}$$

Proposition 2.1. *The augmented GLM curl cleaning GPR model, (1a)–(1b), (11)–(14), (1e), is thermodynamically compatible with the extra energy conservation law*

$$\frac{\partial}{\partial t}\mathcal{E} + \frac{\partial}{\partial x_k}\left(\mathcal{E}u_k\right) + \frac{\partial}{\partial x_k}\left(pu_k\right) + \frac{\partial}{\partial x_k}\left(u_i\sigma_{ik}\right) + \frac{\partial}{\partial x_k}\left(u_i\omega_{ik}\right) + \frac{\partial}{\partial x_k}q_k$$

$$+\rho c_{\mathbf{A}} c_s^2 \epsilon_{ijl}\left(A_{im}\mathring{G}_{mk}\frac{\partial}{\partial x_j}\varphi_{lk}+\varphi_{lm}\mathring{D}_{mk}\frac{\partial}{\partial x_j}A_{ik}\right)+c_{\mathbf{J}}c_h^2\epsilon_{kjl}\left(\rho\psi_l\frac{\partial}{\partial x_j}J_k+\rho J_k\frac{\partial}{\partial x_j}\psi_l\right)=\rho g_i u_i. \tag{18}$$

Proposition 2.2. *Let us first focus in the time derivative and the convective terms but for* $\frac{\partial}{\partial x_k}\left(u_m A_{im}\right)-u_j\frac{\partial}{\partial x_k}A_{ij}$ *and* $\frac{\partial}{\partial x_k}\left(J_m u_m\right)-u_j\frac{\partial}{\partial x_k}J_j$. *Then, taking into account the definition of the new energy (15), we have*

$$\begin{aligned}
&r\left[\frac{\partial}{\partial t}\rho+\frac{\partial}{\partial x_k}\left(\rho u_k\right)\right]+u_i\left[\frac{\partial}{\partial t}\left(\rho u_i\right)+\frac{\partial}{\partial x_k}\left(\rho u_i u_k\right)\right]+\alpha_{ik}\left[\frac{\partial}{\partial t}A_{ik}+u_j\frac{\partial}{\partial x_j}A_{ik}\right]+\gamma_{ik}\left[\frac{\partial}{\partial t}\varphi_{ik}+u_j\frac{\partial}{\partial x_j}\varphi_{ik}\right]\\
&+\beta_k\left[\frac{\partial}{\partial t}J_k+u_j\frac{\partial}{\partial x_j}J_k\right]+\xi_i\left[\frac{\partial}{\partial t}\psi_i+u_k\frac{\partial}{\partial x_k}\psi_i\right]+T\left[\frac{\partial}{\partial t}(\rho S)+\frac{\partial}{\partial x_k}\left(\rho S u_k\right)\right]\\
=\;&\frac{\partial}{\partial t}\mathcal{E}+\partial_\rho\mathcal{E}_1\frac{\partial}{\partial x_k}\left(\rho u_k\right)+\partial_{\rho S}\mathcal{E}_1\frac{\partial}{\partial x_k}(\rho S)+\partial_\rho\mathcal{E}_2\frac{\partial}{\partial x_k}\left(\rho u_k\right)+\partial_{\rho u_i}\mathcal{E}_2\frac{\partial}{\partial x_k}\left(\rho u_i u_k\right)\\
&+\partial_\rho\mathcal{E}_3\frac{\partial}{\partial x_k}\left(\rho u_k\right)+\partial_{A_{ij}}\mathcal{E}_3 u_k\frac{\partial}{\partial x_k}A_{ij}+\partial_\rho\mathcal{E}_4\frac{\partial}{\partial x_k}\left(\rho u_k\right)+\partial_{J_i}\mathcal{E}_4 u_k\frac{\partial}{\partial x_k}J_i+\partial_\rho\mathcal{E}_5\frac{\partial}{\partial x_k}\left(\rho u_k\right)\\
&+\partial_{\varphi_{ij}}\mathcal{E}_5 u_k\frac{\partial}{\partial x_k}\varphi_{ij}+\partial_\rho\mathcal{E}_6\frac{\partial}{\partial x_k}\left(\rho u_k\right)+\partial_{\psi_i}\mathcal{E}_6 u_k\frac{\partial}{\partial x_k}\psi_i\\
=\;&\frac{\partial}{\partial t}\mathcal{E}+\frac{\partial}{\partial x_k}\left[(\mathcal{E}_1+\mathcal{E}_2+\mathcal{E}_3+\mathcal{E}_4)u_k\right]+\partial_\rho\mathcal{E}_5\frac{\partial}{\partial x_k}\left(\rho u_k\right)+\partial_{\varphi_{ij}}\mathcal{E}_5 u_k\frac{\partial}{\partial x_k}\varphi_{ij}+\partial_\rho\mathcal{E}_6\frac{\partial}{\partial x_k}\left(\rho u_k\right)\\
&+\partial_{\psi_i}\mathcal{E}_6 u_k\frac{\partial}{\partial x_k}\psi_i\\
=\;&\frac{\partial}{\partial t}\mathcal{E}+\frac{\partial}{\partial x_k}\left[(\mathcal{E}_1+\mathcal{E}_2+\mathcal{E}_3+\mathcal{E}_4)u_k\right]+\frac{1}{4}c_s^2\mathring{D}_{il}\mathring{D}_{il}\frac{\partial}{\partial x_k}\left(\rho u_k\right)+\rho c_s^2\varphi_{il}\mathring{D}_{lj}u_k\frac{\partial}{\partial x_k}\varphi_{ij}\\
&+\frac{1}{2}c_h^2\psi_i\psi_i\frac{\partial}{\partial x_k}\left(\rho u_k\right)+\rho c_h^2\psi_i u_k\frac{\partial}{\partial x_k}\psi_i\\
=\;&\frac{\partial}{\partial t}\mathcal{E}+\frac{\partial}{\partial x_k}\left[(\mathcal{E}_1+\mathcal{E}_2+\mathcal{E}_3+\mathcal{E}_4)u_k\right]+\frac{\partial}{\partial x_k}\left(\frac{1}{4}\rho c_s^2\mathring{D}_{il}\mathring{D}_{il}u_k\right)+\frac{\partial}{\partial x_k}\left(\frac{1}{2}\rho c_h^2\psi_i\psi_i u_k\right)\\
=\;&\frac{\partial}{\partial t}\mathcal{E}+\frac{\partial}{\partial x_k}\left[(\mathcal{E}_1+\mathcal{E}_2+\mathcal{E}_3+\mathcal{E}_4)u_k\right]+\frac{\partial}{\partial x_k}\left(\mathcal{E}_5 u_k\right)+\frac{\partial}{\partial x_k}\left(\mathcal{E}_6 u_k\right)\\
=\;&\frac{\partial}{\partial t}\mathcal{E}+\frac{\partial}{\partial x_k}\left(\mathcal{E}u_k\right).
\end{aligned} \tag{19}$$

Next, the product of $(\alpha_{ik},\gamma_{ik},\beta_k,\xi_k)$ *by the curl terms in (11)–(14), substitution of* $\alpha_{ik}=\rho c_s^2 A_{ij}\mathring{G}_{jk}$, $\beta_k=\rho c_h^2 J_k$ *and (17), and reordering terms gives*

$$\begin{aligned}
&\alpha_{ik}c_{\mathbf{A}}\epsilon_{ijl}\frac{\partial}{\partial x_j}\varphi_{lk}-\gamma_{ik}c_{\mathbf{A}}\epsilon_{ijl}\frac{\partial}{\partial x_j}A_{lk}+\beta_k c_{\mathbf{J}}\epsilon_{kjl}\frac{\partial}{\partial x_j}\psi_l-\xi_k c_{\mathbf{J}}\epsilon_{kjl}\frac{\partial}{\partial x_j}J_l\\
=\;&\rho c_s^2 A_{im}\mathring{G}_{mk}c_{\mathbf{A}}\epsilon_{ijl}\frac{\partial}{\partial x_j}\varphi_{lk}-\rho c_s^2\varphi_{im}\mathring{D}_{mk}c_{\mathbf{A}}\epsilon_{ijl}\frac{\partial}{\partial x_j}A_{lk}+\rho c_h^2 J_k c_{\mathbf{J}}\epsilon_{kjl}\frac{\partial}{\partial x_j}\psi_l-\rho c_h^2\psi_k c_{\mathbf{J}}\epsilon_{kjl}\frac{\partial}{\partial x_j}J_l\\
=\;&\rho c_s^2 c_{\mathbf{A}}\left(A_{im}\mathring{G}_{mk}\epsilon_{ijl}\frac{\partial}{\partial x_j}\varphi_{lk}-\varphi_{lm}\mathring{D}_{mk}\epsilon_{lji}\frac{\partial}{\partial x_j}A_{ik}\right)+\rho c_h^2 c_{\mathbf{J}}\left(J_k\epsilon_{kjl}\frac{\partial}{\partial x_j}\psi_l-\psi_l\epsilon_{ljk}\frac{\partial}{\partial x_j}J_k\right)\\
=\;&\rho c_s^2 c_{\mathbf{A}}\left(A_{im}\mathring{G}_{mk}\epsilon_{ijl}\frac{\partial}{\partial x_j}\varphi_{lk}+\varphi_{lm}\mathring{D}_{mk}\epsilon_{ijl}\frac{\partial}{\partial x_j}A_{ik}\right)+\rho c_h^2 c_{\mathbf{J}}\left(J_k\epsilon_{kjl}\frac{\partial}{\partial x_j}\psi_l+\psi_l\epsilon_{kjl}\frac{\partial}{\partial x_j}J_k\right)\\
=\;&\rho c_{\mathbf{A}}c_s^2\epsilon_{ijl}\left(A_{im}\mathring{G}_{mk}\frac{\partial}{\partial x_j}\varphi_{lk}+\varphi_{lm}\mathring{D}_{mk}\frac{\partial}{\partial x_j}A_{ik}\right)+c_{\mathbf{J}}c_h^2\rho\epsilon_{kjl}\frac{\partial}{\partial x_j}\left(\psi_l J_k\right).
\end{aligned} \tag{20}$$

The remaining terms exactly correspond to those in the original GPR system and are therefore thermodynamically compatible. We briefly recall their relations. Considering the remaining convective terms of (11) and (13) and the terms on σ_{ik}, ω_{ik}, *it results*

$$u_i\left[\frac{\partial}{\partial x_k}\sigma_{ik}+\frac{\partial}{\partial x_k}\omega_{ik}\right]+\alpha_{ik}\left[\frac{\partial}{\partial x_k}\left(u_m A_{im}\right)-u_j\frac{\partial}{\partial x_k}A_{ij}\right]+\beta_k\left[\frac{\partial}{\partial x_k}\left(J_m u_m\right)-u_j\frac{\partial}{\partial x_k}J_j\right]=\frac{\partial}{\partial x_k}\left(u_i\sigma_{ik}+u_i\omega_{ik}\right). \tag{21}$$

Now, from the temperature term in (13) and the term on $\mathcal{E}_{J_k}$ *in (1e), we get*

$$\beta_k\frac{\partial}{\partial x_k}T+T\frac{\partial}{\partial x_k}\mathcal{E}_{J_k}=\frac{\partial}{\partial x_k}q_k. \tag{22}$$

Finally, the dot product of the source terms multiplied by the corresponding dual variables yields

$$u_i\rho g_i-\alpha_{ik}\frac{1}{\theta_1(\tau_1)}E_{A_{ik}}-\beta_k\frac{1}{\theta_2(\tau_2)}E_{J_k}T\left[\frac{\rho}{T}\left(\frac{1}{\theta_1(\tau_1)}E_{A_{ik}}E_{A_{ik}}+\frac{1}{\theta_2(\tau_2)}E_{J_k}E_{J_k}\right)\right]=u_i\rho g_i. \tag{23}$$

Hence, from (19)–(23), we conclude that the dot product of Eqs. (1a)–(1b), (11)–(14), (1e) by the thermodynamically dual variables $\mathbf{p}_{GLM}$ *yields (18).*

Let us note that the resulting augmented GLM GPR system (1a)–(1b), (11)–(14), (1e), (18) is overdetermined. In what follows, we will address the submodel based on the total energy conservation law,

$$\frac{\partial}{\partial t}\rho + \frac{\partial}{\partial x_k}\left(\rho u_k\right) = 0, \tag{24a}$$

$$\frac{\partial}{\partial t}\left(\rho u_i\right) + \frac{\partial}{\partial x_k}\left(\rho u_i u_k\right) + \frac{\partial}{\partial x_i}p + \frac{\partial}{\partial x_k}\sigma_{ik} + \frac{\partial}{\partial x_k}\omega_{ik} = \rho g_i, \tag{24b}$$

$$\frac{\partial}{\partial t}A_{ik} + \frac{\partial}{\partial x_k}\left(u_m A_{im}\right) + u_j\frac{\partial}{\partial x_j}A_{ik} - u_j\frac{\partial}{\partial x_k}A_{ij} + c_{\mathbf{A}}\epsilon_{ijl}\frac{\partial}{\partial x_j}\varphi_{lk} = -\frac{1}{\theta_1\left(\tau_1\right)}E_{A_{ik}}, \tag{24c}$$

$$\frac{\partial}{\partial t}\varphi_{ik} + u_j\frac{\partial}{\partial x_j}\varphi_{ik} - c_{\mathbf{A}}\epsilon_{ijl}\frac{\partial}{\partial x_j}A_{lk} = 0, \tag{24d}$$

$$\frac{\partial}{\partial t}J_k + \frac{\partial}{\partial x_k}\left(J_m u_m\right) + \frac{\partial}{\partial x_k}T + u_j\left(\frac{\partial}{\partial x_j}J_k - \frac{\partial}{\partial x_k}J_j\right) + c_{\mathbf{J}}\epsilon_{kjl}\frac{\partial}{\partial x_j}\psi_l = -\frac{1}{\theta_2\left(\tau_2\right)}E_{J_k}, \tag{24e}$$

$$\frac{\partial}{\partial t}\psi_k + u_j\frac{\partial}{\partial x_j}\psi_k - c_{\mathbf{J}}\epsilon_{kjl}\frac{\partial}{\partial x_j}J_l = 0, \tag{24f}$$

$$\begin{aligned}&\frac{\partial}{\partial t}\mathcal{E} + \frac{\partial}{\partial x_k}\left(\mathcal{E}u_k\right) + \frac{\partial}{\partial x_k}\left(pu_k\right) + \frac{\partial}{\partial x_k}\left[u_i\left(\sigma_{ik}+\omega_{ik}\right)\right] + \frac{\partial}{\partial x_k}q_k\\ &+\rho c_{\mathbf{A}}c_s^2\epsilon_{ijl}\left(A_{im}\mathring{G}_{mk}\frac{\partial}{\partial x_j}\varphi_{lk} + \varphi_{lm}\mathring{D}_{mk}\frac{\partial}{\partial x_j}A_{ik}\right) + c_{\mathbf{J}}c_h^2\epsilon_{kjl}\left(\rho\psi_l\frac{\partial}{\partial x_j}J_k + \rho J_k\frac{\partial}{\partial x_j}\psi_l\right) = \rho g_i u_i.\end{aligned} \tag{24g}$$

i.e. we neglect the entropy inequality. For thermodynamically compatible methods discretizing the original GPR system containing the entropy relation, we refer to [24,25,76].

3. Numerical discretisation

The discretisation of the GPR system will be performed in the framework of the hybrid finite volume/finite element approach put forward in [77,78] for incompressible flows and then extended to solve the compressible Navier-Stokes equations [33,79], the shallow water equations [80], and the incompressible and weakly compressible GPR model [38]. Further, following the seminal ideas in [43], we propose an extension of the methodology to the arbitrary-Lagrangian-Eulerian framework.

This family of hybrid methods relies on an operator splitting approach which splits the system into a transport subsystem focused on the conservative variables and a Poisson type subsystem for the pressure. Consequently, we decouple the fast moving pressure waves from the bulk velocity of the medium. Then, an explicit discretisation of the transport equations provides an accurate solution of discontinuities while the pressure subsystem can be efficiently solved using an unconditionally stable implicit approach. Hence, the CFL time step condition does not depend on pressure waves that would greatly restrict the time step size. Further, the corresponding semi-discretisation in time verifies the asymptotic-preserving property for decreasing Mach numbers, which would lead to the so called all Mach number methods [29,31].

In what follows, we first present the operator splitting of the augmented GLM GPR model and the overall methodology both in the purely Eulerian framework and in the ALE context. Then, we introduce the spatial discretisation detailing the mesh notation and describe the algorithm's stages.

3.1. Operator splitting and semi-discretisation in time

To ease the presentation of the operator splitting, we first focus on a purely Eulerian approach and introduce a semi-discretisation in time of system (24), yielding

$$\frac{1}{\Delta t}\left(\rho^{n+1}-\rho^n\right) + \frac{\partial}{\partial x_k}\left(\rho u_k^n\right) = 0, \tag{25a}$$

$$\frac{1}{\Delta t}\left(\rho u_i^{n+1}-\rho u_i^n\right) + \frac{\partial}{\partial x_k}\left(\rho u_i^n u_k^n\right) + \frac{\partial}{\partial x_i}p^{n+1} + \frac{\partial}{\partial x_k}\sigma_{ik}^n + \frac{\partial}{\partial x_k}\omega_{ik}^n = \rho^n g_i, \tag{25b}$$

$$\frac{1}{\Delta t}\left(A_{ik}^{n+1}-A_{ik}^n\right) + \frac{\partial}{\partial x_k}\left(u_m^n A_{im}^n\right) + u_j^n\frac{\partial}{\partial x_j}A_{ik}^n - u_j^n\frac{\partial}{\partial x_k}A_{ij}^n + c_{\mathbf{A}}\epsilon_{ijl}\frac{\partial}{\partial x_j}\varphi_{lk}^n = -\frac{1}{\theta_1^n\left(\tau_1\right)}E_{A_{ik}}^n, \tag{25c}$$

$$\frac{1}{\Delta t}\left(\varphi_{ik}^{n+1}-\varphi_{ik}^n\right) + u_j^n\frac{\partial}{\partial x_j}\varphi_{ik}^n - c_{\mathbf{A}}\epsilon_{ijl}\frac{\partial}{\partial x_j}A_{lk}^n = 0, \tag{25d}$$

$$\frac{1}{\Delta t}\left(J_k^{n+1}-J_k^n\right) + \frac{\partial}{\partial x_k}\left(\rho J_m^n u_m^n\right) + \frac{\partial}{\partial x_k}T^n + u_j^n\left(\frac{\partial}{\partial x_j}J_k^n - \frac{\partial}{\partial x_k}J_j^n\right) + c_{\mathbf{J}}\epsilon_{kjl}\frac{\partial}{\partial x_j}\psi_l^n = -\frac{1}{\theta_2^n\left(\tau_2\right)}E_{J_k}^n, \tag{25e}$$

$$\frac{1}{\Delta t}\left(\psi_k^{n+1}-\psi_k^n\right) + u_j^n\frac{\partial}{\partial x_j}\psi_k^n - c_{\mathbf{J}}\epsilon_{kjl}\frac{\partial}{\partial x_j}J_l^n = 0, \tag{25f}$$

$$\begin{aligned}&\frac{1}{\Delta t}\left(\mathcal{E}^n-\mathcal{E}^{n+1}\right) + \frac{\partial}{\partial x_k}\left(\mathcal{E}_1^{n+1}u_k^{n+1}\right) + \frac{\partial}{\partial x_k}\left(\mathcal{E}_2^n u_k^n\right) + \frac{\partial}{\partial x_k}\left(\mathcal{E}_3^n u_k^n\right) + \frac{\partial}{\partial x_k}\left(\mathcal{E}_4^n u_k^n\right) + \frac{\partial}{\partial x_k}\left(\mathcal{E}_5^n u_k^n\right)\\ &+\frac{\partial}{\partial x_k}\left(\mathcal{E}_6^n u_k^n\right) + \frac{\partial}{\partial x_k}\left(p^{n+1}u_k^{n+1}\right) + \frac{\partial}{\partial x_k}\left(u_i^n\sigma_{ik}^n\right) + \frac{\partial}{\partial x_k}\left(u_i^n\omega_{ik}^n\right) + \frac{\partial}{\partial x_k}q_k^n = g_i\rho u_i^n.\end{aligned} \tag{25g}$$

Next, extending the methodology proposed in [33], for solving the compressible Navier-Stokes equations, to the solution of the GPR model, we consider a TV-splitting of the momentum (25b) and energy Eq. (25g), which leads to a transport and a pressure subsystem, [31]. Introducing the intermediate auxiliary variable $\rho\mathbf{u}^*$, we get

$$\frac{1}{\Delta t}\left(\rho u_i^* - \rho^n u_i^n\right) + \frac{\partial}{\partial x_k}\left(\rho^n u_i^n u_k^n\right) + \frac{\partial}{\partial x_i} p^n + \frac{\partial}{\partial x_k}\sigma_{ik}^n + \frac{\partial}{\partial x_k}\omega_{ik}^n = \rho^n g_i, \tag{26}$$

$$\frac{1}{\Delta t}\left(\rho^{n+1} u_i^{n+1} - \rho u_i^*\right) + \frac{\partial}{\partial x_i}\left(p^{n+1} - p^n\right) = 0. \tag{27}$$

Hence, the momentum at the new time step can be computed from

$$\rho u_k^{n+1} = \rho u_k^* - \Delta t \frac{\partial}{\partial x_k}\delta p^{n+1}, \qquad \delta p^{n+1} = p^{n+1} - p^n, \tag{28}$$

once the transport-diffusion Eq. (26) is solved.

Similarly, focusing on the energy equation, (25g), decomposing the energy density within the flux term into its six components and introducing the intermediate auxiliary energy density $\mathcal{E}^*$, we obtain

$$\begin{aligned}&\frac{1}{\Delta t}\left(\mathcal{E}^* - \mathcal{E}^n\right) + \frac{\partial}{\partial x_k}\left(\mathcal{E}_2^n u_k^n\right) + \frac{\partial}{\partial x_k}\left(\mathcal{E}_3^n u_k^n\right) + \frac{\partial}{\partial x_k}\left(\mathcal{E}_4^n u_k^n\right) + \frac{\partial}{\partial x_k}\left(\mathcal{E}_5^n u_k^n\right) + \frac{\partial}{\partial x_k}\left(\mathcal{E}_6^n u_k^n\right)\\ &+\frac{\partial}{\partial x_k}\left(u_i^n \sigma_{ik}^n\right) + \frac{\partial}{\partial x_k}\left(u_i^n \omega_{ik}^n\right) + \frac{\partial}{\partial x_k} q_k^n = g_i \rho u_i^n,\end{aligned} \tag{29}$$

$$\frac{1}{\Delta t}\left(\mathcal{E}^{n+1} - \mathcal{E}^*\right) + \frac{\partial}{\partial x_k}\left(\mathcal{E}_1^{n+1} u_k^{n+1}\right) + \frac{\partial}{\partial x_k}\left(p^{n+1} u_k^{n+1}\right) = 0. \tag{30}$$

Therefore, from (30),

$$\mathcal{E}^{n+1} = \mathcal{E}^* - \Delta t \frac{\partial}{\partial x_k}\left(\mathcal{E}_1^{n+1} u_k^{n+1}\right) - \Delta t \frac{\partial}{\partial x_k}\left(p^{n+1} u_k^{n+1}\right) \tag{31}$$

with $\mathcal{E}^*$ the solution of (29). Substituting the expression for $\mathcal{E}_1$ in terms of the pressure and gathering terms yields

$$\mathcal{E}^{n+1} = \mathcal{E}^* - \Delta t \frac{\partial}{\partial x_k}\left(h^{n+1} \rho u_k^{n+1}\right), \tag{32}$$

where the enthalpy reads

$$h = \frac{\gamma}{\rho(\gamma - 1)} p \tag{33}$$

if the ideal gas EOS (3) is employed. Meanwhile, for the stiffened gas EOS (4), we have

$$h = \frac{\gamma p + \rho_0 c_0^2 - \gamma p_0}{\rho(\gamma - 1)}. \tag{34}$$

Taking into account (2), the energy equation is then rewritten in terms of the pressure unknown as

$$\frac{p^{n+1}}{(\gamma - 1)} - \frac{p^n}{(\gamma - 1)} = -\mathcal{E}_1^n - \mathcal{E}_2^{n+1} - \mathcal{E}_3^{n+1} - \mathcal{E}_4^{n+1} - \mathcal{E}_5^{n+1} - \mathcal{E}_6^{n+1} + \mathcal{E}^* - \Delta t \frac{\partial}{\partial x_k}\left(h^{n+1} \rho u_k^{n+1}\right), \tag{35}$$

where we have subtracted the term $\mathcal{E}_1$ at the two sides of (32). Finally, substitution of (28) yields the pressure equation

$$\begin{aligned}\frac{1}{(\gamma - 1)}\delta p^{n+1} \quad &-\Delta t^2 \frac{\partial}{\partial x_k}\left(h^{n+1} \frac{\partial}{\partial x_k}\delta p^{n+1}\right) = \mathcal{E}^* - \mathcal{E}_1^n - \mathcal{E}_2^{n+1} - \mathcal{E}_3^{n+1} - \mathcal{E}_4^{n+1} - \mathcal{E}_5^{n+1}\\ &-\mathcal{E}_6^{n+1} - \Delta t \frac{\partial}{\partial x_k}\left(h^{n+1} \rho u_k^*\right)\end{aligned} \tag{36}$$

whose solution is employed in (28) and (31) to obtain the momentum and total energy at the new time step.

The highly nonlinear system (36) involves the term $\mathcal{E}_1^{n+1} = \frac{1}{2}\rho^{n+1}\left|\mathbf{u}^{n+1}\right|^2$ so it cannot be solved independently of (28), i.e., the system to be solved involves (25a), (26), (25c)–(25f), (36), (29), (28), (31). To deal with these crossed p^{n+1} and $\rho\mathbf{u}^{n+1}$ terms and with the non linearity introduced by the presence of the enthalpy in the stiffness matrix, we apply a Picard procedure getting the final system

$$\rho^{n+1} = \rho^n - \Delta t \frac{\partial}{\partial x_k}\left(\rho u_k^n\right), \tag{37a}$$

$$\rho u_i^* = \rho u_i^n - \Delta t \left(\frac{\partial}{\partial x_k}\left(\rho^n u_i^n u_k^n\right) + \frac{\partial}{\partial x_i} p^n + \frac{\partial}{\partial x_k}\sigma_{ik}^n + \frac{\partial}{\partial x_k}\omega_{ik}^n - \rho^n g_i\right), \tag{37b}$$

$$A_{ik}^{n+1} = A_{ik}^n - \Delta t \left(\frac{\partial}{\partial x_k}\left(u_m^n A_{im}^n\right) + u_j^n \frac{\partial}{\partial x_j} A_{ik}^n - u_j^n \frac{\partial}{\partial x_k} A_{ij}^n + c_{\mathbf{A}} \epsilon_{ijl} \frac{\partial}{\partial x_j}\varphi_{lk}^n + \frac{1}{\theta_1^n(\tau_1)} E_{A_{ik}}^n\right), \tag{37c}$$

$$\varphi_{ik}^{n+1} = \varphi_{ik}^n - \Delta t \left(u_j^n \frac{\partial}{\partial x_j}\varphi_{ik}^n - c_{\mathbf{A}} \epsilon_{ijl} \frac{\partial}{\partial x_j} A_{lk}^n\right), \tag{37d}$$

$$J_k^{n+1} = J_k^n - \Delta t \left(\frac{\partial}{\partial x_k}\left(J_m^n u_m^n\right) + u_j \left(\frac{\partial}{\partial x_j} J_k^n - \frac{\partial}{\partial x_k} J_j^n \right) + \frac{\partial}{\partial x_k} T^n + c_{\mathbf{J}} \epsilon_{kjl} \frac{\partial}{\partial x_j} \psi_l^n + \frac{1}{\theta_2^n(\tau_2)} E_{J_k}^n \right), \tag{37e}$$

$$\psi_k^{n+1} = \psi_k^n - \Delta t \left(u_j^n \frac{\partial}{\partial x_j} \psi_k^n - c_{\mathbf{J}} \epsilon_{kjl} \frac{\partial}{\partial x_j} J_l^n \right), \tag{37f}$$

$$\mathcal{E}^* = \mathcal{E}^n - \Delta t \Bigg(\frac{\partial}{\partial x_k}\left(\mathcal{E}_2^n u_k^n\right) + \frac{\partial}{\partial x_k}\left(\mathcal{E}_3^n u_k^n\right) + \frac{\partial}{\partial x_k}\left(\mathcal{E}_4^n u_k^n\right) + \frac{\partial}{\partial x_k}\left(\mathcal{E}_5^n u_k^n\right) + \frac{\partial}{\partial x_k}\left(\mathcal{E}_6^n u_k^n\right)$$
$$+ \frac{\partial}{\partial x_k}\left[u_i^n\left(\sigma_{ik}^n + \omega_{ik}^n\right)\right] + \frac{\partial}{\partial x_k} q_k^n - g_i \rho u_i^n \Bigg), \tag{37g}$$

$$\frac{\delta p^{n+1,\ell+1}}{\gamma - 1} - \Delta t^2 \frac{\partial}{\partial x_k}\left(h^{n+1,\ell} \frac{\partial}{\partial x_k} \delta p^{n+1,\ell+1} \right) = \mathcal{E}^* - \mathcal{E}_1^n - \mathcal{E}_2^{n+1,\ell} - \mathcal{E}_3^{n+1}$$
$$- \mathcal{E}_4^{n+1} - \mathcal{E}_5^{n+1} - \mathcal{E}_6^{n+1} - \Delta t \frac{\partial}{\partial x_k}\left(h^{n+1,\ell} \rho u_k^*\right), \tag{37h}$$

$$\rho u_k^{n+1,\ell+1} = \rho u_k^* - \Delta t \frac{\partial}{\partial x_k} \delta p^{n+1,\ell+1}, \tag{37i}$$

$$\mathcal{E}^{n+1} = \mathcal{E}^* - \Delta t \frac{\partial}{\partial x_k}\left(h^{n+1,\ell+1} \rho u_k^{n+1,\ell+1} \right) \tag{37j}$$

with ℓ the Picard iteration index, $\ell = 1, \dots, N_{\text{Pic}}$ and

$$p^{n+1,\ell+1} = p^n + \delta p^{n+1,\ell+1}, \tag{38}$$

needed to compute $h^{n+1,\ell+1}$. Note that the Picard iteration does not affect the computation of the terms related to the distortion field and the thermal impulse in (37h) since their value at the new time step is directly obtained from (37c)–(37f).

Besides, the source terms related to the distortion tensor and thermal impulse may become very stiff, so employing an explicit approach for their discretisation may require very small time steps. To circumvent this issue, we split (11) and (13) into two subsystems [38,44]. The first one accounts for the contributions of the flux term and the non-conservative products,

$$A_{ik}^* = A_{ik}^n - \Delta t \left(\frac{\partial}{\partial x_k}\left(u_m^n A_{im}^n\right) + u_j^n \frac{\partial}{\partial x_j} A_{ik}^n - u_j^n \frac{\partial}{\partial x_k} A_{ij}^n + c_{\mathbf{A}} \epsilon_{ijl} \frac{\partial}{\partial x_j} \varphi_{lk}^n \right), \tag{39}$$

$$J_k^* = J_k^n - \Delta t \left(\frac{\partial}{\partial x_k}\left(J_m^n u_m^n\right) + \frac{\partial}{\partial x_k} T^n + u_j^n \left(\frac{\partial}{\partial x_j} J_k^n + \frac{\partial}{\partial x_k} J_j^n \right) + c_{\mathbf{J}} \epsilon_{kjl} \frac{\partial}{\partial x_j} \psi_l^n \right). \tag{40}$$

Meanwhile, the second subsystem contains only the algebraic source terms and can be implicitly discretized:

$$\frac{1}{\Delta t}\left(A_{ik}^{n+1} - A_{ik}^*\right) = -\frac{1}{\theta_1^{n+1}(\tau_1)} E_{A_{ik}}^{n+1}, \tag{41a}$$

$$\frac{1}{\Delta t}\left(J_k^{n+1} - J_k^*\right) = -\frac{1}{\theta_2^{\star}(\tau_2)} E_{J_k}^{n+1}. \tag{41b}$$

3.1.1. Eulerian hybrid FV/FE method

Attending to the different nature of the equations on (37), we split the Eulerian hybrid finite volume/finite element algorithm into four main stages:

1. Transport stage. A finite volume method is employed to solve system (37a)–(37g) yielding the solution at the new time step for the density, distortion and thermal impulse fields, ρ^{n+1}, $\mathbf{A}^{n+1}$, $\mathbf{J}^{n+1}$, and intermediate values for the momentum and total energy unknowns, $\rho\mathbf{u}^*$, $\mathcal{E}^*$. In case the GLM GPR model is solved, also the cleaning variables are computed at this stage, $\boldsymbol{\varphi}_{\mathbf{A}}^{n+1}$, $\boldsymbol{\psi}_{\mathbf{J}}^{n+1}$.
2. Intermediate stage. The intermediate values obtained for the momentum and total energy are interpolated between the staggered grids allowing for the computation of the source terms in the next stage.
3. Pressure stage. A Picard iteration procedure is employed to approximate the pressure at the new time step, p^{n+1}. Within each Picard iteration a $\mathbb{P}^1$ implicit finite element method is applied to solve (37h). Then, the enthalpy and momentum unknowns are updated following (34) and (37i), getting $h^{n+1,\ell+1}$ and $\rho\mathbf{u}^{n+1,\ell+1}$, that allows the computation of $\mathcal{E}_2^{n+1,\ell+1}$.
4. Correction stage. Once the final momentum, $\rho\mathbf{u}^{n+1}$, is calculated substituting the pressure correction δp^{n+1} in (37i), the obtained velocity is employed in (37j) to get the total energy at time t^{n+1}, $\mathcal{E}^{n+1}$.

A detailed description of each of these stages will be provided in Sections 3.4–3.7.

3.1.2. Extension to the ALE framework

The former methodology assumes a purely Eulerian framework. In order to deal also with small geometry deformations, we extend the hybrid approach to the context of Arbitrary-Lagrangian-Eulerian methods. Following [43], we introduce a new stage at the beginning of each time step:

0. Mesh motion stage. In this stage, we move the mesh attending to the local fluid velocity at the previous time step, $\mathbf{u}^n$. Further, the mesh may also be reshaped attending to prescribed displacements of the boundaries of the computational domain.

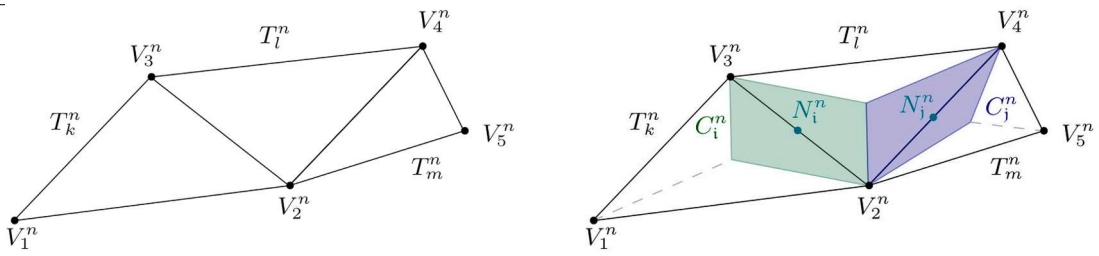

Fig. 1. Construction of two interior dual elements C_{i} and C_{j} from primal elements T_k, T_l, T_m.

Next, in the transport stage, we consider the space-time divergence form of the transport equations which are integrated over space-time control volumes. As a result, the intermediate approximations reside on the deformed mesh. Then, the remaining stages can be performed as for the purely Eulerian method only considering the new grid configuration.

3.2. Spatial discretisation: Staggered unstructured grids

For the discretisation of the spatial domain Ω, we employ unstructured staggered grids of the face type, [77,81,82], also known as diamond grids. We consider a primal mesh made of non-overlapping triangles in 2D and tetrahedra in 3D denoted by T_k, $k = 1, \dots, N_{\mathrm{el}}$, $\Omega = \bigcup_k T_k$. Focusing on one interior edge/face of the domain, Γ_i, we can compute the barycentres, B_{i_L}, B_{i_R}, of the two neighbouring primal elements related to the edge/face and construct a dual cell C_{i} by merging the two subtriangles/subtetrahedra with vertex each of the barycentres and the vertex of Γ_i. Similarly, for a boundary edge/face, we construct a boundary dual cell as the subelement with vertex those of Γ_i and the barycentre of the related primal element. A sketch on the dual mesh construction in 2D is provided in Fig. 1. Further details on the staggered grid generation can be found in [33,77].

To describe the proposed hybrid methodology, we furthermore need to introduce the following notation related to the mesh:

- V_j, $j \in \{1, \dots, N_{\mathrm{ver}}\}$, are the vertex of the primal grid, N_{ver} the total number of vertex.
- $|T_k|$ is the area/volume of the primal element T_k.
- $\mathcal{K}_k$ is the set of indexes of primal elements adjacents to T_k.
- Γ_{kl} is the boundary shared by the primal elements T_k and T_l.
- $\boldsymbol{n}_{kl}$ is the unit normal vector of Γ_{kl} exterior to T_k.
- $\boldsymbol{\eta}_{kl}$ is the normal vector of Γ_{kl} exterior to T_k and weighted the length/area of Γ_{kl}, $\|\boldsymbol{\eta}_{kl}\|$.
- $\hat{\mathcal{K}}_k$ is the set of indexes of dual cells generated using T_k.
- $|T_{k\mathrm{i}}|$ is the area/volume of the intersection of T_k with C_{i}.
- $\hat{\mathcal{K}}_{\mathrm{i}}$ is the set of indexes of primal elements generating the dual cell C_{i}.
- N_{i}, $\mathrm{i} \in \{1, \dots, N_{\mathrm{cell}}\}$, are the vertex of the primal grid, N_{cell} the total number of dual cells.
- $|C_{\mathrm{i}}|$ is the area/volume of C_{i}.
- $\mathcal{K}_{\mathrm{i}}$ is the set of indexes of dual elements adjacents to cell C_{i}.
- $\mathrm{i} = \partial C_{\mathrm{i}} = \bigcup_{\mathrm{j} \in \mathcal{K}_{\mathrm{i}}} \mathrm{ij}$ is the boundary of C_{i} and ij represents the edge/face shared with cell C_{j}.
- $\boldsymbol{n}_{\mathrm{ij}}$ is the outward unit normal vector of ij.
- $\boldsymbol{\eta}_{\mathrm{ij}}$ is the outward normal vector of ij exterior to C_{i} weighted with the length/area of ij, $\|\boldsymbol{\eta}_{\mathrm{ij}}\|$.
- $C_{\mathrm{i}}^\circ = \partial C_{\mathrm{i}} \setminus \mathrm{i}$ is the interior of C_{i}.

On the other hand, the ALE approach, at each time step, requires the update of the coordinates of the primal and dual grids as well as related data; e.g. areas, volumes and boundary normals. It is important to remark that topology changes are not allowed so the connectivities of the mesh structures do not change. Thus, the work load lowers with respect to the generation of a completely new mesh in the modified computational domain. For alternative ALE approaches allowing large deformations and topology changes without the need of remeshing the whole domain, we refer to [83,84].

Given a dual cell at two subsequent time steps, C_{i}^n and C_{i}^{n+1}, we design a space-time control volume $\widetilde{C}_{\mathrm{i}}$ joining the vertex of each dual element at both times so $\widetilde{C}_{\mathrm{i}}|_n = C_{\mathrm{i}}^n$ and $\widetilde{C}_{\mathrm{i}}|_{n+1} = C_{\mathrm{i}}^{n+1}$. This control volume, depicted in Fig. 2, will be then employed within the transport stage to solve the transport subsystem. Analogously with the notation of steady grids, we label $\widetilde{N}_{\mathrm{i}}$, $\widetilde{\Gamma}_{\mathrm{i}} = \partial\widetilde{C}_{\mathrm{i}}$ and $\widetilde{C}_{\mathrm{i}}^\circ = \partial\widetilde{C}_{\mathrm{i}} \setminus \widetilde{\Gamma}_{\mathrm{i}}$ the node, the boundary and the interior of $\widetilde{C}_{\mathrm{i}}$, respectively. Further, the space-time faces of the control volumes located between two neighbouring elements $\widetilde{C}_{\mathrm{i}}$ and $\widetilde{C}_{\mathrm{j}}$ are denoted by $\widetilde{\Gamma}_{\mathrm{ij}}$ and its corresponding outward unit normal with respect to $\widetilde{C}_{\mathrm{i}}$ is $\widetilde{\boldsymbol{n}}_{\mathrm{ij}} = (\widetilde{n}_t, \widetilde{\boldsymbol{n}}_{\boldsymbol{x}})$. Consequently, we have

$$\widetilde{\Gamma}_i = C_{\mathrm{i}}^n \cup \left(\bigcup_{\mathrm{j} \in \mathcal{K}_{\mathrm{i}}} \widetilde{\Gamma}_{\mathrm{ij}} \right) \cup C_{\mathrm{i}}^{n+1} \tag{42}$$

and the outward pointing unit normal vectors to C_{i}^n and C_{i}^{n+1} are $\widetilde{\boldsymbol{n}} = (-1, \boldsymbol{0})$ and $\widetilde{\boldsymbol{n}} = (1, \boldsymbol{0})$, respectively.

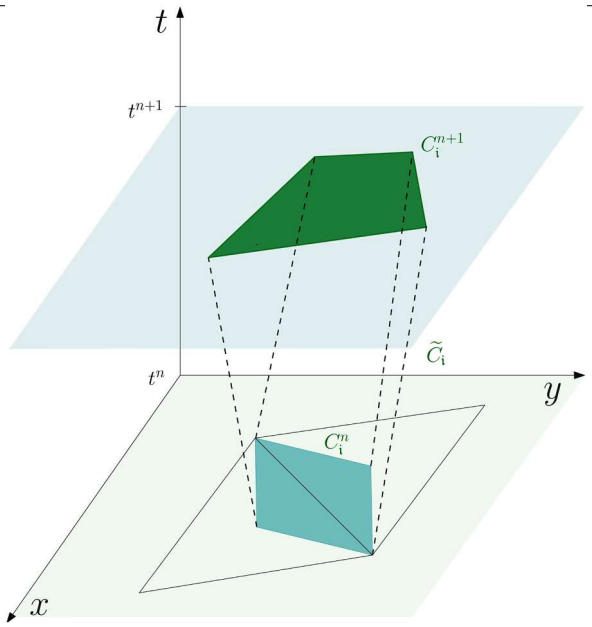

Fig. 2. Construction of a space-time control volume $\widetilde{C}_i$ generated by the deformation of the dual cell C_i between times t^n and t^{n+1}. C_i^n and C_i^{n+1} are shadowed in green while the space time boundary is indicated with dashed lines. The black triangles at time t^n plane correspond to the primal elements generating the dual cell C_i^n. (For interpretation of the references to colour in this figure legend, the reader is referred to the web version of this article.)

Besides, the space-time faces $\widetilde{\Gamma}_{ij}$ can be mapped into a reference element in a local coordinate system. For instance, in the bidimensional case, we consider the coordinate system $\chi - \tau$ with basis functions $\widetilde{\Phi}_\ell = \widetilde{\Phi}_\ell(\chi, \tau)$ given by

$$\widetilde{\Phi}_1 = (1-\chi)(1-\tau), \quad \widetilde{\Phi}_2 = \chi(1-\tau), \quad \widetilde{\Phi}_3 = (1-\chi)\tau, \quad \widetilde{\Phi}_4 = \chi\tau, \qquad 0 \le \chi \le 1, \quad 0 \le \tau \le 1. \tag{43}$$

Then, denoting $\widetilde{\mathbf{X}}_\ell$ the space-time coordinate vectors of the four vertices which form the face,

$$\widetilde{\mathbf{X}}_1 = (t^n, \mathbf{X}_1^n) = (t^n, x_1, y_1), \qquad \widetilde{\mathbf{X}}_2 = (t^n, \mathbf{X}_2^n) = (t^n, x_2, y_2),$$
$$\widetilde{\mathbf{X}}_3 = (t^{n+1}, \mathbf{X}_2^{n+1}) = (t^{n+1}, x_3, y_3), \qquad \widetilde{\mathbf{X}}_4 = (t^{n+1}, \mathbf{X}_1^{n+1}) = (t^{n+1}, x_4, y_4),$$

we define the map from the reference configuration to $\widetilde{\Gamma}_{ij}$ as

$$\widetilde{\mathbf{x}}_{ij}(\chi, \tau) = \widetilde{\Phi}_1 \widetilde{\mathbf{X}}_1 + \widetilde{\Phi}_2 \widetilde{\mathbf{X}}_2 + \widetilde{\Phi}_3 \widetilde{\mathbf{X}}_3 + \widetilde{\Phi}_4 \widetilde{\mathbf{X}}_4,$$

see Fig. 3. Furthermore, the space-time unit normal vector on the space-time face $\widetilde{\Gamma}_{ij}$ reads

$$\widetilde{\boldsymbol{n}}_{ij} = (\tilde{n}_{ij}^t, \tilde{n}_{ij}^x, \tilde{n}_{ij}^y) = \frac{\left(\frac{\partial \widetilde{\mathbf{x}}}{\partial \chi} \times \frac{\partial \widetilde{\mathbf{x}}}{\partial \tau}\right)}{\left\| \frac{\partial \widetilde{\mathbf{x}}}{\partial \chi} \times \frac{\partial \widetilde{\mathbf{x}}}{\partial \tau} \right\|}.$$

Then, denoting its integral

$$\widetilde{\boldsymbol{\eta}}_{ij} := \int_{\widetilde{\Gamma}_{ij}} \widetilde{\boldsymbol{n}}_{ij} \, \mathrm{dt} \, \mathrm{dS}, \tag{44}$$

we observe that

$$\int_{\widetilde{\Gamma}_i} \widetilde{\boldsymbol{n}} \, \mathrm{dS} = \sum_{j \in \mathcal{K}_i} \widetilde{\boldsymbol{\eta}}_{ij} = 0, \tag{45}$$

i.e. the geometric conservation law (GCL) [85] will be verified when using closed space-time control volumes for the integration of the equations at each time step [52,86].

3.3. Mesh motion

Given a vertex on the primal grid at time t^n, $\mathbf{X}_\ell^n$, we compute its position at the new time step $\mathbf{X}_\ell^{n+1}$ as

$$\mathbf{X}_\ell^{n+1} = \mathbf{X}_\ell^n + \Delta t \, \mathbf{V}_\ell^n \tag{46}$$

with $\mathbf{V}_\ell^n$ the mesh velocity. This velocity can be set in two different ways:

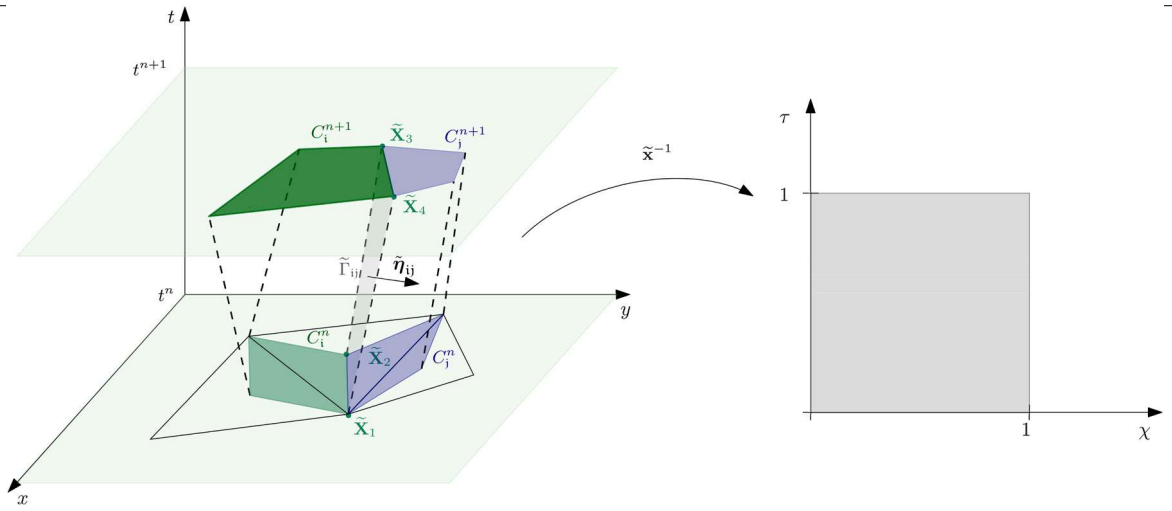

Fig. 3. Map of a space-time face $\widetilde{\Gamma}_{ij}$ to the reference element in the local coordinate system $\chi - \tau$. The face $\widetilde{\Gamma}_{ij}$ (shadowed in gray) shared by the space-time control volumes $\widetilde{C}_i$ and $\widetilde{C}_j$ is determined by vertex $\widetilde{\mathbf{X}}_1$, $\widetilde{\mathbf{X}}_2$, $\widetilde{\mathbf{X}}_3$ and $\widetilde{\mathbf{X}}_4$.

- According to a prescribed boundary velocity, $\mathbf{V}^n_{BC}$. Assuming that we have the description of the boundary motion, the mesh displacement at the interior of the domain is computed by solving a Laplace equation on the velocity with Dirichlet boundary conditions,

$$\begin{cases} \nabla^2 \mathbf{V}^n = 0, & \forall \mathbf{X} \in \Omega^n, \\ \mathbf{V}^n(\mathbf{X}) = \mathbf{V}^n_{BC}, & \forall \mathbf{X} \in \partial\Omega^n. \end{cases} \tag{47}$$

- As a smoothed local fluid velocity. Since we are working in the ALE framework, we can arbitrarily choose the mesh velocity. For instance, we can set it to match the local fluid velocity, as in classical Lagrangian schemes, or apply a smoothing operator in order to reduce mesh distortion at the interior of the computational domain [83,86]. Accordingly, we define a regularization parameter $\zeta \in [0, \infty)$ and compute the mesh velocity solving

$$\begin{cases} \mathbf{V}^n(\mathbf{X}) - \Delta t\, \zeta \nabla^2 \mathbf{V}^n(\mathbf{X}) = \mathbf{u}^n, & \forall \mathbf{X} \in \Omega^n, \\ \mathbf{V}^n(\mathbf{X}) = \mathbf{u}^n_{BC}, & \forall \mathbf{X} \in \partial\Omega^n, \end{cases} \tag{48}$$

  at the aid of $\mathbb{P}^1$ continuous finite element methods. Following this approach, for $\zeta = 0$ we retrieve the pure Lagrangian scheme while as $\zeta \to \infty$ we have a Laplacian smoothing of the mesh velocity.

Let us note that, as it will be seen in the numerical results section, both types of motion may be combined by setting some of the boundaries to have a specific boundary velocity while others freely move with the local fluid velocity. This methodology allows, e.g., for the simulation of free surface flows in confined moving domains. Further details on the mesh motion within the hybrid FV/FE methodology can be found in [43].

3.4. Transport stage: A finite volume scheme on the space-time divergence form of the transport subsystem

The transport subsystem (37a)–(37g) is solved at the aid of an explicit finite volume method. Introducing the vector of conservative variables $\mathbf{Q} = \left(\rho, \mathbf{u}, \mathbf{A}, \boldsymbol{\varphi}_{\mathbf{A}}, \mathbf{J}, \boldsymbol{\psi}_{\mathbf{J}}, \mathcal{E}\right)^T$, the continuous counterpart of the transport equations can be recast into a general system of the form

$$\partial_t \mathbf{Q} + \nabla \cdot \boldsymbol{\mathcal{F}}(\mathbf{Q}) + \boldsymbol{\mathcal{B}}(\mathbf{Q}) \cdot \nabla \mathbf{Q} = \boldsymbol{\mathcal{S}}(\mathbf{Q}), \tag{49}$$

with $\boldsymbol{\mathcal{F}}(\mathbf{Q})$ the convective flux terms, $\boldsymbol{\mathcal{B}}(\mathbf{Q}) \cdot \nabla \mathbf{Q}$ the non-conservative products, and $\boldsymbol{\mathcal{S}}(\mathbf{Q})$ the source terms. Hence, its space-time divergence formulation reads

$$\widetilde{\nabla} \cdot \widetilde{\boldsymbol{\mathcal{F}}}(\mathbf{Q}) + \widetilde{\boldsymbol{\mathcal{B}}}(\mathbf{Q}) \cdot \widetilde{\nabla} \mathbf{Q} = \mathbf{S}(\mathbf{Q}) \tag{50}$$

with

$$\widetilde{\nabla} = \left(\frac{\partial}{\partial t}, \nabla\right), \qquad \widetilde{\boldsymbol{\mathcal{F}}} = (\mathbf{Q}, \boldsymbol{\mathcal{F}}(\mathbf{Q})), \qquad \widetilde{\boldsymbol{\mathcal{B}}}(\mathbf{Q}) = \left(0, \boldsymbol{\mathcal{B}}_1(\mathbf{Q}), \boldsymbol{\mathcal{B}}_2(\mathbf{Q}), \boldsymbol{\mathcal{B}}_3(\mathbf{Q})\right).$$

Integration of (50) on a space-time control volume $\widetilde{C}_i$, leads to

$$\int_{\widetilde{C}_i} \widetilde{\nabla} \cdot \widetilde{\boldsymbol{\mathcal{F}}}(\mathbf{Q})\, \mathrm{dt}\, \mathrm{dV} + \int_{\widetilde{C}_i} \widetilde{\boldsymbol{\mathcal{B}}}(\mathbf{Q}) \cdot \widetilde{\nabla} \mathbf{Q}\, \mathrm{dt}\, \mathrm{dV} = \int_{\widetilde{C}_i} \boldsymbol{\mathcal{S}}(\mathbf{Q})\, \mathrm{dt}\, \mathrm{dV}\,. \tag{51}$$

Now, Gauss theorem is applied to transform the space-time integral of the flux into the integral over the space-time boundary $\widetilde{\Gamma}_{\mathrm{i}}$. Moreover, we employ a path conservative approach to deal with the non-conservative products splitting their contribution into a smooth part within the control volume and the jumps at its boundaries [87]. Hence, we have

$$\int_{\widetilde{\Gamma}_{\mathrm{i}}} \widetilde{\boldsymbol{\mathcal{F}}}(\mathbf{Q}) \cdot \widetilde{\boldsymbol{n}}_{\mathrm{i}} \,\mathrm{dt}\,\mathrm{dS} + \int_{\widetilde{\Gamma}_{\mathrm{i}}} \widetilde{\boldsymbol{\mathcal{D}}}(\mathbf{Q}) \cdot \widetilde{\boldsymbol{n}}_{\mathrm{i}} \,\mathrm{dt}\,\mathrm{dS} + \int_{\widetilde{C}_{\mathrm{i}}^{\circ}} \widetilde{\boldsymbol{\mathcal{B}}}(\mathbf{Q}) \cdot \widetilde{\nabla}\mathbf{Q} \,\mathrm{dt}\,\mathrm{dV} = \int_{\widetilde{C}_{\mathrm{i}}} \boldsymbol{\mathcal{S}}(\mathbf{Q}) \,\mathrm{dt}\,\mathrm{dV}\,. \tag{52}$$

From (42), we can split the integrals over the faces into the integral over the space-time boundary surfaces $\widetilde{\Gamma}_{\mathrm{ij}}$ and the two boundaries of $\widetilde{C}_{\mathrm{i}}$ orthogonal to the time axis, i.e. C_{i}^{n} and C_{i}^{n+1}, so

$$\left|\widetilde{C}_{\mathrm{i}}\right|\mathbf{Q}_{\mathrm{i}}^{*} = \left|\widetilde{C}_{\mathrm{i}}\right|\mathbf{Q}_{\mathrm{i}}^{n} - \sum_{\mathrm{j}\in\mathcal{K}_{\mathrm{i}}} \int_{\widetilde{\Gamma}_{\mathrm{ij}}} \left(\widetilde{\boldsymbol{\mathcal{F}}}(\mathbf{Q}) + \widetilde{\boldsymbol{\mathcal{D}}}(\mathbf{Q})\right) \cdot \widetilde{\boldsymbol{n}}_{\mathrm{ij}} \,\mathrm{dt}\,\mathrm{dS} - \int_{\widetilde{C}_{\mathrm{i}}^{\circ}} \widetilde{\boldsymbol{\mathcal{B}}}(\mathbf{Q}) \cdot \widetilde{\nabla}\mathbf{Q} \,\mathrm{dt}\,\mathrm{dV} + \int_{\widetilde{C}_{\mathrm{i}}^{\circ}} \boldsymbol{\mathcal{S}}(\mathbf{Q}) \,\mathrm{dt}\,\mathrm{dV}, \tag{53}$$

where, for the GLM GPR model, we define $\mathbf{Q}^{*} = \left(\rho^{n+1}, \rho\mathbf{u}^{*}, \mathbf{A}^{n+1}, \boldsymbol{\varphi}_{\mathbf{A}}^{n+1}, \mathbf{J}^{n+1}, \boldsymbol{\psi}_{\mathbf{J}}^{n+1}, \mathcal{E}^{*}\right)^{T}$.

3.4.1. Convective terms

Denoting $\widetilde{\boldsymbol{\mathcal{F}}}\left(\mathbf{Q}_{\mathrm{i}}^{n}, \mathbf{Q}_{\mathrm{j}}^{n}, \widetilde{\boldsymbol{\eta}}_{\mathrm{ij}}\right)$ a numerical flux function, we approximate the flux terms in (53) as

$$\sum_{\mathrm{j}\in\mathcal{K}_{\mathrm{i}}} \int_{\widetilde{\Gamma}_{\mathrm{ij}}} \widetilde{\boldsymbol{\mathcal{F}}}(\mathbf{Q}) \cdot \widetilde{\boldsymbol{n}}_{\mathrm{ij}} \,\mathrm{dt}\,\mathrm{dS} = \sum_{\mathrm{j}\in\mathcal{K}_{\mathrm{i}}} \widetilde{\boldsymbol{\mathcal{F}}}\left(\mathbf{Q}_{\mathrm{i}}^{n}, \mathbf{Q}_{\mathrm{j}}^{n}, \widetilde{\boldsymbol{\eta}}_{\mathrm{ij}}\right). \tag{54}$$

For instance, for the Rusanov numerical flux function [88], we have

$$\widetilde{\boldsymbol{\mathcal{F}}}^{R}\left(\overline{\mathbf{Q}}_{\mathrm{i},R}^{n}, \overline{\mathbf{Q}}_{\mathrm{j},L}^{n}, \widetilde{\boldsymbol{\eta}}_{\mathrm{ij}}\right) = \frac{1}{2}\left(\widetilde{\boldsymbol{\mathcal{F}}}\left(\overline{\mathbf{Q}}_{\mathrm{i},R}^{n}\right) + \widetilde{\boldsymbol{\mathcal{F}}}\left(\overline{\mathbf{Q}}_{\mathrm{j},L}^{n}\right)\right) \cdot \widetilde{\boldsymbol{\eta}}_{\mathrm{ij}} - \frac{1}{2}\alpha_{\mathrm{ij}}^{n}\left(\overline{\mathbf{Q}}_{\mathrm{j},L}^{n} - \overline{\mathbf{Q}}_{\mathrm{i},R}^{n}\right) \tag{55}$$

with the maximum signal speed on the edge

$$\alpha_{\mathrm{ij}}^{n} = \max\left\{\left|\overline{\mathbf{u}}_{\mathrm{i},R}^{n} \cdot \boldsymbol{\eta}_{\mathrm{ij}} - \upsilon_{\mathrm{ij}}^{n} \pm c_{\mathrm{i},R}^{n}\right|, \left|\overline{\mathbf{u}}_{\mathrm{j},L}^{n} \cdot \boldsymbol{\eta}_{\mathrm{ij}} - \upsilon_{\mathrm{ij}}^{n} \pm c_{\mathrm{j},L}^{n}\right|, \left|\overline{\mathbf{u}}_{\mathrm{i},R}^{n} \cdot \boldsymbol{\eta}_{\mathrm{ij}} - \upsilon_{\mathrm{ij}}^{n} \pm c_{\mathbf{A},\mathrm{i}}\right|, \left|\overline{\mathbf{u}}_{\mathrm{j},L}^{n} \cdot \boldsymbol{\eta}_{\mathrm{ij}} - \upsilon_{\mathrm{ij}}^{n} \pm c_{\mathbf{A},\mathrm{j}}\right|,\right.$$
$$\left.\left|\overline{\mathbf{u}}_{\mathrm{i},R}^{n} \cdot \boldsymbol{\eta}_{\mathrm{ij}} - \upsilon_{\mathrm{ij}}^{n} \pm c_{\mathbf{J},\mathrm{i}}\right|, \left|\overline{\mathbf{u}}_{\mathrm{j},L}^{n} \cdot \boldsymbol{\eta}_{\mathrm{ij}} - \upsilon_{\mathrm{ij}}^{n} \pm c_{\mathbf{J},\mathrm{j}}\right|\right\}, \qquad c_{\mathrm{i},R}^{n} = \sqrt{\frac{4}{3}c_{s}^{2} + \frac{2c_{h}^{2}\overline{T}_{\mathrm{i},R}^{n}}{\left(\overline{\rho}_{\mathrm{i},R}^{n}\right)^{2} c_{v}}}, \tag{56}$$

approximated from the eigenvalues obtained for the unidimensional GPR model. Following the seminal ideas in [89] to guarantee Galilean invariance of the ALE method, the flux should be computed in the rest-frame of each mesh face, i.e. in a frame moving with the normal face velocity, $\upsilon_{\mathrm{ij}}^{n}$, rather than in the lab-frame, which corresponds to the global fixed coordinates. In the particular case of the Rusanov flux and since we are using space-time control volumes, it is sufficient to evaluate the eigenvalues using the relative velocity, as indicated in (56). To get a second order scheme, the half in time evolved and boundary extrapolated states, $\overline{\mathbf{Q}}_{\mathrm{i},R}^{n}$, $\overline{\mathbf{Q}}_{\mathrm{j},L}^{n}$, are computed following a local ADER approach [78,90,91]:

1. Calculate the gradients in space, $\nabla\mathbf{Q}^{n}$, and time, $\nabla_{t}\mathbf{Q}_{\mathrm{i}}^{n}$. To address the spacial gradient, the Crouzeix-Raviart basis functions on the primal elements are used, assuming the averaged values of $\mathbf{Q}^{n}$ approximate the values at the barycentres of the primal element faces. Second order is achieved by choosing the gradient to be the one of the primal element containing the dual face. For the time derivative, a Cauchy-Kovalevskaya, or Lax-Wendroff, procedure [92] is applied.
2. Employ the reference element in order to calculate the coordinates of the barycentre of the space-time face and compute the displacement with respect to the barycentres of cells C_{i}^{n} and C_{j}^{n}:

$$\Delta\mathbf{x}_{\mathrm{i}} = \widetilde{\mathbf{x}}_{\mathrm{ij}}(0.5, 0.5) - \mathbf{x}_{\mathrm{i}}, \qquad \Delta\mathbf{x}_{\mathrm{j}} = \widetilde{\mathbf{x}}_{\mathrm{ij}}(0.5, 0.5) - \mathbf{x}_{\mathrm{j}}.$$

3. Perform the half in time evolution and extrapolate the data at the boundary:

$$\overline{\mathbf{Q}}_{\mathrm{i},R} = \mathbf{Q}_{\mathrm{i}}^{n} + \frac{\Delta t}{2}\nabla_{t}\mathbf{Q}_{\mathrm{i}}^{n} + \nabla\mathbf{Q}^{n} \cdot \Delta\mathbf{x}_{\mathrm{i}}, \qquad \overline{\mathbf{Q}}_{\mathrm{j},L} = \mathbf{Q}_{\mathrm{j}}^{n} + \frac{\Delta t}{2}\nabla_{t}\mathbf{Q}_{\mathrm{j}}^{n} + \nabla\mathbf{Q}^{n} \cdot \Delta\mathbf{x}_{\mathrm{j}}.$$

In the numerical results section, to circumvent Godunov's theorem and guarantee a stable scheme, the former ADER approach is modified including the ENO strategy [93] or the min-mod limiter of Roe [94]. Further, we observe that, in most simulations, employing ENO limiting based on the physical variables instead of the conservative ones would lead to smoother solutions. Besides, adding a small artificial viscosity depending on a coefficient c_{α} can improve stability of the overall algorithm when small velocities are observed in comparison with the magnitude of the pressure field [33].

3.4.2. Non-conservative terms: A path-conservative approach

As aforementioned, the non-conservative products are approximated employing a path conservative scheme. Accordingly, we approximate

$$\int_{\widetilde{\Gamma}_{\mathrm{i}}} \widetilde{\boldsymbol{\mathcal{D}}}(\mathbf{Q}^{n}) \cdot \widetilde{\boldsymbol{n}}_{\mathrm{i}} \,\mathrm{dt}\,\mathrm{dS} = \sum_{\mathrm{j}\in\mathcal{K}_{\mathrm{i}}} \widetilde{\boldsymbol{\mathcal{D}}}\left(\mathbf{Q}_{\mathrm{i}}^{n}, \mathbf{Q}_{\mathrm{j}}^{n}, \widetilde{\boldsymbol{\eta}}_{\mathrm{ij}}\right). \tag{57}$$

Considering the straight line segment path

$$\psi = \psi\left(\mathbf{Q}_{\mathrm{i}}^{n}, \mathbf{Q}_{\mathrm{j}}^{n}, s\right) = \mathbf{Q}_{\mathrm{i}}^{n} + s\left(\mathbf{Q}_{\mathrm{j}}^{n} - \mathbf{Q}_{\mathrm{i}}^{n}\right), \qquad s \in [0,1], \tag{58}$$

and the reconstructed variables to attain second order, we have

$$\widetilde{\boldsymbol{\mathcal{D}}}(\overline{\mathbf{Q}}_{\mathrm{i},R}^{n}, \overline{\mathbf{Q}}_{\mathrm{j},L}^{n}, \widetilde{\boldsymbol{\eta}}_{\mathrm{ij}}) = \frac{1}{2}\widetilde{\boldsymbol{\mathcal{B}}}_{\mathrm{ij}}\left(\overline{\mathbf{Q}}_{\mathrm{j},L}^{n} - \overline{\mathbf{Q}}_{\mathrm{i},R}^{n}\right), \qquad \widetilde{\boldsymbol{\mathcal{B}}}_{\mathrm{ij}} = \int_{0}^{1} \widetilde{\boldsymbol{\mathcal{B}}}\left(\psi\left(\overline{\mathbf{Q}}_{\mathrm{i},R}^{n}, \overline{\mathbf{Q}}_{\mathrm{j},L}^{n}, s\right)\right) \cdot \widetilde{\boldsymbol{\eta}}_{\mathrm{ij}}\, \mathrm{dS}\,. \tag{59}$$

On the other hand, we compute the half in time evolved conservative variables at each space-time control volume $\widetilde{C}_{\mathrm{i}}$ as

$$\overline{\mathbf{Q}}_{\mathrm{i}}^{n} = \mathbf{Q}_{\mathrm{i}}^{n} + \frac{\Delta t}{4}\left(\nabla_{t}\mathbf{Q}_{\mathrm{i}_1}^{n} + \nabla_{t}\mathbf{Q}_{\mathrm{i}_2}^{n}\right), \tag{60}$$

where the subindex i_1, i_2 refer to the two primal elements from which the dual cell is built, $\widetilde{T}_{\mathrm{i}_1}$, $\widetilde{T}_{\mathrm{i}_2}$. Then, using a weighted average for the computation of the gradient at the control volume, we have

$$\int_{\widetilde{C}_{\mathrm{i}}^{\circ}} \widetilde{\boldsymbol{\mathcal{B}}}(\overline{\mathbf{Q}}) \cdot \widetilde{\nabla}\overline{\mathbf{Q}}\, \mathrm{dt}\, \mathrm{dV} = \left|\widetilde{C}_{\mathrm{i}}\right| \boldsymbol{\mathcal{B}}(\overline{\mathbf{Q}}_{\mathrm{i}}^{n}) \left(\frac{\left|C_{\mathrm{i}_1}^{n}\right|}{\left|C_{\mathrm{i}}^{n}\right|} \nabla \overline{\mathbf{Q}}_{\mathrm{i}_1}^{n} + \frac{\left|C_{\mathrm{i}_2}^{n}\right|}{\left|C_{\mathrm{i}}^{n}\right|} \nabla \overline{\mathbf{Q}}_{\mathrm{i}_2}^{n} \right), \qquad \left|\widetilde{C}_{\mathrm{i}}\right| = \frac{1}{2}\left(\left|C_{\mathrm{i}}^{n}\right| + \left|C_{\mathrm{i}}^{n+1}\right|\right)\Delta t\,. \tag{61}$$

Above, $\left|C_{\mathrm{i}_1}^{n}\right|$, $\left|C_{\mathrm{i}_2}^{n}\right|$ denote the areas of the two halves of the dual element C_{i}^{n} corresponding to $T_{\mathrm{i}_1}^{n}$ and $T_{\mathrm{i}_2}^{n}$, respectively.

In order for the ALE scheme to satisfy Galilean invariance, the computation of the non-conservative products is done in the rest-frame, thus accounting for the relative velocity. In particular, the distortion and thermal impulse fields involve a velocity-dependent non-conservative product matrix $\boldsymbol{\mathcal{B}}(\mathbf{Q}, \mathbf{v})$, where $\mathbf{v}$ denotes the mesh velocity. The jump term (59) is computed on each face Γ_{ij} by approximating the normal relative velocity in $\widetilde{\boldsymbol{\mathcal{B}}}_{\mathrm{ij}}$ as $\overline{\mathbf{u}}_{\mathrm{ij}}^{n} \cdot \boldsymbol{\eta}_{\mathrm{ij}} - v_{ij}^{n}$, with $\overline{\mathbf{u}}_{\mathrm{ij}}^{n} = \frac{1}{2}\left(\overline{\mathbf{Q}}_{\mathrm{i},R}^{n} + \overline{\mathbf{Q}}_{\mathrm{j},L}^{n}\right)$ and v_{ij}^{n} the normal face velocity, already introduced for the computation of the eigenvalues. Meanwhile, for the smooth part of the non-conservative product (61), we first calculate the mesh velocity associated to the node of the dual element, $\mathbf{v}_{\mathrm{i}}^{n}$. Then, the relative velocity, $\overline{\mathbf{u}}_{\mathrm{i}}^{n} - \mathbf{v}_{\mathrm{i}}^{n}$, is used to approximate $\boldsymbol{\mathcal{B}}(\overline{\mathbf{Q}}_{\mathrm{i}}^{n})$.

3.4.3. Source terms

The source terms of the momentum, (37b), and total energy, (37g), equations are simply integrated on the control volume employing the half in time evolved density and momentum as

$$\int_{\widetilde{C}_{\mathrm{i}}^{\circ}} \rho_{\mathrm{i}}\mathbf{g}\, \mathrm{dt}\, \mathrm{dV} = \left|\widetilde{C}_{\mathrm{i}}\right| \overline{\rho}_{\mathrm{i}}^{n}\mathbf{g}, \qquad \int_{\widetilde{C}_{\mathrm{i}}^{\circ}} \rho_{\mathrm{i}}\mathbf{g} \cdot \mathbf{u}\, \mathrm{dt}\, \mathrm{dV} = \left|\widetilde{C}_{\mathrm{i}}\right| \mathbf{g} \cdot \overline{\rho\mathbf{u}}_{\mathrm{i}}^{n}. \tag{62}$$

As mentioned previously, in the visco-plastic limit of the model, the source terms related to the distortion tensor and thermal impulse can become very stiff. Therefore, (11) and (13) are split into two subsystems. The first subsystem accounts for the contributions of the flux term and the non-conservative products and is discretized as described in the previous sections. This yields intermediate values of the distortion and thermal impulse fields, and $\mathbf{J}_{\mathrm{i}}^{*}$. The second subsystem, corresponding to (41), is given by

$$\partial_t A_{ik} = -\frac{1}{\theta_1(\tau_1)} E_{A_{ik}}, \tag{63a}$$

$$\partial_t J_k = -\frac{1}{\theta_2(\tau_2)} E_{J_k}. \tag{63b}$$

Following [38], this system of ordinary differential equations is locally solved at each dual cell using the Runge-Kutta DIRK scheme [95] combined with an inexact Newton algorithm. As a consequence, we get the updated fields $\mathbf{A}_{\mathrm{i}}^{n+1}$, $\mathbf{J}_{\mathrm{i}}^{n+1}$.

The numerical scheme resulting from the former formulation of the distortion field, (1c), is not asymptotic preserving in the fluid relaxation limit of the model [36]. To recover the Navier-Stokes equations in the limit $\tau \to 0$, we reorder the flux and the non-conservative product contributions of the distortion field equations into two terms as

$$\frac{\partial}{\partial t} A_{ik} + A_{im}\frac{\partial}{\partial x_k} u_m + u_m \frac{\partial}{\partial x_m} A_{ik} = -\frac{1}{\theta_1(\tau_1)} E_{A_{ik}}. \tag{64}$$

The linear term $A_{im}\frac{\partial}{\partial x_k}u_m$ is then discretised like the smooth part of the non-conservative products, i.e., using the gradients obtained at the dual cells applying the Galerkin approach. On the other hand, the term $u_m \frac{\partial}{\partial x_m} A_{ik}$ is computed implicitly within the source term system. Accordingly, we have

$$A_{ik}^{n+1} + \frac{\Delta t}{\theta_1^{n+1}(\tau_1)} E_{A_{ik}}^{n+1} = A_{ik}^{\star}, \tag{65a}$$

$$A_{ik}^{\star} = A_{ik}^{n} - \Delta t\, A_{im}^{n}\frac{\partial}{\partial x_k}\tilde{u}_m - \Delta t\, u_m^{n}\frac{\partial}{\partial x_m} A_{ik}^{n}, \tag{65b}$$

with the gradient $\frac{\partial}{\partial x_k}\tilde{u}_m$ approximated using the Galerkin approach. This formulation provides a natural framework to impose wall boundary conditions in the fluid limit of the model. In particular, the given boundary velocity field at the Crouzeix-Raviart node

located at the boundary is employed, together with the previous time step velocity values at the internal nodes, to approximate the velocity gradient. This asymptotic preserving approach is used in Section 4, when wall boundary conditions are defined. Further details on the treatment of boundary conditions for the GPR model can be found in [38].

3.5. Pressure stage: Solution of the pressure subsystem

To solve the pressure system, we first derive its weak formulation. Multiplication of (37h) by a test function $z \in H_0^1 = \left\{ z \in H^1(\Omega) \mid \int_\Omega z \,\mathrm{dV} = 0 \right\}$, and integration over the computational domain gives

$$\frac{1}{\gamma - 1} \int_\Omega \delta p^{n+1,\ell+1} z \,\mathrm{dV} - \Delta t^2 \int_\Omega \frac{\partial}{\partial x_j} \left(h^{n+1,\ell} \frac{\partial}{\partial x_j} \delta p^{n+1,\ell+1} \right) z \,\mathrm{dV} = -\Delta t \int_\Omega \frac{\partial}{\partial x_j} \left(h^{n+1,\ell} \rho u_j^* \right) z \,\mathrm{dV}$$
$$+ \int_\Omega \left(\mathcal{E}^* - \mathcal{E}_1^n - \mathcal{E}_2^{n+1,\ell} - \mathcal{E}_3^{n+1} - \mathcal{E}_4^{n+1} - \mathcal{E}_5^{n+1} - \mathcal{E}_6^{n+1} \right) z \,\mathrm{dV}. \tag{66}$$

Then, applying Green's theorem and taking into account the relation (37i), we obtain the weak problem

$$\frac{1}{\gamma - 1} \int_\Omega \delta p^{n+1,\ell+1} z \,\mathrm{dV} + \Delta t^2 \int_\Omega h^{n+1,\ell} \frac{\partial}{\partial x_j} \delta p^{n+1,\ell+1} \frac{\partial}{\partial x_j} z \,\mathrm{dV} = \Delta t \int_\Omega h^{n+1,\ell} \rho u_j^* \frac{\partial}{\partial x_j} z \,\mathrm{dV}$$
$$+ \int_\Omega \left(\mathcal{E}^* - \mathcal{E}_1^n - \mathcal{E}_2^{n+1,\ell} - \mathcal{E}_3^{n+1} - \mathcal{E}_4^{n+1} - \mathcal{E}_5^{n+1} - \mathcal{E}_6^{n+1} \right) z \,\mathrm{dV} - \Delta t \int_\Gamma h^{n+1,\ell} \rho u_j^{n+1} n_j z \,\mathrm{dS}. \tag{67}$$

This problem can be discretized using $\mathbb{P}^1$ Lagrange finite element methods in the updated primal grid. Let us remark that the use of Picard iterations increase one order in time per iteration. Hence, two Picard iterations are enough to preserve the accuracy of the overall scheme. Further, the resulting pressure system is symmetric and positive definite so a classical conjugate gradient method can be employed for its solution.

We observe that the right hand side of (67) involves intermediate and updated values of several variables that have been computed in the dual grid. Therefore, previous to the pressure stage, we perform an intermediate stage to interpolate the needed data between the staggered grids, as detailed in Section 3.7. Moreover, $\mathcal{E}_2^{n+1,\ell}$ is updated at each Picard iteration approximating the momentum according to (37i) as

$$\rho \mathbf{u}_{\mathfrak{i}}^{n+1,\ell} = \rho \mathbf{u}_{\mathfrak{i}}^* - \Delta t \frac{1}{|T_k|} \sum_{k \in \hat{\mathcal{K}}_{\mathfrak{i}}} |T_{k\mathfrak{i}}| \left(\nabla \delta p^{n+1,\ell} \right)_k \tag{68}$$

with $(\nabla p)_k$ the pressure gradient computed using the $\mathbb{P}^1$ basis functions in the primal element T_k, and computing

$$\mathcal{E}_2^{n+1,\ell} = \frac{1}{2\rho^{n+1}} \left| \rho \mathbf{u}^{n+1,\ell} \right|^2. \tag{69}$$

Finally, the enthalpy $h^{n+1,\ell}$ is calculated at each primal vertex by substituting $p^{n+1,\ell} = p^n + \delta p^{n+1,\ell}$ in (34). The enthalpy at each primal face, which is also assumed to be the updated average value in the corresponding dual cell, is then computed as the average of its values on the vertex of the face.

3.6. Correction stage: Update of the intermediate velocity and total energy

Once the pressure correction δp^{n+1} is computed, we update the velocity and total energy according to (68) and (37j). In particular, the energy correction is first performed by primal element

$$\mathcal{E}_k^{n+1} = \mathcal{E}_k - \frac{\Delta t}{|T_k|} \sum_{l \in \mathcal{K}_k} \int_{\Gamma_{kl}} h^{n+1} \rho \mathbf{u}^{n+1} \cdot \boldsymbol{n}_{kl} \, dS. \tag{70}$$

Next, the obtained values are interpolated to the dual cells as

$$\mathcal{E}_{\mathfrak{i}}^{n+1} = \frac{1}{|C_{\mathfrak{i}}|} \sum_{k \in \hat{\mathcal{K}}_i} |T_{k\mathfrak{i}}| \mathcal{E}_k^{n+1}. \tag{71}$$

3.7. Intermediate stage: Interpolation between grids

It is important to recall that once the transport stage has been performed, all variables live in the new mesh configuration. Therefore, mesh interpolation between the dual and primal grids for ALE is carried out in the same way as for the purely Eulerian approach [38]. More precisely, given a scalar field at the dual cells, $q_{\mathfrak{i}}$, we approximate the solution at each primal element, q_k, as a weighted average of the form

$$q_k = \sum_{\mathfrak{i} \in \hat{\mathcal{K}}_k} q_{\mathfrak{i}} \frac{|T_{k\mathfrak{i}}|}{|T_k|}. \tag{72}$$

Table 1
2D Taylor-Green vortex. Main features of the primal triangular grids used to run the convergence table.

Mesh	Primal elements	Vertices	Dual elements
M_1	128	81	208
M_2	512	289	800
M_3	2048	1089	3136
M_4	8192	4225	12416
M_5	32768	16641	49408
M_6	131072	66049	197120
M_7	524288	263169	787456

This interpolation needs to be done for the density, ρ^{n+1}, and the intermediate momentum, $\rho\mathbf{u}^*$, to compute the initial kinetic energy $\mathcal{E}_2^{n+1,1}$. Further, we also apply (72) to get the intermediate total energy density, $\mathcal{E}^*$, the total energy components $\mathcal{E}_3^{n+1}$, $\mathcal{E}_4^{n+1}$, $\mathcal{E}_5^{n+1}$ and $\mathcal{E}_6^{n+1}$, and the initial enthalpy which is first approximated at each dual cell as

$$h_{\mathrm{i}}^{n+1,1} = \frac{\gamma p_{\mathrm{i}}^n + \rho_0 c_0^2 - \gamma p_0}{\rho_{\mathrm{i}}^{n+1}(\gamma - 1)}. \tag{73}$$

Then, the related volume integrals in the right hand side of (67) are calculated assuming a constant value of the involved variables by primal element. Meanwhile, for the term depending on $\mathcal{E}_1^n$, we employ the values of the pressure at each primal vertex computed in the previous iteration. Hence, its contribution is calculated using the standard mass matrix of the $\mathbb{P}^1$ FEM employed in the pressure discretisation. The boundary integral in the right hand side of (67) is performed setting the enthalpy at each primal boundary to be the averaged value at the dual cell containing it.

4. Numerical results

In this section, we analyse several test cases both in the fluid and solid limits of the GPR model to assess the main properties of the proposed ALE hybrid methodology. In what follows, the international system of units is employed and all test cases are initialized considering $\mathbf{A} = \mathbf{I}$ and $\mathbf{J} = \mathbf{0}$. Further, unless stated the contrary, the time step is dynamically computed at each time iteration attending to a CFL stability condition based on the transport-diffusion subsystem, i.e.

$$\Delta t = \min_{C_{\mathrm{i}}} \left\{ \Delta t_{\mathrm{i}} \right\}, \qquad \Delta t_{\mathrm{i}} = \frac{\mathrm{CFL}\, r_{\mathrm{i}}}{|\lambda_{\mathrm{i}}|_{\max}},$$

where $|\lambda_{\mathrm{i}}|_{\max}$ is de maximum of the absolute approximated eigenvalues of the subsystem at cell C_{i} and r_{i} is the incircle diameter of the cell. The eigenvalues are approximated from those calculated in the 1D case as

$$\lambda \in \{|\mathbf{u}| - c, |\mathbf{u}|, |\mathbf{u}| + c\}, \quad c = \sqrt{\frac{4}{3}c_s^2 + 2\frac{c_h^2 T}{\rho^2 c_v}}, \tag{74}$$

for the original GPR model, (1), and

$$\lambda \in \left\{|\mathbf{u}| - c_{\mathbf{J}}, |\mathbf{u}| - c_{\mathbf{A}}, |\mathbf{u}| - c, |\mathbf{u}|, |\mathbf{u}| + c, |\mathbf{u}| + c_{\mathbf{A}}, |\mathbf{u}| + c_{\mathbf{J}}\right\}, \tag{75}$$

if we consider the augmented GLM curl cleaning GPR model, (1a)–(1b), (11)–(14), (1e). Generally, for the second order scheme, we take CFL = 0.5.

4.1. Convergence test, low Mach number asymptotic behaviour and Galilean invariance

As first test case, we consider the 2D Taylor Green vortex, a classical benchmark for assessing the order of convergence of numerical methods in fluid dynamics. The initial condition reads

$$\mathbf{u}(\mathbf{x}, 0) = \begin{pmatrix} \sin(x)\cos(y) \\ -\cos(x)\sin(y) \end{pmatrix}, \quad p(\mathbf{x}, 0) = \frac{p_0}{\gamma} + \frac{1}{4}(\cos(2x) + \cos(2y)).$$

Meanwhile, the model parameters, leading to an low Mach inviscid flow with $M \approx 3.2 \times 10^{-3}$, are $c_s = c_h = 0$, $\mu = \kappa = 0$, $c_v = 2.5$, $c_p = 3.5$, $p_0 = 10^5$. As computational domain, we set $\Omega = [0, 2\pi]^2$ with periodic boundary conditions everywhere. The errors and orders of convergence for a set of successively refined Cartesian triangular grids described in Table 1 are reported in Table 2. The Cartesian triangular grids employed for the simulations are constructed as follows. First a regular Cartesian grid made of quadrilaterals is generated. Then, each element is divided into two triangular elements by joining with a new element boundary two opposite vertex of the quadrilateral.

This test case is also run for a set of decreasing Mach numbers to analyse the asymptotic behaviour of the proposed methodology in the low Mach number limit. Table 3 confirms that the order of convergence is preserved for very low Mach number regimes. Let us note that the limit scheme for the incompressible Navier-Stokes equations in which the proposed hybrid method is based [78], is

Table 2
Taylor-Green vortex. Spatial L_2 error norms and convergence rates at time $t = 0.1$.

Mesh	$L^2_\Omega(\rho)$	$\mathcal{O}(\rho)$	$L^2_\Omega(\rho\mathbf{u})$	$\mathcal{O}(\rho\mathbf{u})$	$L^2_\Omega(p)$	$\mathcal{O}(p)$
M1	$2.43 \cdot 10^{-2}$		$1.05 \cdot 10^{-1}$		$5.03 \cdot 10^{-1}$	
M2	$3.51 \cdot 10^{-3}$	2.79	$2.95 \cdot 10^{-2}$	1.83	$1.26 \cdot 10^{-1}$	2.00
M3	$5.15 \cdot 10^{-4}$	2.77	$7.62 \cdot 10^{-3}$	1.95	$3.04 \cdot 10^{-2}$	2.05
M4	$9.16 \cdot 10^{-5}$	2.49	$1.90 \cdot 10^{-3}$	2.00	$7.56 \cdot 10^{-3}$	2.01
M5	$1.96 \cdot 10^{-5}$	2.23	$4.75 \cdot 10^{-4}$	2.00	$1.89 \cdot 10^{-3}$	2.00
M6	$4.50 \cdot 10^{-6}$	2.12	$1.19 \cdot 10^{-4}$	2.00	$1.02 \cdot 10^{-3}$	0.90
M7	$1.68 \cdot 10^{-6}$	1.42	$2.97 \cdot 10^{-5}$	2.00	$1.21 \cdot 10^{-4}$	3.07

Table 3
2D Taylor-Green vortex. Spatial L_2 error norms and convergence rates of the density, momentum, total energy and pressure at time $t = 0.1$ for $M \in \{10^{-2}, 10^{-3}, 10^{-4}, 10^{-5}\}$. Results computed using the second order approach.

Mesh	$L^2_\Omega(\rho)$	$\mathcal{O}(\rho)$	$L^2_\Omega(\rho\mathbf{u})$	$\mathcal{O}(\rho\mathbf{u})$	$L^2_\Omega(\mathcal{E})$	$\mathcal{O}(\mathcal{E})$	$L^2_\Omega(p)$	$\mathcal{O}(p)$
$M = 10^{-2}$, $p_0 = 10^4$ (double precision)								
M1	$2.43 \cdot 10^{-2}$		$1.05 \cdot 10^{-1}$		$8.57 \cdot 10^{1}$		$5.07 \cdot 10^{-1}$	
M2	$3.50 \cdot 10^{-3}$	2.79	$2.95 \cdot 10^{-2}$	1.83	$5.59 \cdot 10^{0}$	3.94	$1.26 \cdot 10^{-1}$	2.01
M3	$5.09 \cdot 10^{-4}$	2.78	$7.62 \cdot 10^{-3}$	1.95	$3.99 \cdot 10^{-1}$	3.81	$3.04 \cdot 10^{-2}$	2.05
M4	$8.97 \cdot 10^{-5}$	2.50	$1.91 \cdot 10^{-3}$	2.00	$3.04 \cdot 10^{-2}$	3.71	$7.55 \cdot 10^{-3}$	2.01
$M = 10^{-3}$, $p_0 = 10^6$ (double precision)								
M1	$2.43 \cdot 10^{-2}$		$1.05 \cdot 10^{-1}$		$8.53 \cdot 10^{3}$		$5.03 \cdot 10^{-1}$	
M2	$3.51 \cdot 10^{-3}$	2.79	$2.95 \cdot 10^{-2}$	1.83	$5.51 \cdot 10^{2}$	3.95	$1.26 \cdot 10^{-1}$	2.00
M3	$5.15 \cdot 10^{-4}$	2.77	$7.62 \cdot 10^{-3}$	1.95	$3.83 \cdot 10^{1}$	3.85	$3.04 \cdot 10^{-2}$	2.05
M4	$9.16 \cdot 10^{-5}$	2.49	$1.90 \cdot 10^{-3}$	2.00	$2.62 \cdot 10^{0}$	3.87	$7.56 \cdot 10^{-3}$	2.01
$M = 10^{-4}$, $p_0 = 10^8$ (quadruple precision)								
M1	$2.43 \cdot 10^{-2}$		$1.05 \cdot 10^{-1}$		$8.53 \cdot 10^{5}$		$5.03 \cdot 10^{-1}$	
M2	$3.51 \cdot 10^{-3}$	2.79	$2.95 \cdot 10^{-2}$	1.83	$5.51 \cdot 10^{4}$	3.95	$1.26 \cdot 10^{-1}$	2.00
M3	$5.15 \cdot 10^{-4}$	2.77	$7.62 \cdot 10^{-3}$	1.95	$3.83 \cdot 10^{3}$	3.85	$3.04 \cdot 10^{-2}$	2.05
M4	$9.16 \cdot 10^{-5}$	2.49	$1.90 \cdot 10^{-3}$	2.00	$2.62 \cdot 10^{2}$	3.87	$7.56 \cdot 10^{-3}$	2.01
$M = 10^{-5}$, $p_0 = 10^{10}$ (quadruple precision)								
M1	$2.43 \cdot 10^{-2}$		$1.05 \cdot 10^{-1}$		$8.53 \cdot 10^{7}$		$5.03 \cdot 10^{-1}$	
M2	$3.51 \cdot 10^{-3}$	2.79	$2.95 \cdot 10^{-2}$	1.83	$5.51 \cdot 10^{6}$	3.95	$1.26 \cdot 10^{-1}$	2.00
M3	$5.15 \cdot 10^{-4}$	2.77	$7.62 \cdot 10^{-3}$	1.95	$3.83 \cdot 10^{5}$	3.85	$3.04 \cdot 10^{-2}$	2.05
M4	$9.58 \cdot 10^{-5}$	2.43	$1.91 \cdot 10^{-3}$	2.00	$5.72 \cdot 10^{4}$	2.74	$7.56 \cdot 10^{-3}$	2.01

not exactly divergence free. Hence, when $M \to 0$ the errors are not expected to decrease quadratically but to be preserved. Due to the magnitude of the pressure variable, for very low Mach numbers quadruple precision is required.

To analyse also the behaviour of the ALE hybrid approach, we consider the isentropic vortex and let the mesh freely move according to the fluid velocity [43]. The solution is given by a rotating vortex defined as

$$\rho(\mathbf{x},0) = 1, \quad \mathbf{u}(\mathbf{x},0) = \begin{pmatrix} -re^{-\frac{1}{2}(r^2-1)}\sin\varphi \\ re^{-\frac{1}{2}(r^2-1)}\cos\varphi \end{pmatrix} + \mathbf{u}^{\mathrm{g}}, \quad p(\mathbf{x},0) = \frac{p_0}{\gamma} - \frac{1}{2}e^{-r^2+1}, \quad \varphi = \arctan(y-5, x-5), \tag{76}$$

with $r = \sqrt{(x-5)^2 + (y-5)^2}$ the radius to the centre of the computational domain $\Omega = [0,10]^2$. Since this benchmark studies an inviscid incompressible fluid, the parameters for the GPR model are taken as $c_h = c_s = \mu = \kappa = 0$, $c_v = 2.5$, $c_p = 3.5$. A set of reference pressures is considered to analyse the behaviour of the method for different Mach numbers, $M \in \{10^{-2}, 10^{-3}, 10^{-4}, 10^{-5}\}$. Dirichlet boundary conditions are imposed everywhere and we assume the vortex centre to be steady, i.e. $\mathbf{u}^{\mathrm{g}} = \mathbf{0}$. The errors and convergence rates obtained at time $t_{\mathrm{e}} = 0.1$ are reported in Table 4. The expected second order is achieved for all studied Mach numbers.

To numerically assess Galilean invariance [89,96] of the proposed approach, the isentropic vortex with $M = 10^{-3}$ is also performed by superimposing a uniform convection of the vortex in the $x - y$ plane with velocity $\mathbf{u}^{\mathrm{g}} = (1,1)^T$. Table 5 reports the resulting L^2-errors, computed by comparing the numerical solution against the time-shifted initial condition $\mathbf{Q}_{\mathrm{exact}}(\mathbf{x}, t_{\mathrm{e}}) = \mathbf{Q}_{\mathrm{exact}}(\mathbf{x} - \mathbf{u}^{\mathrm{g}} t_{\mathrm{e}}, 0)$. We observe that the errors are of the same order of those obtained for the non convected vortex, and the expected order of accuracy is recovered. Besides, M3 mesh at times $t \in \{0, 0.5, 1\}$ is shown in Fig. 4 to illustrate the convection of the vortex.

4.2. Riemann problems

To analyse the capability of the proposed approach to capture strong discontinuities arising in compressible media, we address a set of Riemann problems both in the fluid and solid limits of the model. In particular, we consider the computational domain

Table 4
2D isentropic vortex. Spatial L_2 error norms and convergence rates of the density, momentum, total energy and pressure at time $t = 0.1$ for $M \in \{10^{-2}, 10^{-3}, 10^{-4}, 10^{-5}\}$. Results computed using the second order ALE hybrid method.

Mesh	$L^2_\Omega(\rho)$	$\mathcal{O}(\rho)$	$L^2_\Omega(\rho\mathbf{u})$	$\mathcal{O}(\rho\mathbf{u})$	$L^2_\Omega(\mathcal{E})$	$\mathcal{O}(\mathcal{E})$	$L^2_\Omega(p)$	$\mathcal{O}(p)$
$M = 10^{-2}$, $p_0 = 10^4$ (double precision)								
M2	$1.25 \cdot 10^{-2}$		$6.58 \cdot 10^{-2}$		$5.58 \cdot 10^{1}$		$2.54 \cdot 10^{-1}$	
M3	$2.05 \cdot 10^{-3}$	2.61	$1.54 \cdot 10^{-2}$	2.10	$2.72 \cdot 10^{0}$	4.36	$6.03 \cdot 10^{-2}$	2.07
M4	$3.40 \cdot 10^{-4}$	2.59	$3.73 \cdot 10^{-3}$	2.05	$1.80 \cdot 10^{-1}$	3.92	$1.50 \cdot 10^{-2}$	2.01
M5	$6.03 \cdot 10^{-5}$	2.50	$9.27 \cdot 10^{-4}$	2.01	$1.55 \cdot 10^{-2}$	3.54	$3.63 \cdot 10^{-3}$	2.05
$M = 10^{-3}$, $p_0 = 10^6$ (double precision)								
M2	$1.26 \cdot 10^{-2}$		$6.59 \cdot 10^{-2}$		$5.58 \cdot 10^{3}$		$2.63 \cdot 10^{-1}$	
M3	$2.07 \cdot 10^{-3}$	2.60	$1.54 \cdot 10^{-2}$	2.09	$2.70 \cdot 10^{2}$	4.37	$5.91 \cdot 10^{-2}$	2.15
M4	$3.47 \cdot 10^{-4}$	2.58	$3.74 \cdot 10^{-3}$	2.04	$1.74 \cdot 10^{1}$	3.95	$1.49 \cdot 10^{-2}$	1.99
M5	$6.17 \cdot 10^{-5}$	2.49	$9.29 \cdot 10^{-4}$	2.01	$1.32 \cdot 10^{0}$	3.73	$3.78 \cdot 10^{-3}$	1.98
$M = 10^{-4}$, $p_0 = 10^8$ (quadruple precision)								
M2	$1.26 \cdot 10^{-2}$		$6.59 \cdot 10^{-2}$		$5.58 \cdot 10^{5}$		$5.63 \cdot 10^{0}$	
M3	$2.07 \cdot 10^{-3}$	2.60	$1.54 \cdot 10^{-2}$	2.09	$2.70 \cdot 10^{4}$	4.37	$6.17 \cdot 10^{-2}$	6.51
M4	$3.47 \cdot 10^{-4}$	2.58	$3.74 \cdot 10^{-3}$	2.04	$1.74 \cdot 10^{3}$	3.96	$1.50 \cdot 10^{-2}$	2.04
M5	$6.17 \cdot 10^{-5}$	2.49	$9.30 \cdot 10^{-4}$	2.01	$1.31 \cdot 10^{2}$	3.73	$4.18 \cdot 10^{-3}$	1.85
$M = 10^{-5}$, $p_0 = 10^{10}$ (quadruple precision)								
M2	$1.26 \cdot 10^{-2}$		$6.59 \cdot 10^{-2}$		$5.58 \cdot 10^{7}$		$5.63 \cdot 10^{2}$	
M3	$2.07 \cdot 10^{-3}$	2.60	$1.54 \cdot 10^{-2}$	2.09	$2.70 \cdot 10^{6}$	4.37	$1.80 \cdot 10^{0}$	8.29
M4	$3.47 \cdot 10^{-4}$	2.58	$3.74 \cdot 10^{-3}$	2.04	$1.74 \cdot 10^{5}$	3.96	$2.04 \cdot 10^{-1}$	3.14
M5	$6.17 \cdot 10^{-5}$	2.49	$9.30 \cdot 10^{-4}$	2.01	$1.31 \cdot 10^{4}$	3.73	$2.35 \cdot 10^{-1}$	−0.02

Table 5
2D isentropic vortex. Spatial L_2 error norms and convergence rates of the density, momentum, total energy and pressure at time $t = 0.1$ for $M = 10^{-3}$ and $\mathbf{u}^{\mathrm{g}} = (1, 1)^T$. Results computed using the second order ALE hybrid method.

Mesh	$L^2_\Omega(\rho)$	$\mathcal{O}(\rho)$	$L^2_\Omega(\rho\mathbf{u})$	$\mathcal{O}(\rho\mathbf{u})$	$L^2_\Omega(\mathcal{E})$	$\mathcal{O}(\mathcal{E})$	$L^2_\Omega(p)$	$\mathcal{O}(p)$
M2	$8.60 \cdot 10^{-3}$		$8.27 \cdot 10^{-2}$		$4.39 \cdot 10^{3}$		$2.20 \cdot 10^{-1}$	
M3	$1.18 \cdot 10^{-3}$	2.87	$1.68 \cdot 10^{-2}$	2.30	$1.84 \cdot 10^{2}$	4.58	$5.61 \cdot 10^{-2}$	1.97
M4	$1.53 \cdot 10^{-4}$	2.95	$3.85 \cdot 10^{-3}$	2.13	$1.10 \cdot 10^{1}$	4.07	$1.48 \cdot 10^{-2}$	1.93
M5	$2.27 \cdot 10^{-5}$	2.75	$9.36 \cdot 10^{-4}$	2.04	$9.37 \cdot 10^{-1}$	3.55	$3.79 \cdot 10^{-3}$	1.96

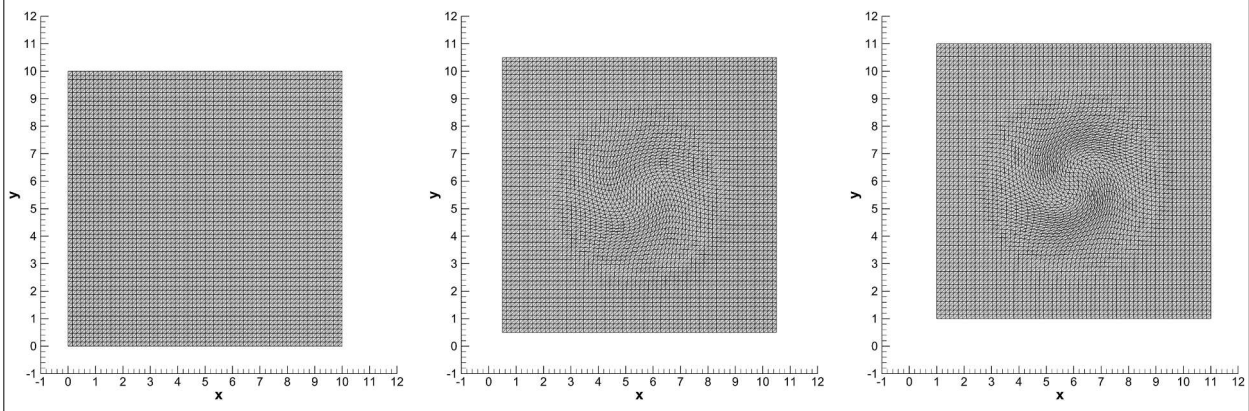

Fig. 4. 2D isentropic vortex. Initial $M3$ mesh (left) and deformed mesh at $t = 0.5$ (centre) and $t = 1$ (right) considering the vortex convection velocity $\mathbf{u}^{\mathrm{g}} = (1, 1)^T$.

$\Omega = [-0.5, 0.5] \times [-0.05, 0.05]$ and define the initial condition for the primitive variables $\mathbf{V} = (\rho, \mathbf{u}, \mathbf{A}, \mathbf{J}, p)$ as

$$\mathbf{V}(\mathbf{x}, 0) = \begin{cases} \mathbf{V}^L & \text{if } x \leq x_d, \\ \mathbf{V}^R & \text{if } x > x_d, \end{cases}$$

Table 6
Riemann problems. Initial condition, location of the initial discontinuity, x_d, and final time, t_{end}.

Test	ρ^L	ρ^R	u_1^L	u_1^R	u_2^L	u_2^R	p^L	p^R	x_c	t_e
RP1	1	0.125	0	0	0	0	1	0.1	0	0.2
RP2	1	1	−1	1	0	0	0.4	0.4	0	0.15
RP3	1	0.125	0.5	0	0	0	1	1	0	0.1
RP4	5.99924	5.99242	19.5975	−6.19633	0	0	460.894	46.095	−0.2	0.035
RP5	1	1	−19.59745	−19.59745	0	0	1000	0.01	0.3	0.01
RP6	1	1	2	−2	0	0	0.1	0.1	0	0.8
RP7	1	0.125	0.5	0	0	0	1	1	0	0.1
RP8–9	1	0.5	0	0	−0.2	0.2	1	0.5	0	0.2

Table 7
Riemann problems. Material parameters for the GPR model.

Test	c_s	c_h	c_v	c_p	μ	κ
RP1-7	0	0	2.5	3.5	0	0
RP8	1	0	1	1.4	10^{20}	10^{20}
RP9	1	1	1	1.4	10^{20}	10^{20}

with the remaining left and right states, ρ^L, $\mathbf{u}^L$, p^L, ρ^R, $\mathbf{u}^R$, p^R, the initial position of the discontinuity, x_d, the final simulation time, t_e, and the number of mesh divisions along the x-axis given in Table 6. The material parameters for each test case are provided in Table 7.

Riemann problems RP1–RP7 correspond to classical tests for inviscid flows and, therefore, an exact Riemann solver for the Euler equations has been employed to get the exact solution of the density, pressure and velocity fields [93]. In Fig. 5, we report the results obtained for the Sod shock tube problem which presents a shock, a contact discontinuity and a rarefaction wave. For this Riemann problem both the purely Eulerian and the ALE scheme with $\varsigma = 5$ have been run. The numerical solution computed using the HTC FV scheme in [25] has also been included for comparison. Figs. 6 and 10 show the solutions obtained for a double rarefaction, RP2, and a double shock, RP6, tests. Combined waves are analysed through the Lax benchmark (RP3), RP4, where two shock colliding waves lead to three strong discontinuities, and RP7, where a shock presenting a small wave in the density field is generated. The obtained results are reported in Figs. 7, 8 and 11. Finally, Fig. 9 depicts the solution obtained for the severe left blast problem introduced in [97].

On the other hand, test cases RP8, RP9 are classically employed to specifically assess numerical methods in the solid limit of the GPR model [24,36]. The initial condition coincides for both tests but different media are considered: RP8 corresponds to an ideal elastic solid without heat conduction and RP9 incorporates heat conduction. As expected, a contact discontinuity, two acoustic and two shear waves plus two additional thermo-acoustic waves, when accounting for heat conduction, are generated, see Figs. 12–13. The provided reference solutions have been computed using the thermodynamically compatible scheme (HTC) proposed in [25], which solves the entropy equation instead of the total energy conservation law.

All solutions of the semi-implicit hybrid methodology have been computed using an ENO limiting strategy on the primitive variables. The artificial viscosity has been activated with values $c_\alpha = 0.2$ for RP1 and RP7, $c_\alpha = 2$ for RP2 and RP6, $c_\alpha = 0.5$ for RP3, $c_\alpha = 5$ for RP4, $c_\alpha = 10$ for RP5 and $c_\alpha = 1$ for RP8-9. A structured mesh of $N_x = 400$ divisions along the x-axis has been employed for all test cases except for RP5 and RP10, which have been run on grids of $N_x = 800$ and $N_x = 2000$ divisions, respectively. Overall, the results obtained show a good agreement with the exact and reference solutions in presence of strong waves.

4.3. Fluid and solid circular explosions

We now analyse two circular explosion test cases designed to trigger genuinely multidimensional wave-propagation effects. The first one corresponds to the radial extension of the Sod shock tube problem [52], i.e. an inviscid flow with $c_s = c_h = 0$ and $\mu = \kappa = 0$, and initial condition given by

$$\rho(\mathbf{x},0) = \begin{cases} 1 & \text{if } r \le 0.5, \\ 0.125 & \text{if } r > 0.5, \end{cases} \qquad \mathbf{u}(\mathbf{x},0) = \mathbf{0}, \qquad p(\mathbf{x},0) = \begin{cases} 1 & \text{if } r \le 0.5, \\ 0.1 & \text{if } r > 0.5, \end{cases} \qquad r = \sqrt{x^2 + y^2}.$$

The results obtained at $t_e = 0.25$ using the hybrid FV/FE method with ENO limiting are depicted in Fig. 14. For comparison, we include a reference solution computed solving, with a TVD-FV scheme, the 1D radial PDE with source terms equivalent to the compressible Euler system [98].

The second circular Riemann problem regards a solid medium [36]. We set $\tau_1 = \tau_2 = 10^{20}$, $\rho_0 = 1$, $c_v = 1.0$, $c_s = 1$, $c_h = 0.5$, $\gamma = 1.4$, and the initial condition

$$\rho(\mathbf{x},0) = 1, \quad \mathbf{u}(\mathbf{x},0) = \mathbf{0}, \quad p(\mathbf{x},0) = \begin{cases} 2 & \text{if } r \le 0.5, \\ 1 & \text{if } r > 0.5. \end{cases}$$

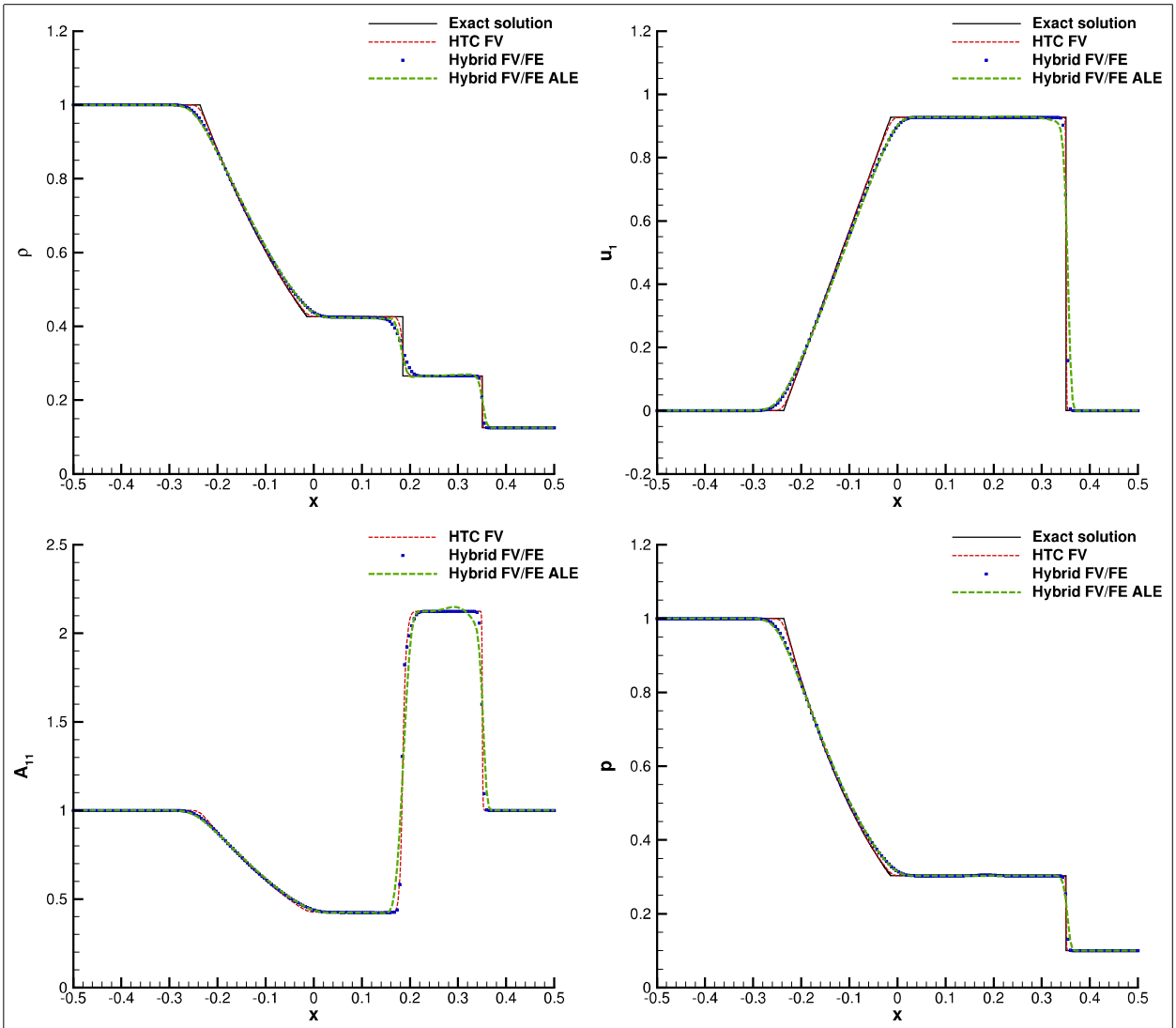

Fig. 5. RP1 Sod. 1D cuts of the solution obtained using the hybrid FV/FE method for the compressible GPR model with the fully Eulerian code (blue squares) and the ALE scheme (green dashed line) compared against the exact solution for the Navier-Stokes equations (black line) and the solution of the GPR model obtained using the HTC FV scheme in [25] (red dashed line). From left-top to right-bottom: density, horizontal velocity component, distortion field component A_{11}, and pressure. (For interpretation of the references to colour in this figure legend, the reader is referred to the web version of this article.)

As aforementioned, in the solid limit the GPR model presents curl-free-type involution constraints for the distortion and heat flux fields. To analyse the behaviour of the proposed GLM cleaning strategy a set of simulations for $c_{\mathbf{A}}$, $c_{\mathbf{J}} \in \{0, 5, 10, 20, 50, 100\}$ has been run for the solid circular explosion test case. The obtained curl errors are depicted in Fig. 15. As expected, we observe the decay of $\nabla\times A$ and $\nabla\times J$ for increasing values of the cleaning speeds. Besides, the contour plots of density, A_{11} and J_1 obtained at time $t_e = 0.15$ are depicted in Fig. 16. To ease comparison with available reference data, the solution for a 1D cut along the positive part of the x-axis are reported in Fig. 17. The solutions are presented for both the fully Eulerian scheme and the ALE method with a smoothing parameter for the mesh velocity $\varsigma = 5$.

4.4. 3D explosion

In this section, the 3D extension of the Sod problem is studied. As computational domain, we define the unit sphere centred at the origin which is discretized employing a primal mesh made of 8082535 tetrahedral elements. The initial condition is given by

$$\rho(\mathbf{x},0) = \begin{cases} 1 & \text{if } r \le 0.5, \\ 0.125 & \text{if } r > 0.5, \end{cases} \qquad p(\mathbf{x},0) = \begin{cases} 1 & \text{if } r \le 0.5, \\ 0.1 & \text{if } r > 0.5, \end{cases} \qquad \mathbf{u}(\mathbf{x},0) = \mathbf{0}, \qquad r = \sqrt{x^2 + y^2 + z^2},$$

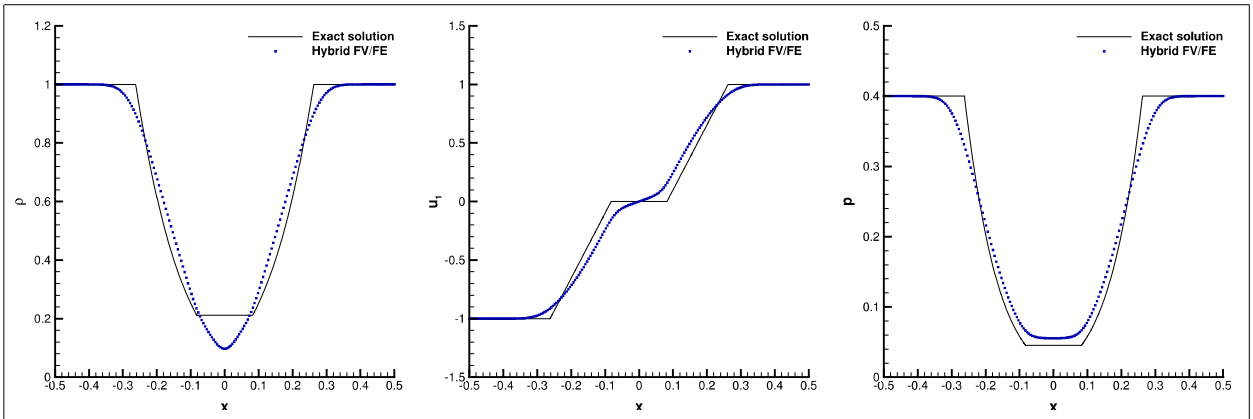

Fig. 6. RP2 smooth double rarefaction. 1D cuts of the solution obtained using the hybrid FV/FE method for the compressible GPR model (blue squares) compared against the exact solution (black line). From left to right: density, horizontal velocity component and pressure. (For interpretation of the references to colour in this figure legend, the reader is referred to the web version of this article.)

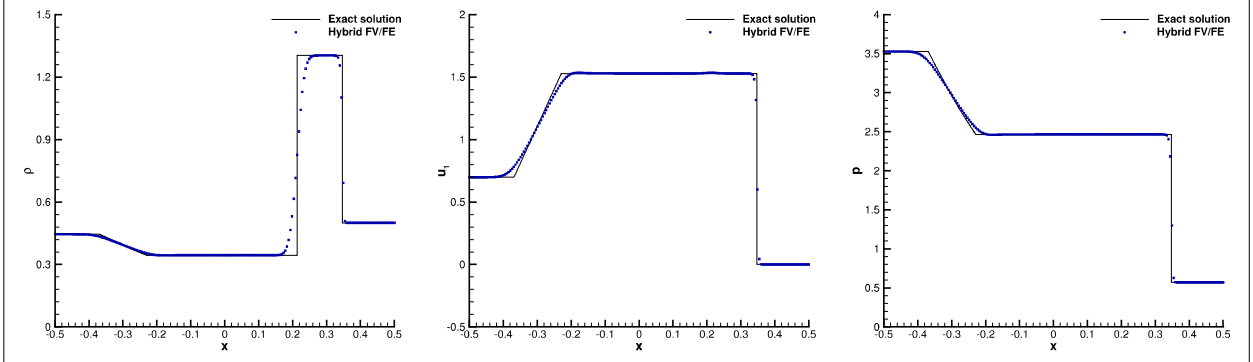

Fig. 7. RP3 Lax. 1D cuts of the solution obtained using the hybrid FV/FE method for the compressible GPR model (blue squares) compared against the exact solution (black line). From left to right: density, horizontal velocity component and pressure. (For interpretation of the references to colour in this figure legend, the reader is referred to the web version of this article.)

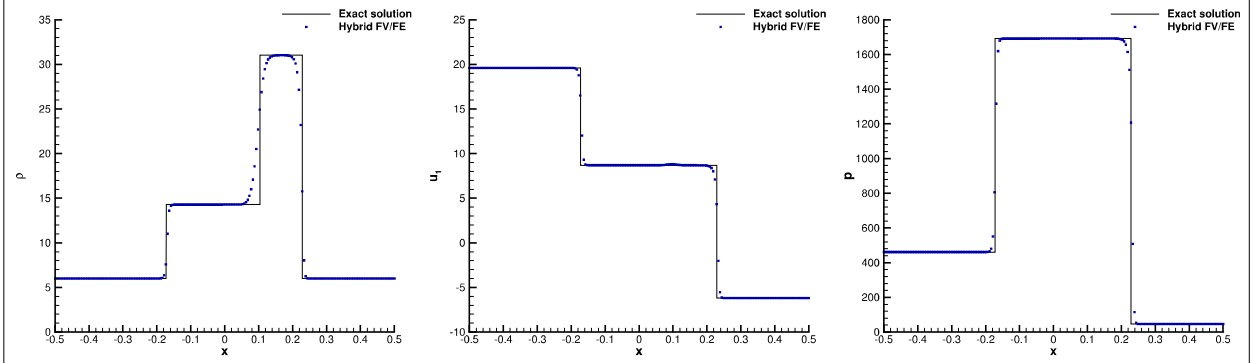

Fig. 8. RP4. 1D cuts of the solution obtained using the hybrid FV/FE method for the compressible GPR model (blue squares) compared against the exact solution (black line). From left to right: density, horizontal velocity component and pressure. (For interpretation of the references to colour in this figure legend, the reader is referred to the web version of this article.)

while the model parameters read $c_s = c_h = 0$, $\mu = \kappa = 0$, $c_v = 2.5$ and $\gamma = 1.4$. Dirichlet boundary conditions are defined in the outer boundary. The simulation is run employing the ENO limiting strategy based on physical variables and setting $c_\alpha = 1$. The solution obtained at $t_e = 0.25$ is depicted in Figs. 18–19. We observe a good agreement with the reference solution computed with a TVD-FV solver of the corresponding 1D radial PDE.

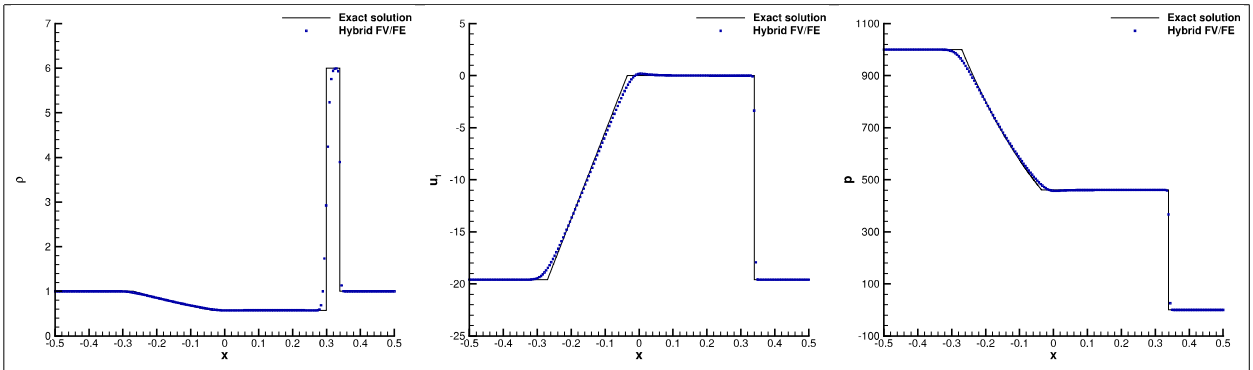

Fig. 9. RP5 left blast problem. 1D cuts of the solution obtained using the hybrid FV/FE method for the compressible GPR model (blue squares) compared against the exact solution (black line). From left to right: density, horizontal velocity component and pressure. (For interpretation of the references to colour in this figure legend, the reader is referred to the web version of this article.)

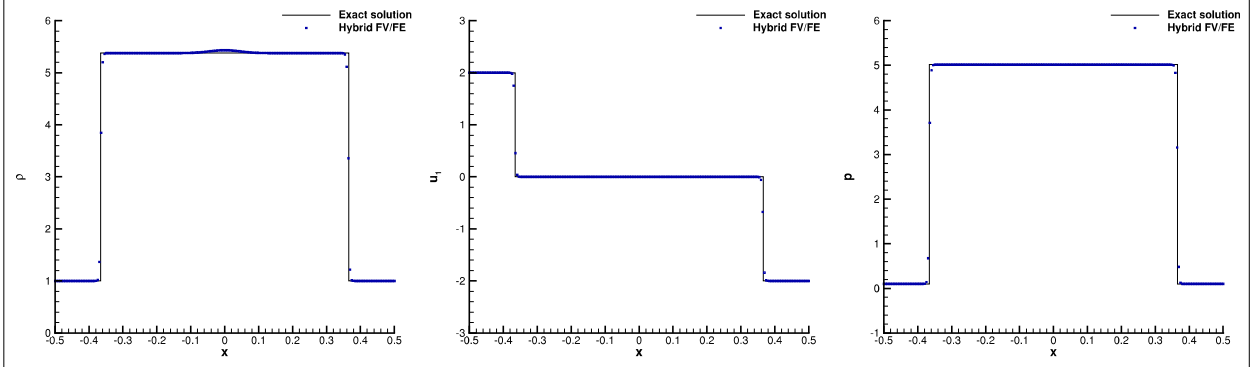

Fig. 10. RP6 double shock. 1D cuts of the solution obtained using the hybrid FV/FE method for the compressible GPR model (blue squares) compared against the exact solution (black line). From left to right: density, horizontal velocity component and pressure. (For interpretation of the references to colour in this figure legend, the reader is referred to the web version of this article.)

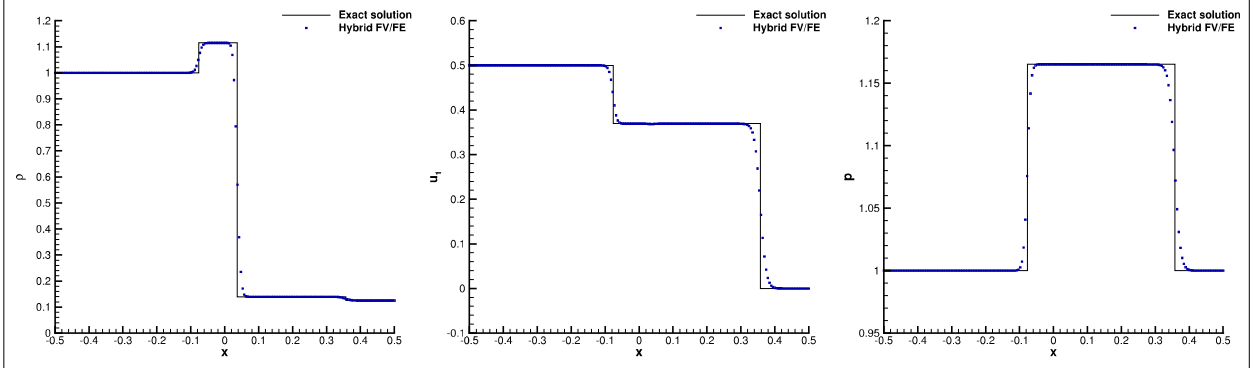

Fig. 11. RP7. 1D cuts of the solution obtained using the hybrid FV/FE method for the compressible GPR model (blue squares) compared against the exact solution (black line). From left to right: density, horizontal velocity component and pressure. (For interpretation of the references to colour in this figure legend, the reader is referred to the web version of this article.)

4.5. Shear motion

To analyse the behaviour of the proposed approach for different shears, we consider a shear test in solid mechanics and the First Stokes problem for fluid dynamics with viscosities $\mu \in \{10^{-4}, 10^{-3}, 10^{-2}\}$. Further, we take $c_s = c_h = 1$, $c_v = 2.5$ and $\gamma = 1.4$ and $\mu = \kappa = 10^{20}$ for the solid test case. The initial conditions are given by a Riemann-type problem with

$$\rho(\mathbf{x}, 0) = 1, \quad p(\mathbf{x}, 0) = \frac{1}{\gamma}, \quad u_1(\mathbf{x}, 0) = 0, \quad u_2(\mathbf{x}, 0) = \begin{cases} -0.1 & \text{if } y \leq 0, \\ 0.1 & \text{if } y > 0. \end{cases}$$

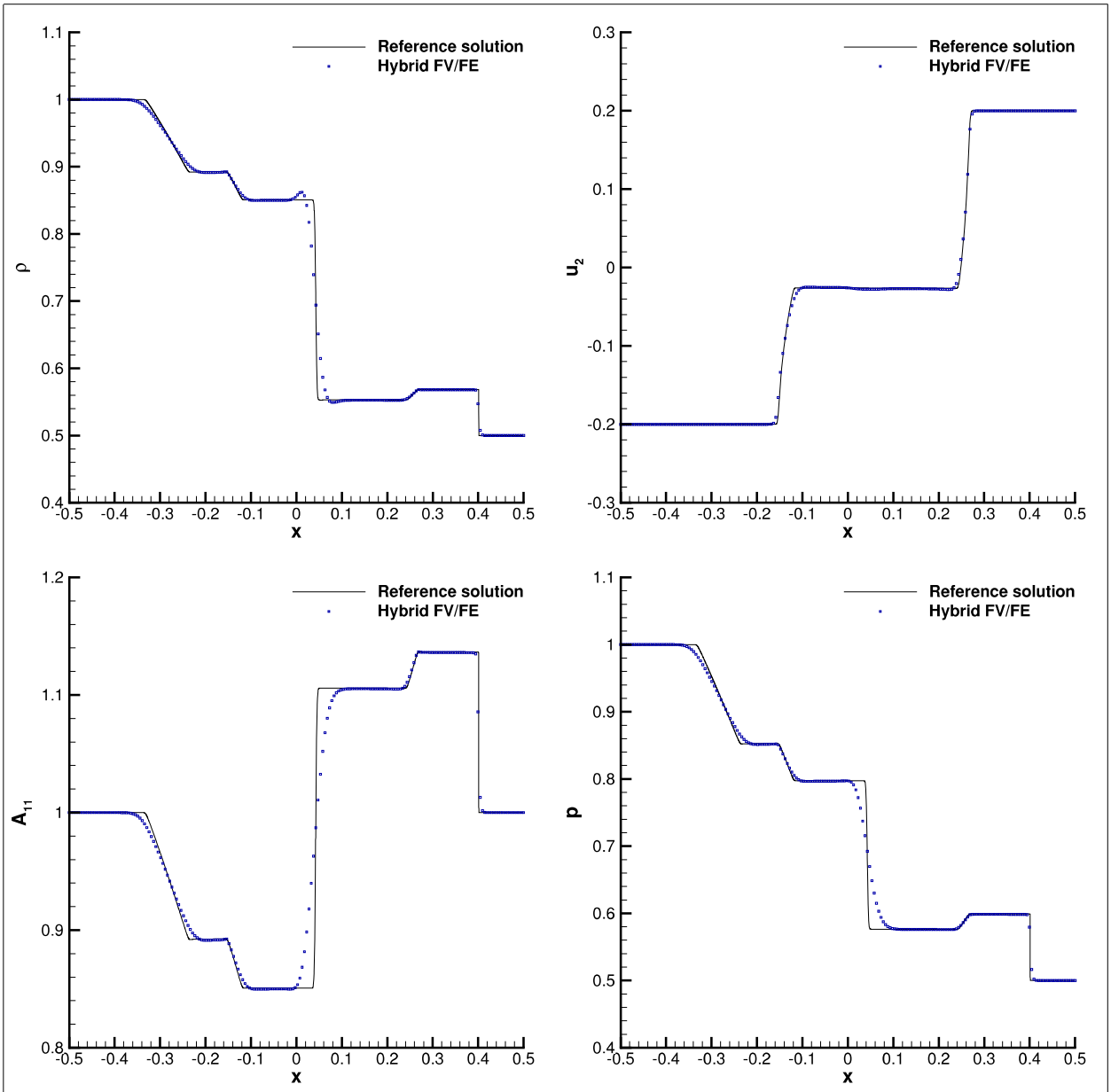

Fig. 12. RP8. 1D cuts of the solution obtained using the hybrid FV/FE method for the compressible GPR model (blue squares) compared against the reference solution computed using the HTC method proposed in [25] (black line). From left-top to right-bottom: density, velocity component u_2, distortion field component A_{11} and pressure. (For interpretation of the references to colour in this figure legend, the reader is referred to the web version of this article.)

We define the computational domain $\Omega = [-0.5, 0.5] \times [-0.05, 0.05]$ which is discretized employing a regular Cartesian triangular grid made of $N_x = 400$ divisions along the x-axis. We define strong Dirichlet boundary conditions at the left and right boundaries of the domain while periodic conditions are imposed in y-direction. The 1D cut of the velocity field component u_2 approximated at time $t_e = 0.4$ is depicted in Fig. 20. For the fluid test cases, the known analytical solution

$$u_2(\mathbf{x}, t) = \frac{1}{10}\mathrm{erf}\left(\frac{x}{2\sqrt{\mu t}}\right),$$

is also reported while a reference solution, computed using a TVD-FV scheme on a very fine one-dimensional grid, is included for validation of the shear solid test case. An excellent agreement is observed in all setups.

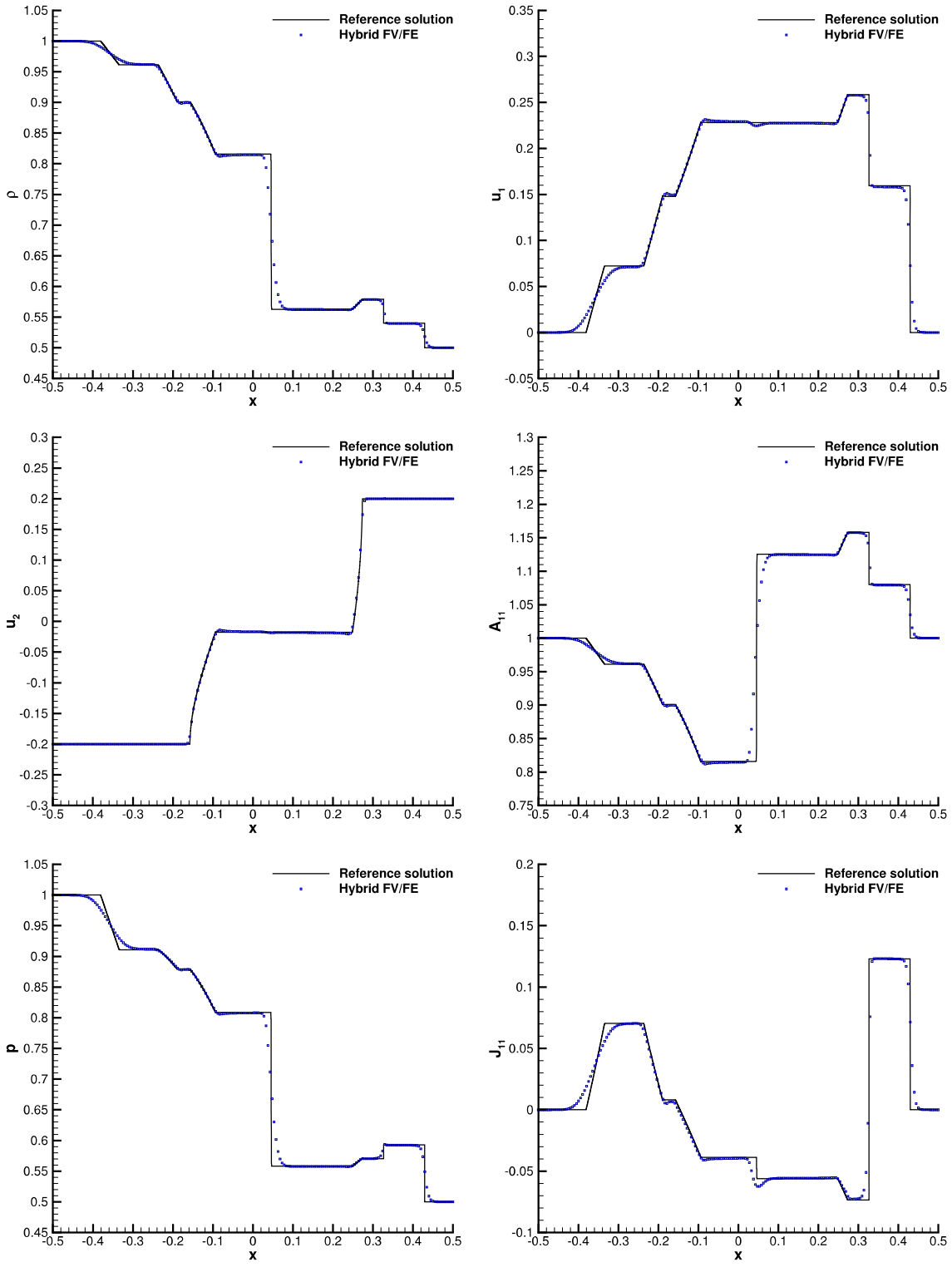

Fig. 13. RP9. 1D cuts of the solution obtained using the hybrid FV/FE method for the compressible GPR model (blue squares) compared against the reference solution computed using the HTC method proposed in [25] (black line). From left-top to right-bottom: density, velocity components u_1, u_2, distortion field component A_{11}, pressure and thermal impulse J_1. (For interpretation of the references to colour in this figure legend, the reader is referred to the web version of this article.)

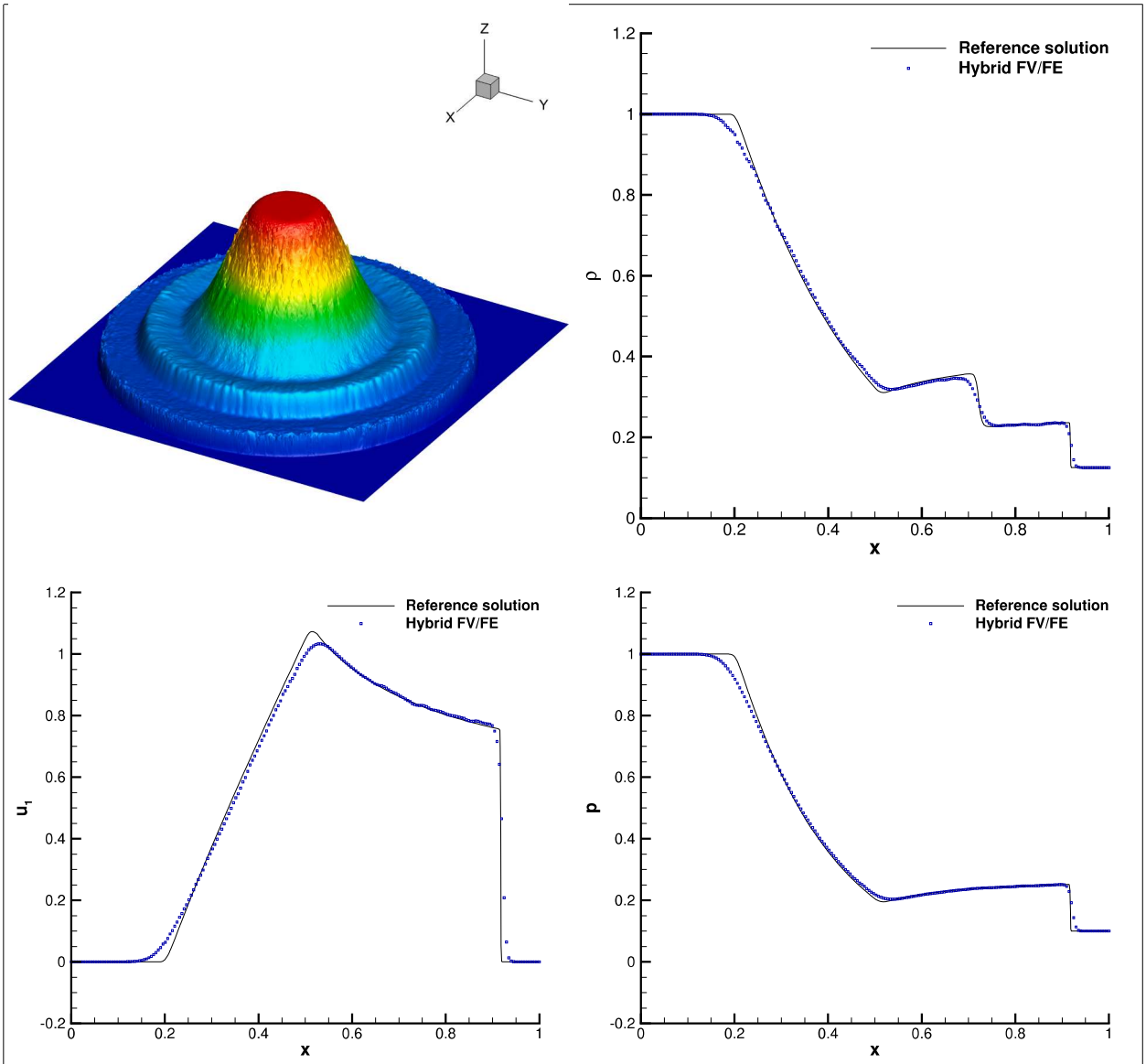

Fig. 14. Fluid circular explosion 2D. 3D extrusion of the density field and 1D cuts of the density, u_1 and pressure for $\{(x, y) \in \mathbb{R}^2 \,|\, x \in [0, 1],\ y = 0\}$ using the hybrid method (blue squares) compared against the reference solution (black line). (For interpretation of the references to colour in this figure legend, the reader is referred to the web version of this article.)

4.6. *Double shear layer*

The double shear layer is a classical test in fluid dynamics yielding complex flow patterns in the distortion field components when the GPR model is solved [25,27]. Hence it allows verification of numerical methods in the presence of thin sharp flow structures. In particular, we consider the initial condition in the computational domain $\Omega = [0, 1]^2$ given by

$$\rho(\mathbf{x}, 0) = 1, \quad u_1(\mathbf{x}, 0) = \begin{cases} \tanh(30(y - 0.25)) & \text{if } y \leq 0.5, \\ \tanh(30(0.75 - y)) & \text{if } y > 0.5, \end{cases} \quad u_2(\mathbf{x}, 0) = 0.05 \sin(2\pi x), \quad p(\mathbf{x}, 0) = 0$$

and we set the model parameters as $c_p = 3.5$, $c_s = \sqrt{2}$, $c_s = 8$, $c_v = 2.5$, $\mu = \kappa = 2 \cdot 10^{-3}$. The second order Eulerian hybrid scheme is run up to time $t_e = 1.8$ with CFL $= 0.25$ using a primal Cartesian mesh made of 524288 triangular elements. The contour plots of the distortion field component A_{12}, reported in Fig. 21, agree well with the solutions obtained for the incompressible GPR model and the weakly compressible approach in [38].

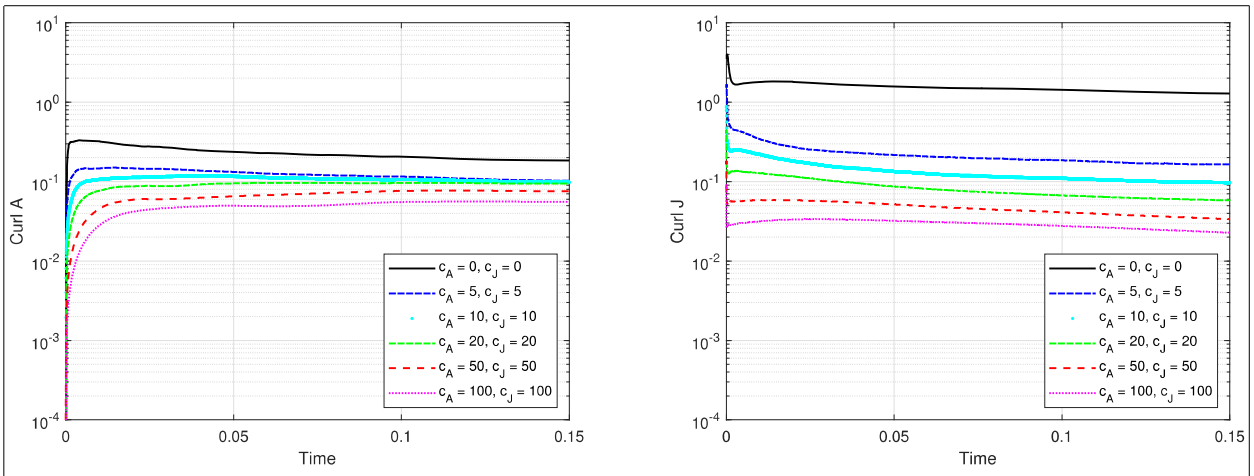

Fig. 15. Solid circular explosion. Time evolution of the curl errors for the distortion field, **A**, (left) and the thermal impulse, **J**, (right) for cleaning speeds $c_{\mathbf{A}}$, $c_{\mathbf{J}} \in \{0, 5, 10, 20, 50, 100\}$.

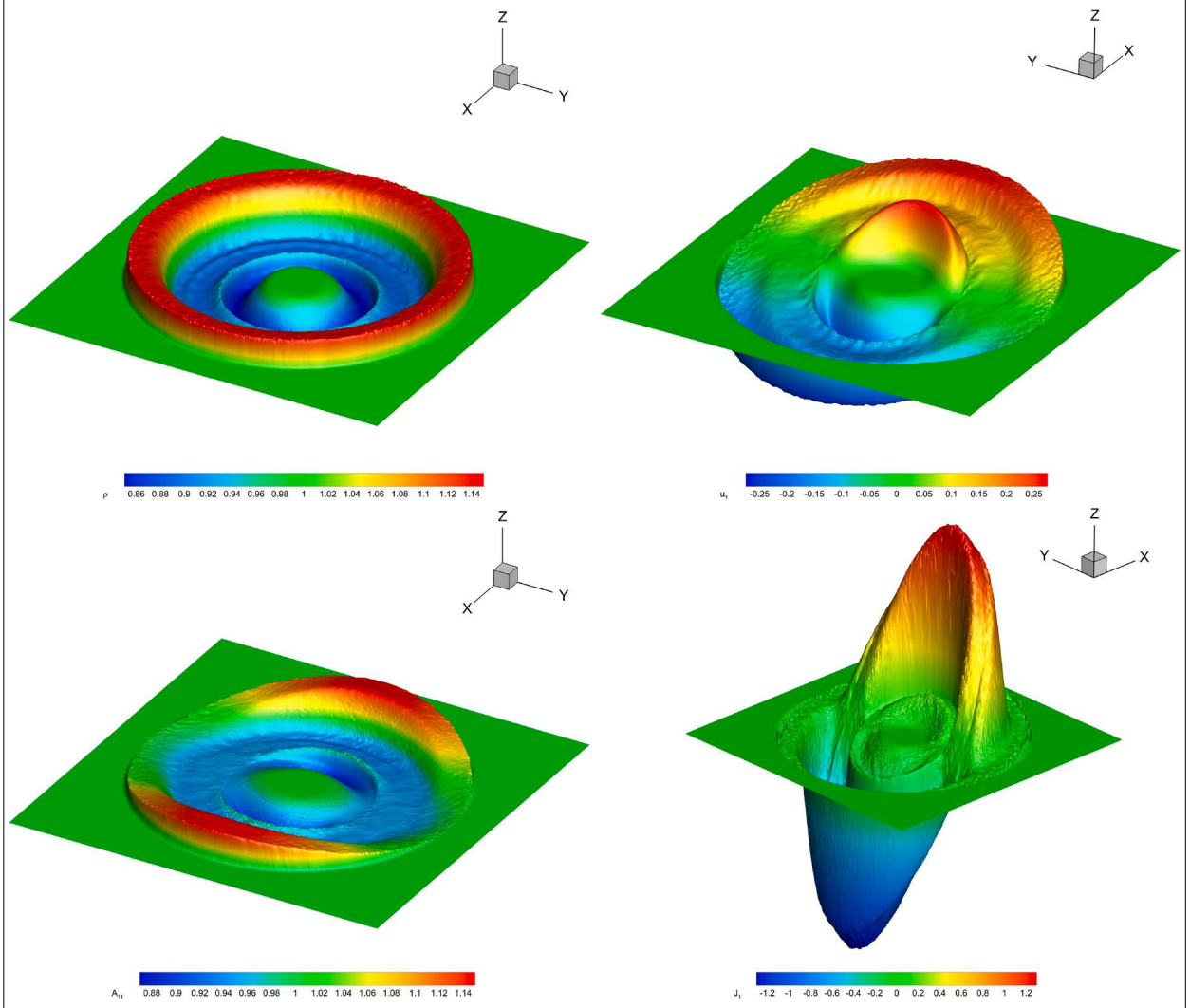

Fig. 16. Solid circular explosion 2D. Elevated contour plots of the density, u_1, A_{11} and J_1 for $\{(x, y) \in \mathbb{R}^2 \,|\, x \in [0, 1],\ y = 0\}$ using the hybrid FV/FE method for the compressible GPR model.

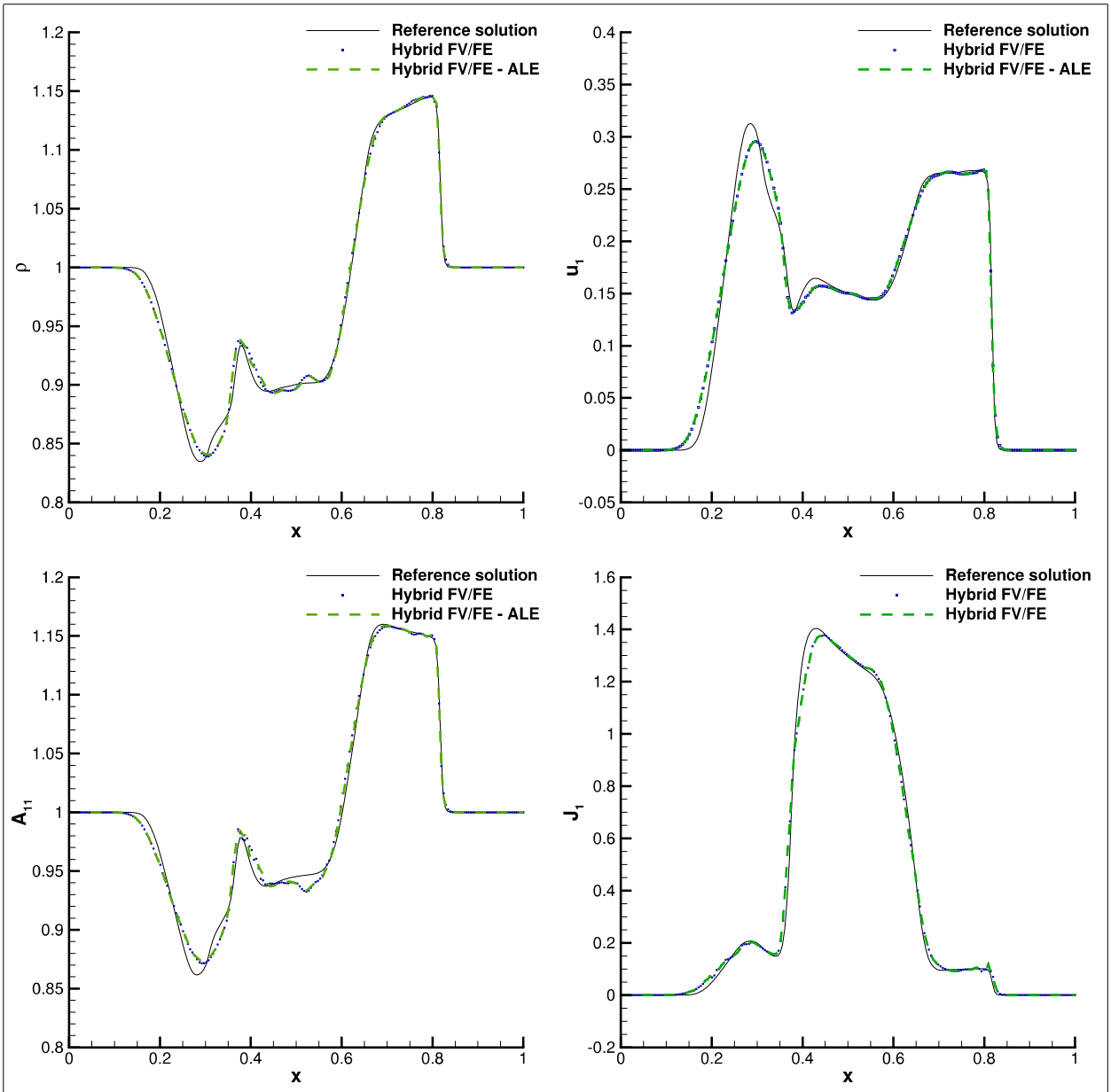

Fig. 17. Solid circular explosion 2D. 1D cuts of the density, u_1, A_{11} and J_1 for $\{(x, y) \in \mathbb{R}^2 \mid x \in [0, 1],\ y = 0\}$ using the hybrid FV/FE method for the compressible GPR model with the Eulerian scheme (blue squares) and with the ALE method (green dashed line) compared against the reference solution (black line). (For interpretation of the references to colour in this figure legend, the reader is referred to the web version of this article.)

4.7. Smooth acoustic wave

To analyse the behaviour of the proposed approach for flows dominated by acoustic waves, we consider the acoustic wave benchmark [32]. The initial condition defined in $\Omega = [-2, 2]^2$ is given by

$$\rho(\mathbf{x}, 0) = 1, \quad \mathbf{u}(\mathbf{x}, 0) = \mathbf{0}, \quad p(\mathbf{x}, 0) = 1 + e^{-40r^2}$$

with $r = \sqrt{x^2 + y^2}$. As model parameters, we set $\mu = \kappa = c_s = 0$, $c_h = 10^{-10}$, $c_v = 1$, $c_p = 1.4$. A first simulation is run using the hybrid FV/FE method without limiters on a Cartesian grid made of 2097152 primal triangular elements. The contour plots of the Mach number , A_{11} and A_{12}, and 1D cuts of the density, pressure and velocity component u_1 at time $t_e = 1$ are depicted in Figs. 22–23. The 1D plots also report the solution obtained using the ALE method with mesh speed smoothing $\varsigma = 5$. To ease validation, a reference solution computed with a second order TVD FV scheme on a very fine grid is included. We observe that the steep acoustic wave front is well captured with both schemes.

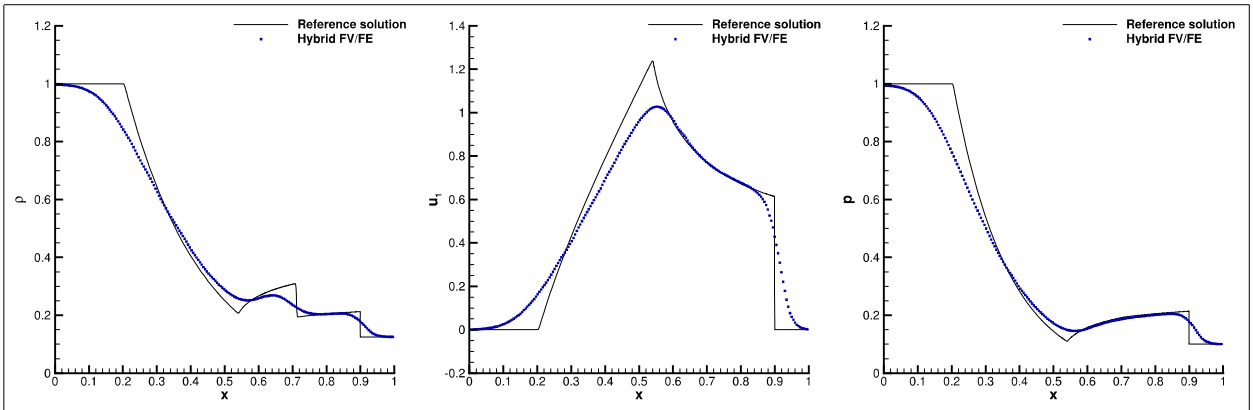

Fig. 18. 3D Sod explosion. 1D cuts of the density, u_1, and pressure for $\{(x, y, z) \in \mathbb{R}^3 \,|\, x \in [0, 1],\ y = 0,\ z = 0\}$ using the hybrid FV/FE method for the compressible GPR model (blue squares) compared against the reference solution (black line). (For interpretation of the references to colour in this figure legend, the reader is referred to the web version of this article.)

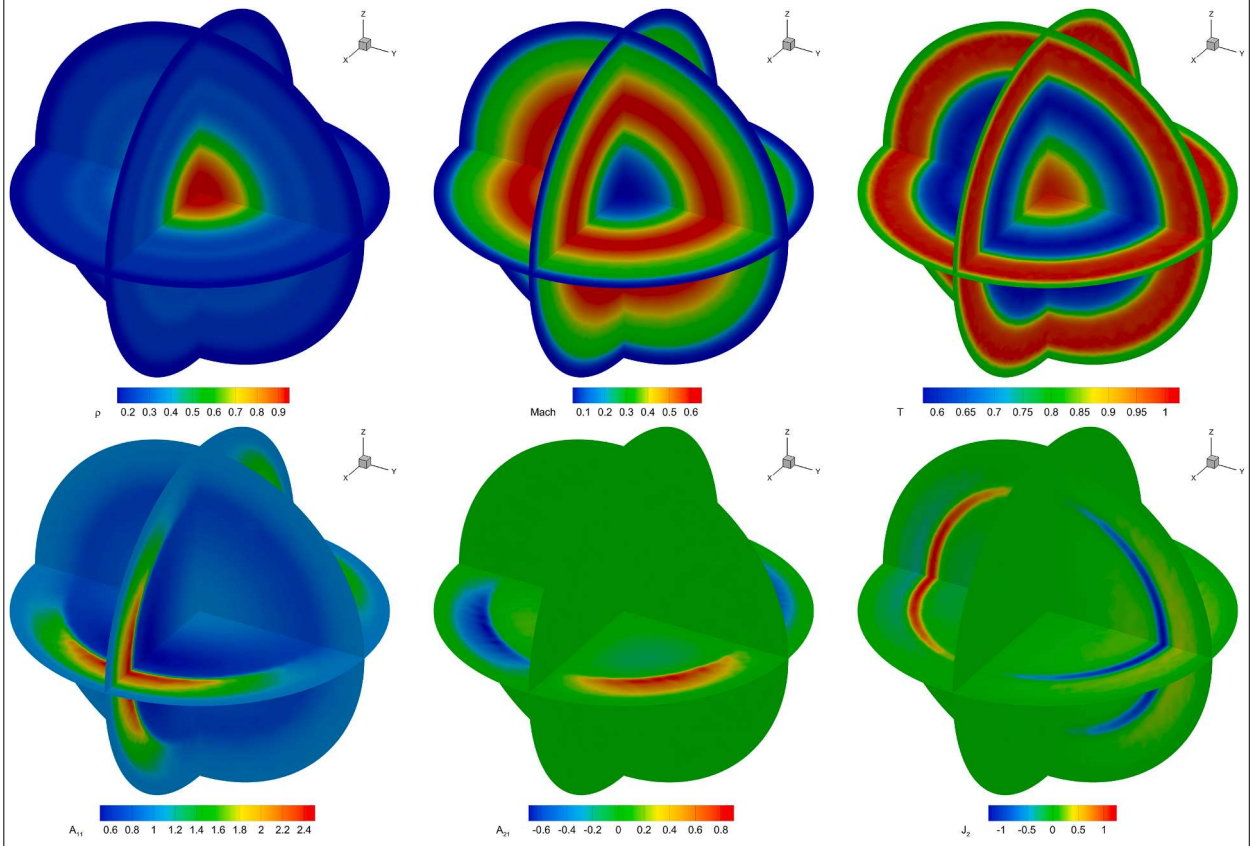

Fig. 19. 3D Sod explosion. Contour plots of the density, Mach number, temperature, A_{11}, A_{21} and J_2 for the 2D slices $x = 0$, $y = 0$ and $z = 0$.

4.8. Lid-driven cavity

A classical test case in fluid dynamics, commonly used to assess numerical methods for viscous incompressible flows, is the lid-driven cavity benchmark, for which we set $c_s = 8$, $c_h = 0$, $\mu = 10^{-2}$, $\kappa = 0$, $c_v = 1$, and $\gamma = 1.4$. In this test case, the fluid is assumed to be confined within a unit square cavity with a sliding lid at the top moving at velocity $\mathbf{u}_{\text{lid}} = (1, 0)^T$ and an initial fluid at rest. The computational domain is discretized employing an unstructured grid made of 185984 primal cells and strong wall boundary conditions are imposed in all boundaries. The results, computed at $t_c = 10$ using the asymptotic-preserving method with ENO limiting and $c_\alpha = 0.5$, are reported in Fig. 24. A good agreement is observed for the 1D cuts in comparison with the reference data in [99].

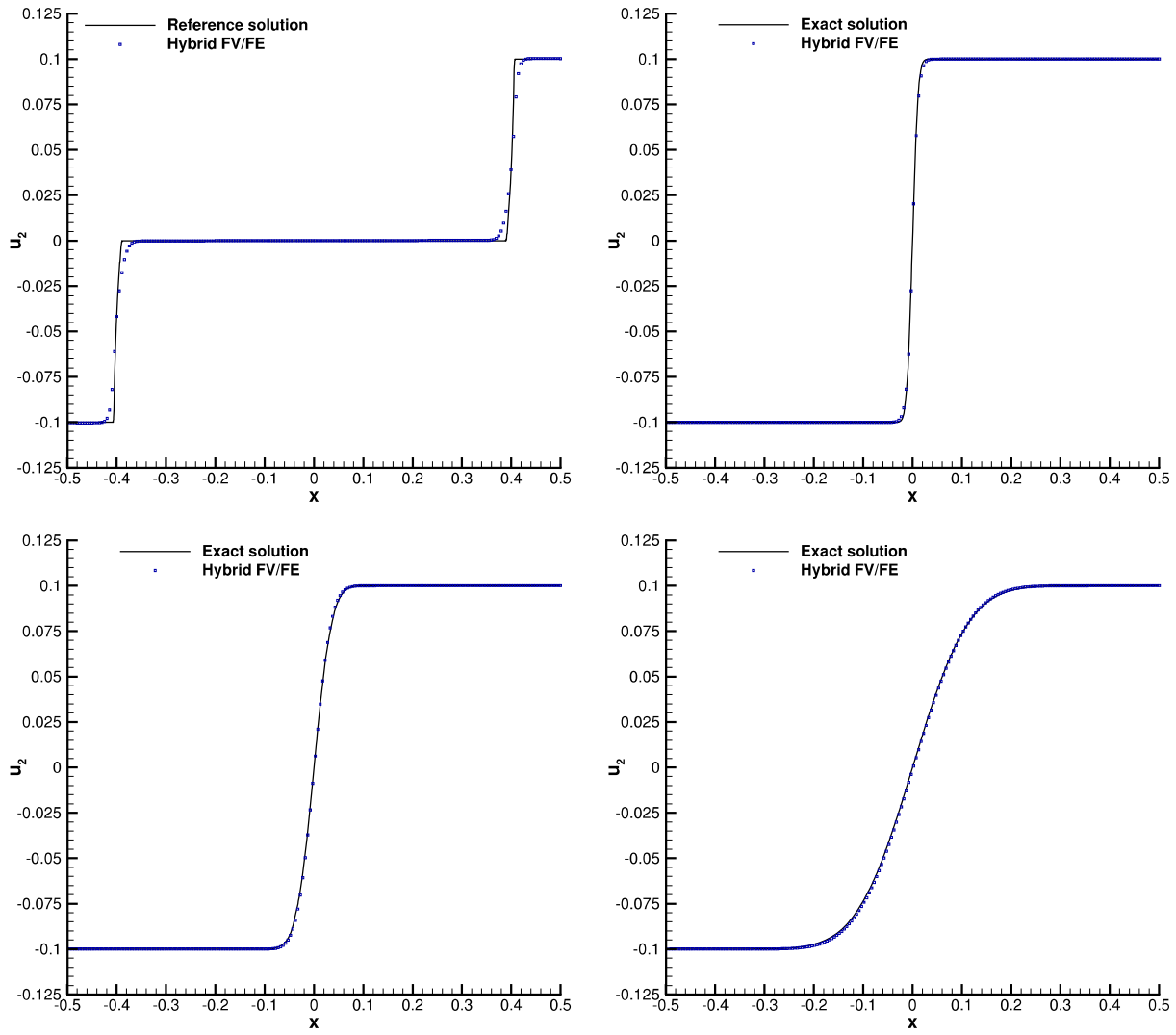

Fig. 20. First Stokes. 1D cuts along the x-direction of the velocity component u_2 computed using the Eulerian hybrid FV/FE method for the compressible GPR model (blue squares) compared against the exact and reference solutions (black line). From top left to right bottom: shear solid and first Stokes with $\mu \in \{10^{-4}, 10^{-3}, 10^{-2}\}$. (For interpretation of the references to colour in this figure legend, the reader is referred to the web version of this article.)

4.9. Solid rotor

The solid rotor test case is employed to further test the behaviour of the proposed numerical method in the solid limit of the GPR model [24,36,76]. The solution in the computational domain $\Omega = [-1, 1]^2$ is initialized as

$$\rho(\mathbf{x}, 0) = p(\mathbf{x}, 0) = 1, \quad \mathbf{u}(\mathbf{x}, 0) = \begin{cases} \left(\frac{-y}{0.2}, \frac{x}{0.2}, 0\right)^T & \text{if } \|\mathbf{x}\| \leq 0.2, \\ \mathbf{0} & \text{if } \|\mathbf{x}\| > 0.2. \end{cases}$$

while the model parameters are $c_s = c_h = 1$, $\tau_1 = 6 \cdot 10^{20}$, $\tau_2 = 10^{20}$, $p_0 = 0$, $c_v = 1$, $c_p = 1.4$. A simulation is run employing the hybrid FV/FE approach with ENO limiting and an implicit discretisation of the source terms. Besides, periodic boundary conditions are assumed in all boundaries and the final simulation time is $t_e = 0.3$. The obtained solution for representing variables is reported in Figs. 25–26. To ease comparison with reference solutions in the bibliography, 1D cuts of ρ, u_1, A_{11}, A_{12}, J_1 and p fields are reported in Fig. 27. An excellent agreement is observed for all variables with the numerical approaches proposed in [36,38,76]. The solution obtained with the hybrid methodology has been calculated using a very fine unstructured mesh made of 2975744 primal triangular elements which allows a detailed definition of the steepest wavefronts.

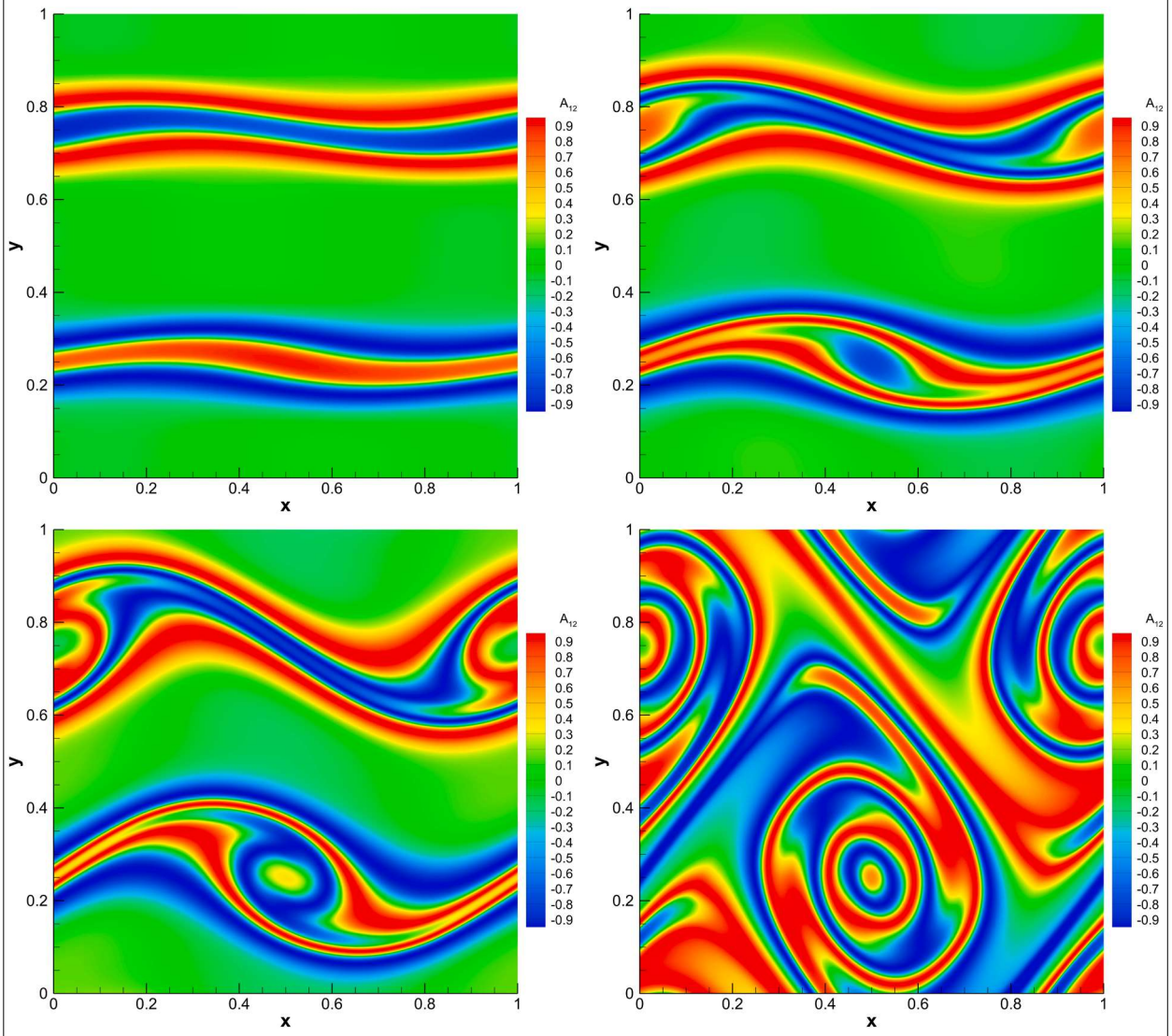

Fig. 21. Double shear layer. Contour plots of the distortion field component A_{12} for $t \in \{0.4, 0.8, 1.2, 1.8\}$.

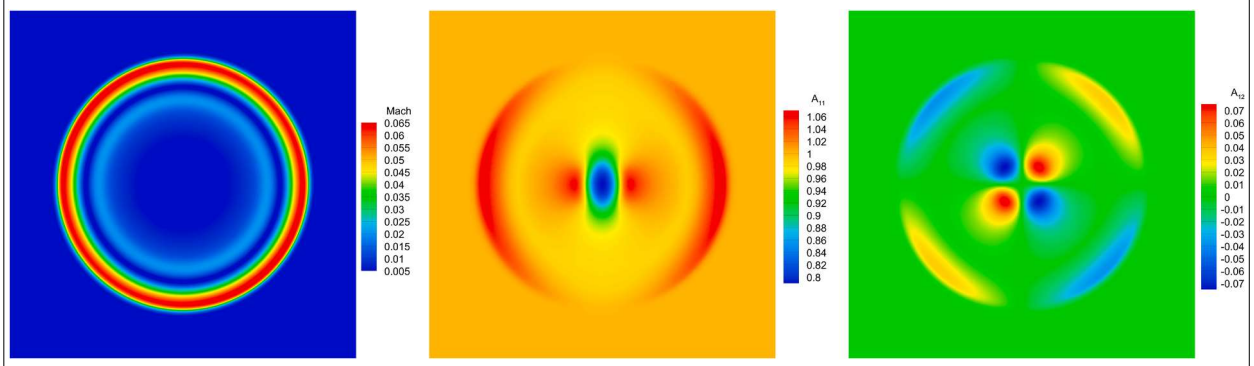

Fig. 22. Smooth acoustic wave. Contour plots of the Mach number, A_{11} and A_{12} fields computed using the hybrid FV/FE method for the compressible GPR model with the Eulerian scheme.

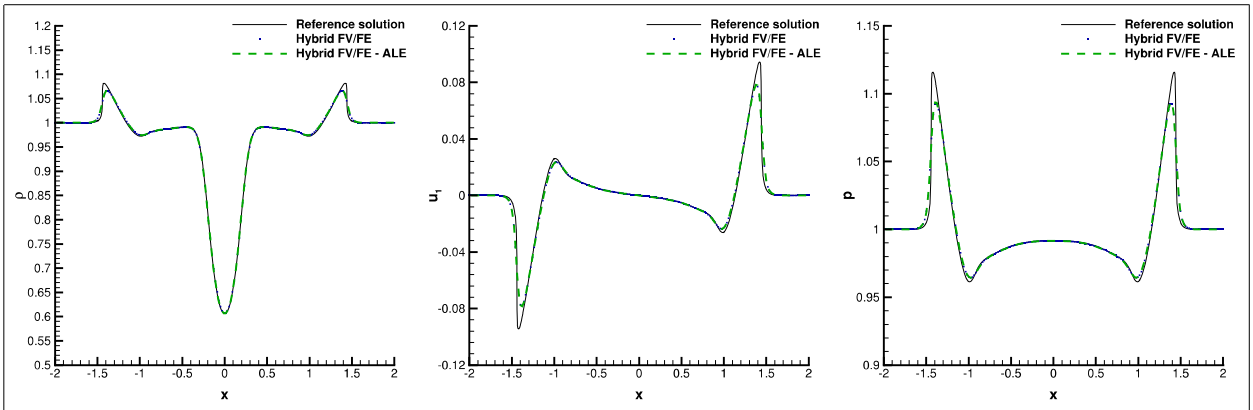

Fig. 23. Smooth acoustic wave. 1D cuts of the density, u_1, and pressure fields for $\{(x,y) \in \mathbb{R}^2 \,|\, x \in [-1,1],\ y = 0\}$ using the hybrid FV/FE method for the compressible GPR model with the Eulerian scheme (blue squares) and with the ALE method (green dashed line) compared against the reference solution (black line). (For interpretation of the references to colour in this figure legend, the reader is referred to the web version of this article.)

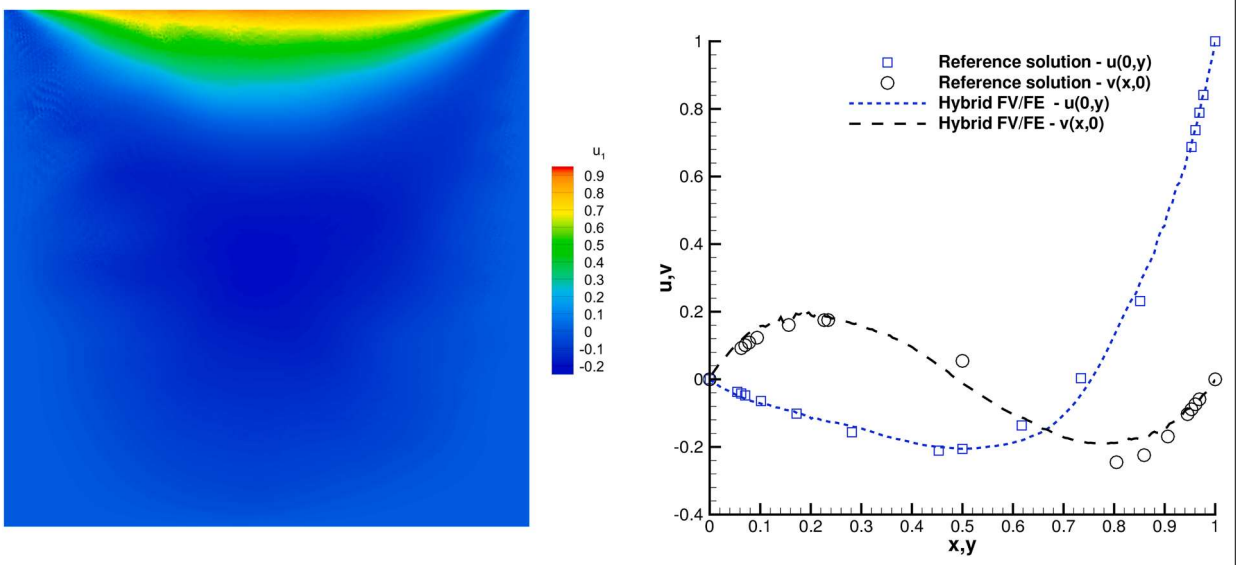

Fig. 24. Lid-driven cavity. Contour plot of the velocity field u_1 (left) and 1D cut in $x-$ and $y-$directions of the velocity components (right). The provided reference solution has been taken from [99].

4.10. Sloshing

The last test case corresponds to a sloshing of an inviscid fluid in a moving tank [43,100,101]. The initial computational domain is $\Omega_0 = [0, 1.73] \times [0, 0.6]$. The left, right and bottom boundaries of are assumed to be slip walls moving horizontally following

$$u_1(t) = -\omega A \sin(\omega t), \qquad A = 0.032, \qquad \omega = 2\frac{\pi}{T}, \qquad T = 1.3. \tag{77}$$

Further, the fluid is left free in the top boundary allowing for the sloshing phenomena to occur. To this end, a pressure boundary condition with $p_{\text{top}} = 0$ is imposed at the top of the domain while inside the domain the fluid moves with a local fluid velocity with speed smoothing $\varsigma = 10^3$. As initial conditions, we consider a fluid at rest with hydrostatic pressure distribution,

$$\rho(0,\mathbf{x}) = 1, \qquad \mathbf{u}(0,\mathbf{x}) = \mathbf{0}, \qquad p(0,\mathbf{x}) = \frac{10^5}{\gamma} + g(0.6 - y), \qquad \mathbf{g} = (0,-g), \qquad g = 9.81. \tag{78}$$

This benchmark is solved employing the second order semi-implicit ALE hybrid method with ENO limiting and auxiliary numerical viscosity coefficient $c_\alpha = 2$. Besides, a Lax time dissipation between the staggered grids is applied over the new contributions of the transport stage at each time step. Three simulations are run addressing different models: the incompressible Navier-Stokes equations [43], the incompressible GPR model [38] and the fully compressible GPR model. Moreover, the GPR model has also been employed to solve the sloshing problem on a second inertial frame, assuming an horizontal convection of the geometry with $\mathbf{u}^g = (0.01, 0)^T$. All four simulations are run on an unstructured triangular mesh of 4072 primal elements up to time $t_e = 9$. The time series of the

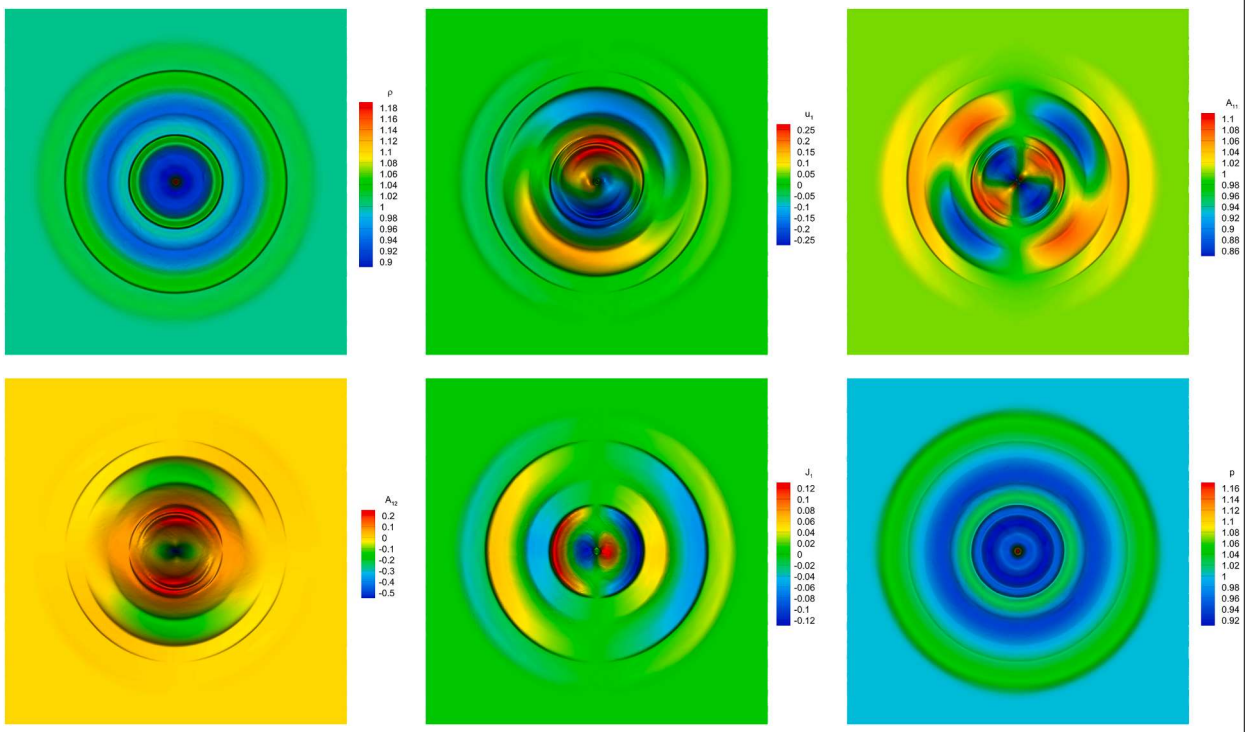

Fig. 25. Solid rotor. Contour plots for the density, u_1, A_{11}, A_{12}, J_1 and pressure fields at $t_e = 0.3$.

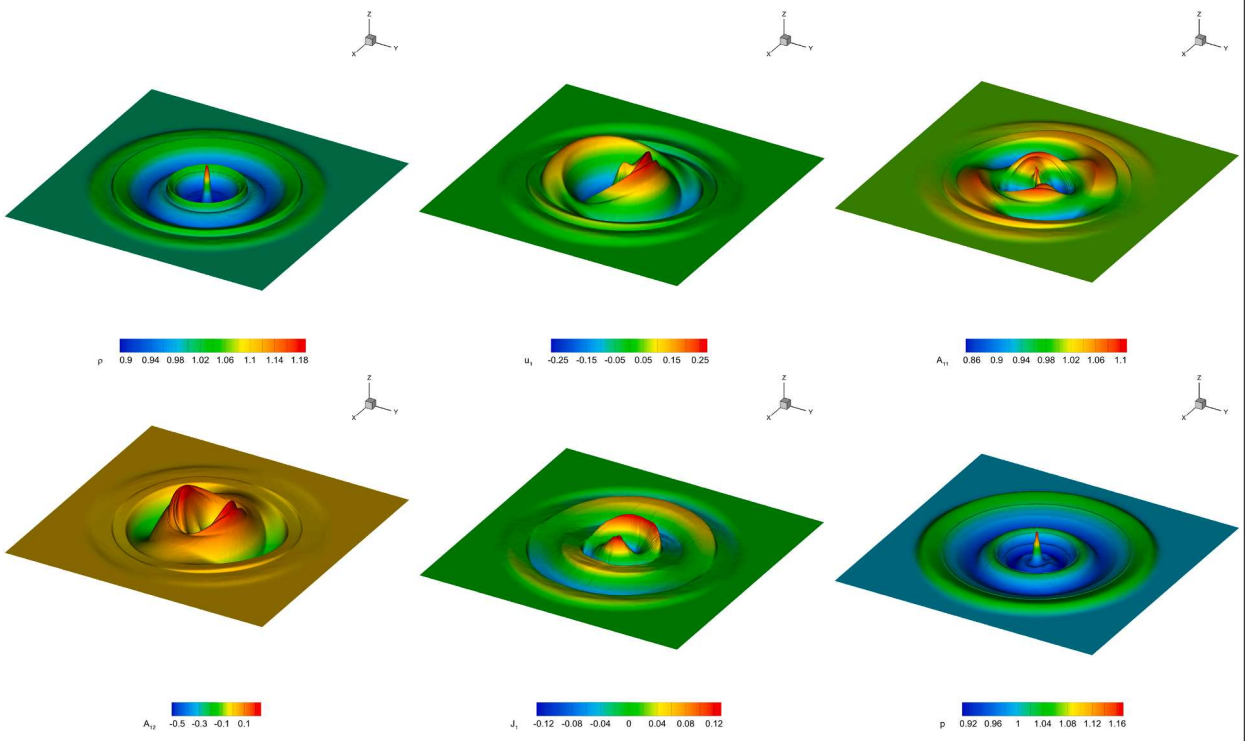

Fig. 26. Solid rotor. Elevated contour plots for the density, u_1, A_{11}, A_{12}, J_1 and pressure fields at $t_e = 0.3$.

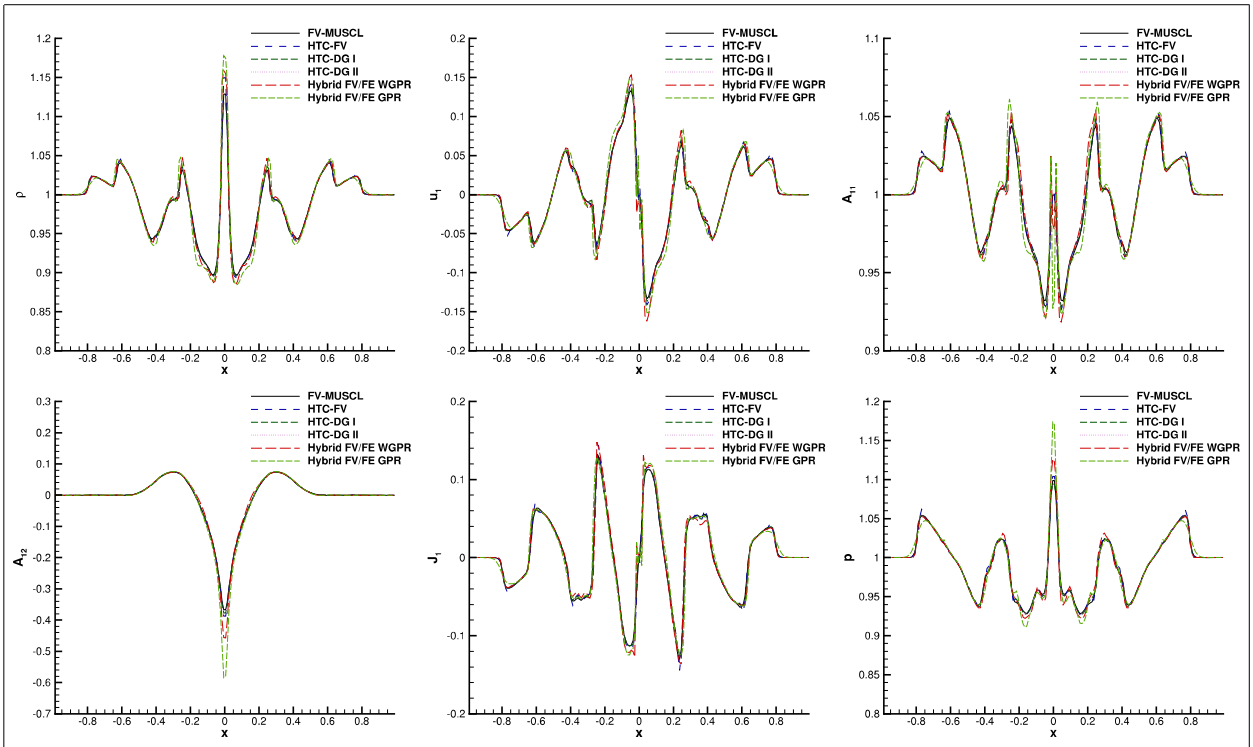

Fig. 27. Solid rotor. 1D comparative of the solution along the x-axis obtained using the new hybrid methodology for the compressible GPR model, the hybrid approach for weakly compressible medium [38], the FV and DG thermodynamically compatible schemes in [76] and the asymptotic-preserving FV-MUSCL method [36]. From left-top to right-bottom: density, u_1, A_{11}, A_{12}, J_1 and pressure.

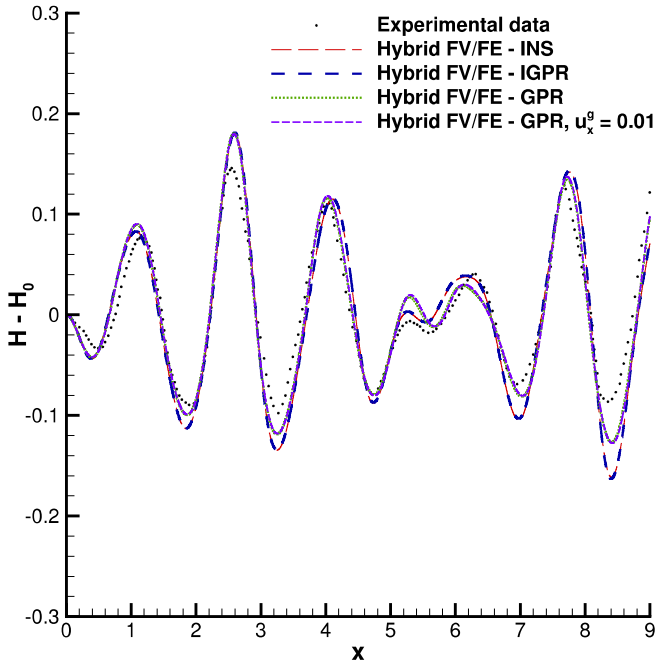

Fig. 28. Sloshing. Time series of the mesh surface elevation for the ALE hybrid method solving the compressible GPR model (green dotted line for $u_x^g = 0$, violet short dashed line for $u_x^g = 0.01$), the incompressible GPR model (blue dashed line) and the incompressible Navier-Stokes equations [43] (red dashed line) and experimental data from [100] (black circles). (For interpretation of the references to colour in this figure legend, the reader is referred to the web version of this article.)

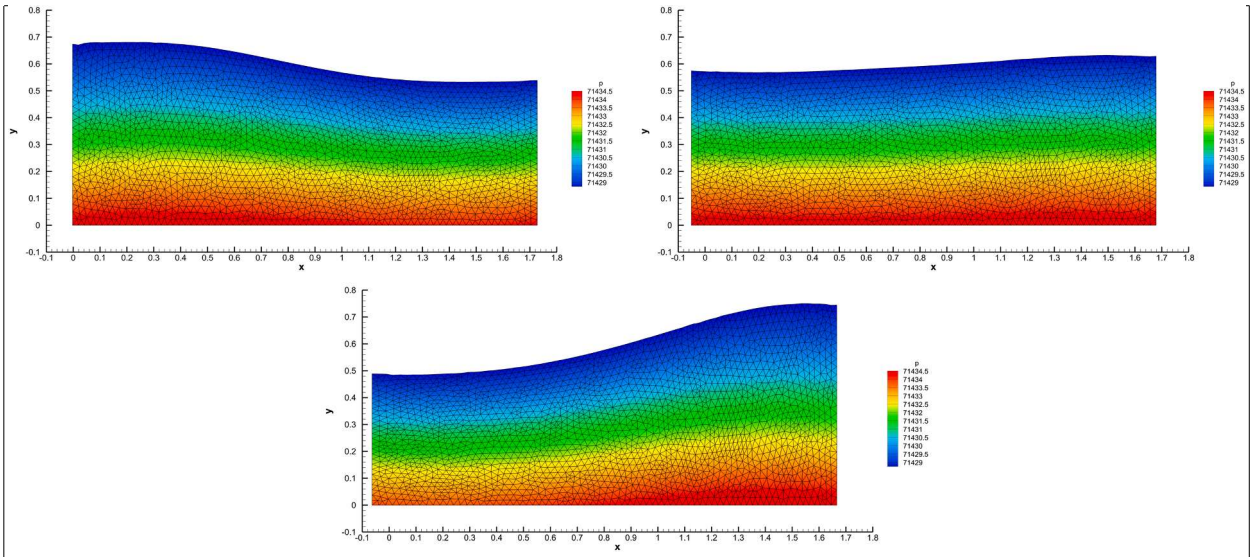

Fig. 29. Sloshing. Pressure contour plot and mesh deformation at times $t \in \{1.2, 2.14, 3.29\}$ (from top to bottom). Results obtained using the first order ALE hybrid FV/FE method for the GPR model with artificial viscosity $c_\alpha = 2$.

surface elevation of a point tracer initially located at $\mathbf{x} = (0.05, 0.6)$ is reported in Fig. 28. A good agreement is observed among the obtained solutions and with the experimental data from [100]. To further illustrate the obtained solutions and ease comparison with further references, as e.g. [43,101], several contour plots of the pressure and the mesh deformation computed using the GPR model are depicted in Fig. 29.

5. Conclusions

A novel semi-implicit direct arbitrary Lagrangian-Eulerian methodology has been presented for the numerical solution of the GPR model for continuum mechanics. Inspired by all Mach number methods and implicit-explicit techniques, a two-level operator splitting is introduced to decouple the computation of transport, pressure and potentially stiff relaxation source terms. The resulting subsystems are discretised through a hybrid approach which combines explicit finite volume methods for the transport subsystem and a continuous finite element method for the Poisson-type problem associated with the pressure field and for the Laplacian equation that may govern the mesh motion. The ODE subsystem related to the source terms is locally solved employing a Runge-Kutta scheme. This approach yields a time step restriction independent of the pressure waves allowing for a robust and computationally efficient treatment of the underlying physical processes able to deal with all Mach number media.

In addition, a thermodynamically compatible augmented GLM GPR model has been introduced, which significantly reduces errors associated with curl-type involutions. For demanding simulations in the solid limit, employing an exactly curl-free scheme may become essential. It should also be emphasised that the Galilean invariance of an ALE or Lagrangian numerical method solving the GPR model depends not only the conservative structure of the governing equations, addressed in the proposed methodology, but also on the geometric compatibility of the distortion and thermal impulse fields. Numerical violations of the curl-free constraints may introduce spurious frame-dependent contributions, resulting in a loss of Galilean invariance although in practice the current implementation demonstrates robustness across standard test cases.

A natural direction for future research is the development of exact involution-preserving discretisations exploiting the staggered grid structure [41], which would fully enforce the curl-free constraints while maintaining Galilean invariance. The preservation of additional structural properties, such as thermodynamic compatibility [25,76], will also be addressed.

The numerical results presented demonstrate the capability of the proposed methodology to accurately handle both solids and fluids at all Mach numbers. Future efforts will, therefore, focus on incorporating very high-order schemes, on employing alternative equations of state enabling the treatment of medium to large deformations [62,63], and on extending the methodology to fluid-structure iteration problems.

CRediT authorship contribution statement

S. Busto: Writing – review & editing, Writing – original draft, Visualization, Validation, Software, Methodology, Investigation, Funding acquisition, Formal analysis, Conceptualization.

Data availability

Data will be made available on request.

Declaration of competing interest

The authors declare the following financial interests/personal relationships which may be considered as potential competing interests:

Saray Busto reports financial support was provided by Spanish Ministry of Science, Innovation and Universities. Saray Busto reports financial support was provided by State Agency of Research. Saray Busto reports financial support was provided by European Commission. Saray Busto reports financial support was provided by Government of Galicia. If there are other authors, they declare that they have no known competing financial interests or personal relationships that could have appeared to influence the work reported in this paper.

Acknowledgements

The author acknowledges support from the Spanish Ministry of Science, Innovation and Universities (MCIN), the Spanish AEI (MCIN/AEI/10.13039/501100011033) and European Social Fund Plus under the project RYC2022-036355-I; from FEDER and the Spanish Ministry of Science, Innovation and Universities under project PID2021-122625OB-I00; from the European Research Council under the European Union's Horizon Europe research and innovation program grant ERC-2025-STG SUPREMUM 101219299, and from the Xunta de Galicia (Spain) under project GI-1563 ED431C 2025/09. The author would like to acknowledge support from the CESGA, Spain, for the access to the FT3 supercomputer. Views and opinions expressed are however those of the author only and do not necessarily reflect those of the granting authorities. Neither the European Union nor the granting authorities can be held responsible for them.

References

[1] S.K. Godunov, An interesting class of quasilinear systems, Dokl. Akad. Nauk SSSR 139(3) (1961) 521–523.
[2] S.K. Godunov, E.I. Romenskii, Nonstationary equations of nonlinear elasticity theory in Eulerian coordinates, J. Appl. Mech. Tech. Phy. 13 (6) (1972) 868–884.
[3] E.I. Romenski, Hyperbolic systems of thermodynamically compatible conservation laws in continuum mechanics, Math. Comput. Model. 28(10) (1998) 115–130.
[4] S.K. Godunov, E.I. Romenski, Nonstationary equations of the nonlinear theory of elasticity in Euler coordinates, J. Appl. Mech. Tech. Phy. 13 (1972) 868–885.
[5] S.K. Godunov, E.I. Romenski, Elements of Continuum Mechanics and Conservation Laws, Kluwer Academic/ Plenum Publishers, 2003.
[6] A.N. Malyshev, E.I. Romenski, Hyperbolic equations for heat transfer. Global solvability of the Cauchy problem, Sib. Math. J. 27 (1986) 734–740.
[7] I. Peshkov, E. Romenski, A hyperbolic model for viscous Newtonian flows, Continuum Mech. Therm. 28 (2016) 85–104.
[8] P.T. Barton, D. Drikakis, E.I. Romenski, An Eulerian finite-volume scheme for large elastoplastic deformations in solids, Int. J. Numer. Methods Eng. 81 (4) (2010) 453–484.
[9] M. Dumbser, I. Peshkov, E.I. Romenski, A Unified Hyperbolic Formulation for Viscous Fluids and Elastoplastic Solids, vol. 237, Springer International Publishing, 2018, pp. 451–463.
[10] H. Jackson, N. Nikiforakis, A numerical scheme for non-Newtonian fluids and plastic solids under the GPR model, J. Comput. Phys. 387 (2019) 410–429.
[11] E. Romenski, G. Reshetova, I. Peshkov, Thermodynamically compatible hyperbolic model of a compressible multiphase flow in a deformable porous medium and its application to wavefields modeling, AIP Conf. Proc. 2448 (1) (2021) 020019.
[12] I. Peshkov, M. Pavelka, E. Romenski, M. Grmela, Continuum mechanics and thermodynamics in the Hamilton and the Godunov-type formulations, Continuum Mech. Therm. 30 (6) (2018) 1343–1378.
[13] E.I. Romenski, Hyperbolic equations of Maxwell's nonlinear model of elastoplastic heat-conducting media, Sib. Math. 30 (1989) 606–625.
[14] M. Dumbser, I. Peshkov, E. Romenski, O. Zanotti, High order ADER schemes for a unified first order hyperbolic formulation of Newtonian continuum mechanics coupled with electro-dynamics, J. Comput. Phys. 348 (2017) 298–342.
[15] E. Romenski, I. Peshkov, M. Dumbser, F. Fambri, A new continuum model for general relativistic viscous heat-conducting media, Philos. Trans. R. Soc. Math. Phys. Eng. Sci. 378 (2170) (2020) 20190175.
[16] E.I. Romenski, A.D. Resnyansky, E.F. Toro, Conservative hyperbolic formulation for compressible two-phase flow with different phase pressures and temperatures, Q. Appl. Math. 65 (2) (2007) 259–279.
[17] E.I. Romenski, D. Drikakis, E.F. Toro, Conservative models and numerical methods for compressible two-phase flow, J. Sci. Comput. 42 (2010) 68–95.
[18] E. Romenski, G. Reshetova, I. Peshkov, Computational model for compressible two-phase flow in deformed porous medium, in: O. Gervasi, B. Murgante, S. Misra, C. Garau, I. Blečić, D. Taniar, B.O. Apduhan, A.M. A.C. Rocha, E. Tarantino, C.M. Torre (Eds.), Computational Science and Its Applications – ICCSA 2021, Springer International Publishing, 2021, pp. 224–236.
[19] E.I. Romenski, I. Peshkov, Thermodynamically compatible hyperbolic model for a two-phase compressible fluid flow with surface tension, Fluid Dyn. 58 (7) (2023) 1255–1265.
[20] L. Río-Martín, F. Dhaouadi, M. Dumbser, An exactly curl-free finite-volume/finite-difference scheme for a hyperbolic compressible isentropic two-phase model, J. Sci. Comput. 102 (1) (2025) 13.
[21] D. Ferrari, I. Peshkov, E. Romenski, M. Dumbser, A unified HTC multiphase model of continuum mechanics, J. Comput. Phys. 521 (2025) 113553.
[22] F. Dhaouadi, M. Dumbser, A first order hyperbolic reformulation of the Navier-Stokes-Korteweg system based on the GPR model and an augmented Lagrangian approach, J. Comput. Phys. 470 (2022) 111544.
[23] O. Kincl, I. Peshkov, M. Pavelka, V. Klika, Unified description of fluids and solids in smoothed particle hydrodynamics, Appl. Math. Comput. 439 (2023) 127579.
[24] S. Busto, M. Dumbser, I. Peshkov, E. Romenski, On thermodynamically compatible finite volume schemes for continuum mechanics, SIAM J. Sci. Comput. 44 (2022) A1723–A1751.
[25] S. Busto, M. Dumbser, A new class of simple, general and efficient finite volume schemes for overdetermined thermodynamically compatible hyperbolic systems, Commun. Appl. Math. Comput. 6 (3) (2024) 1742–1778. https://doi.org/10.1007/s42967-023-00307-4
[26] W. Boscheri, M. Dumbser, R. Loubère, Cell centered direct Arbitrary-Lagrangian-Eulerian ADER-WENO finite volume schemes for nonlinear hyperelasticity, Comput. Fluids 134–135 (Supplement C) (2016) 111–129.
[27] M. Dumbser, I. Peshkov, E. Romenski, O. Zanotti, High order ADER schemes for a unified first order hyperbolic formulation of continuum mechanics: viscous heat-conducting fluids and elastic solids, J. Comput. Phys. 314 (2016) 824–862.

[28] S. Busto, S. Chiocchetti, M. Dumbser, E. Gaburro, I. Peshkov, High order ADER schemes for continuum mechanics, Front. Phys. 8 (2020) 32.
[29] J.H. Park, C.D. Munz, Multiple pressure variables methods for fluid flow at all Mach numbers, Int. J. Numer. Methods Fluids 49 (8) (2005) 905–931.
[30] P. Degond, M. Tang, All speed scheme for the low Mach number limit of the isentropic Euler equations, Comm. Comput. Phys. 10 (1) (2011) 1–31.
[31] E.F. Toro, M.E. Vázquez-Cendón, Flux splitting schemes for the Euler equations, Comput. Fluids 70 (2012) 1–12.
[32] M. Tavelli, M. Dumbser, A pressure-based semi-implicit space-time discontinuous Galerkin method on staggered unstructured meshes for the solution of the compressible Navier-Stokes equations at all Mach numbers, J. Comput. Phys. 341 (2017) 341–376.
[33] S. Busto, L. Río-Martín, M.E. Vázquez-Cendón, M. Dumbser, A semi-implicit hybrid finite volume / finite element scheme for all Mach number flows on staggered unstructured meshes, Appl. Math. Comput. 402 (2021) 126117.
[34] A. Thomann, G. Puppo, C. Klingenberg, An all speed second order IMEX relaxation schemefor the Euler equations, J. Comput. Phys. 420 (2020) 109723.
[35] W. Boscheri, S. Busto, M. Dumbser, An all Mach number semi-implicit hybrid finite volume/virtual element method for compressible viscous flows on Voronoi meshes, Comput. Method. Appl. M. 433 (2025) 117502.
[36] W. Boscheri, M. Dumbser, M. Ioriatti, I. Peshkov, E. Romenski, A structure-preserving staggered semi-implicit finite volume scheme for continuum mechanics, J. Comput. Phys. 424 (2021) 109866.
[37] I. Peshkov, M. Dumbser, W. Boscheri, E. Romenski, S. Chiocchetti, M. Ioriatti, Simulation of non-Newtonian viscoplastic flows with a unified first order hyperbolic model and a structure-preserving semi-implicit scheme, Comput. Fluids 224 (2021) 104963.
[38] S. Busto, L. Río-Martín, Semi-implicit hybrid finite volume/finite element method for the GPR model of continuum mechanics, J. Sci. Comput. 102 (2) (2025) 49.
[39] A. Lucca, S. Busto, M. Dumbser, An implicit staggered hybrid finite volume/finite element solver for the incompressible Navier-Stokes equations, East Asian J. Appl. Math. 13 (2023) 671–716.
[40] S. Busto, M. Dumbser, A staggered semi-implicit hybrid finite volume / finite element scheme for the shallow water equations at all Froude numbers, Appl. Numer. Math. 175 (2022) 108–132.
[41] F. Fambri, E. Zampa, S. Busto, L. Río-Martín, F. Hindenlang, E. Sonnendrücker, M. Dumbser, A well-balanced and exactly divergence-free staggered semi-implicit hybrid finite volume/finite element scheme for the incompressible MHD equations, J. Comput. Phys. 493 (2023) 112493.
[42] E. Zampa, S. Busto, M. Dumbser, A divergence-free hybrid finite volume/finite element scheme for the incompressible MHD equations based on compatible finite element spaces with a posteriori limiting, Appl. Numer. Math. 198 (2024) 346–374.
[43] S. Busto, M. Dumbser, L. Río-Martín, Semi-implicit hybrid finite volume/finite element method for the GPR model of continuum mechanics, Appl. Math. Comput. 437 (2023) 127539.
[44] W. Boscheri, S. Chiocchetti, I. Peshkov, A cell-centered implicit-explicit Lagrangian scheme for a unified model of nonlinear continuum mechanics on unstructured meshes, J. Comput. Phys. 451 (2022) 110852.
[45] W. Boscheri, M. Dumbser, R. Loubère, P.H. Maire, A structure-preserving and thermodynamically compatible cell-centered Lagrangian finite volume scheme for continuum mechanics, ArXiV preprint (2025).
[46] J. von Neumann, R.D. Richtmyer, A method for the calculation of hydrodynamics shocks, J. Appl. Phys. 21 (1950) 232–237.
[47] S.K. Sambasivan, M.J. Shashkov, D.E. Burton, A finite volume cell-centered Lagrangian hydrodynamics approach for solids in general unstructured grids, Int. J. Numer. Meth. Fl. 72 (2013) 770–810.
[48] P.H. Maire, R. Abgrall, J. Breil, J. Ovadia, A cell-centered Lagrangian scheme for two-dimensional compressible flow problems, SIAM J. Sci. Comput. 29 (2007) 1781–1824.
[49] G. Carré, S.D. Pino, B. Després, E. Labourasse, A cell-centered Lagrangian hydrodynamics scheme on general unstructured meshes in arbitrary dimension, J. Comput. Phys. 228 (2009) 5160–5183.
[50] N.M. Atallah, V.Z. Tomov, G. Scovazzi, Weak boundary conditions for Lagrangian shock hydrodynamics: a high-order finite element implementation on curved boundaries, J. Comput. Phys. 507 (2024) 112959.
[51] M. Berndt, J. Breil, S. Galera, M. Kucharik, P.H. Maire, M. Shashkov, Two-step hybrid conservative remapping for multimaterial arbitrary Lagrangian–Eulerian methods, J. Comput. Phys. 230 (17) (2011) 6664–6687.
[52] W. Boscheri, M. Dumbser, Arbitrary-Lagrangian-Eulerian one-step WENO finite volume schemes on unstructured triangular meshes, Commun. Comput. Phys. 14 (2013) 1174–1206.
[53] E. Gaburro, A unified framework for the solution of hyperbolic PDE systems using high order direct Arbitrary-Lagrangian-Eulerian schemes on moving unstructured meshes with topology change, Arch. Comput. Method. E. 28 (2021) 1249–1321.
[54] W. Boscheri, M. Ciallella, High order treatment of moving curved boundaries: arbitrary-Lagrangian-Eulerian methods with a shifted boundary polynomial correction, J. Comput. Phys. 539 (2025) 114215.
[55] P.L. Tallec, J. Mouro, Fluid structure interaction with large structural displacements, Comput. Method. Appl. M. 190 (2001) 3039–3067.
[56] F. Nobile, C. Vergara, An effective fluid-structure interaction formulation for vascular dynamics by generalized Robin conditions, SIAM J. Sci. Comput. 30 (2008) 731–763.
[57] J. Cesenek, M. Feistauer, J. Horacek, V. Kucera, J. Prokopova, Simulation of compressible viscous flow in time-dependent domains, Appl. Math. Comput. 219 (2013) 7139–7150.
[58] C.D. Munz, P. Omnes, R. Schneider, E. Sonnendrücker, U. Voss, Divergence correction techniques for maxwell solvers based on a hyperbolic model, J. Comput. Phys. 161 (2000) 484–511.
[59] S. Busto, M. Dumbser, C. Escalante, S. Gavrilyuk, N. Favrie, On high order ADER discontinuous Galerkin schemes for first order hyperbolic reformulations of nonlinear dispersive systems, J. Sci. Comput. 87 (2021) 48.
[60] S. Busto, M. Dumbser, A new thermodynamically compatible finite volume scheme for magnetohydrodynamics, SIAM J. Numer. Anal. 61 (2023) 1.
[61] H. Jackson, A fast numerical scheme for the Godunov-Peshkov-Romenski model of continuum mechanics, J. Comput. Phys. 348 (2017) 514–533.
[62] N. Favrie, S. Gavrilyuk, S. Ndanou, A thermodynamically compatible splitting procedure in hyperelasticity, J. Comput. Phys. 270 (2014) 300–324.
[63] S. Gavrilyuk, S. Ndanou, S. Hank, One-parameter family of equations of state for isotropic compressible solids, J. Elast. 124 (2016) 133–141.
[64] S.K. Godunov, Symmetric form of the equations of magnetohydrodynamics, Numer. Methods Mech. Continuous Media 3 (1) (1972) 26–34.
[65] K.G. Powell, An Approximate Riemann Solver for Magnetohydrodynamics (That Works in More Than One Dimension), Technical Report NASA-CR-194902 NAS 1.26:194902, Institute for Computer Applications in Science and Engineering (ICASE), 1994.
[66] K.G. Powell, P.L. Roe, T.J. Linde, T.I. Gombosi, D.L. De Zeeuw, A solution-adaptive upwind scheme for ideal magnetohydrodynamics, J. Comput. Phys. 154 (2) (1999) 284–309.
[67] S. Chiocchetti, I. Peshkov, S. Gavrilyuk, M. Dumbser, High order ADER schemes and GLM curl cleaning for a first order hyperbolic formulation of compressible flow with surface tension, J. Comput. Phys. 426 (2021) 109898.
[68] J.M. Hyman, M. Shashkov, Natural discretizations for the divergence, gradient, and curl on logically rectangular grids, Comput. Math. Appl. 33 (1997) 81–104.
[69] R. Jeltsch, M. Torrilhon, On curl-preserving finite volume discretizations for shallow water equations, BIT Numer. Math. 46 (Supplement 1) (2006) S35–S53.
[70] M. Dumbser, S. Chiocchetti, I. Peshkov, On numerical methods for hyperbolic PDE with curl involutions, in: O. Bokhove, et al. (Eds.), Continuum Mechanics, Applied Mathematics and Scientific Computing: Godunovś Legacy, Springer International Publishing, 2020, pp. 125–134.
[71] D.S. Balsara, R. Käppeli, W. Boscheri, M. Dumbser, Curl constraint-preserving reconstruction and the guidance it gives for mimetic scheme design, Commun. Appl. Math. Comput. 5 (1) (2023) 235–294.
[72] A. Dedner, F. Kemm, D. Kröner, C.-D. Munz, T. Schnitzer, M. Wesenberg, Hyperbolic divergence cleaning for the MHD equations, J. Comput. Phys. 175 (2002) 645–673.
[73] M. Dumbser, F. Fambri, E. Gaburro, A. Reinarz, On GLM curl cleaning for a first order reduction of the CCZ4 formulation of the Einstein field equations, J. Comput. Phys. 404 (2020) 109088.

[74] D. Derigs, A.R. Winters, G.J. Gassner, S. Walch, M. Böhm, Ideal GLM-MHD: about the entropy consistent nine-wave magnetic field divergence diminishing ideal magnetohydrodynamics equations, J. Comput. Phys. 364 (2018) 420–467.
[75] I. Peshkov, E. Romenski, M. Dumbser, Continuum mechanics with torsion, Continuum Mech. Therm. 31 (5) (2019) 1517–1541.
[76] R. Abgrall, S. Busto, M. Dumbser, A simple and general framework for the construction of thermodynamically compatible schemes for computational fluid and solid mechanics, Appl. Math. Comput. 440 (2023) 127629.
[77] A. Bermúdez, J.L. Ferrín, L. Saavedra, M.E. Vázquez-Cendón, A projection hybrid finite volume/element method for low-Mach number flows, J. Comput. Phys. 271 (2014) 360–378.
[78] S. Busto, J.L. Ferrín, E.F. Toro, M.E. Vázquez-Cendón, A projection hybrid high order finite volume/finite element method for incompressible turbulent flows, J. Comput. Phys. 353 (2018) 169–192.
[79] A. Bermúdez, S. Busto, M. Dumbser, J.L. Ferrín, L. Saavedra, M.E. Vázquez-Cendón, A staggered semi-implicit hybrid FV/FE projection method for weakly compressible flows, J. Comput. Phys. 421 (2020) 109743.
[80] L. Río-Martín, S. Busto, M. Dumbser, A massively parallel hybrid finite volume/finite element scheme for computational fluid dynamics, Mathematics 9 (2021) 2316.
[81] A. Bermúdez, A. Dervieux, J.A. Desideri, M.E. Vázquez-Cendón, Upwind schemes for the two-dimensional shallow water equations with variable depth using unstructured meshes, Comput. Methods Appl. Mech. Eng. 155 (1) (1998) 49–72.
[82] M. Tavelli, M. Dumbser, A staggered space-time discontinuous Galerkin method for the three-dimensional incompressible Navier-Stokes equations on unstructured tetrahedral meshes, J. Comput. Phys. 319 (2016) 294–323.
[83] E. Gaburro, W. Boscheri, S. Chiocchetti, C. Klingenberg, V. Springel, M. Dumbser, High order direct Arbitrary-Lagrangian-Eulerian schemes on moving Voronoi meshes with topology changes, J. Comput. Phys. 407 (2020) 109167.
[84] E. Gaburro, High order well-balanced Arbitrary-Lagrangian-Eulerian ADER discontinuous Galerkin schemes on general polygonal moving meshes, Comput. Fluids 301 (2025) 106764.
[85] C. Farhat, P. Geuzainne, C. Grandmont, The discrete geometric conservation law and the nonlinear stability of ALE schemes for the solution of flow problems on moving grids, J. Comput. Phys. 174 (2001) 669–694.
[86] W. Boscheri, M. Dumbser, A direct Arbitrary-Lagrangian-Eulerian ADER-WENO finite volume scheme on unstructured tetrahedral meshes for conservative and non-conservative hyperbolic systems in 3D, J. Comput. Phys. 275 (2014) 484–523.
[87] C. Parés, Numerical methods for nonconservative hyperbolic systems: a theoretical framework, SIAM J. Numer. Anal. 44 (2006) 300–321.
[88] V.V. Rusanov, The calculation of the interaction of non-stationary shock waves and obstacles, USSR Computat. Math. Math. Phys. 1 (1962) 304–320.
[89] V. Springel, E pur si muove: Galilean-invariant cosmological hydrodynamical simulations on a moving mesh, Mon. Not. R. Astron. Soc. 401 (2) (2010) 791–851.
[90] E.F. Toro, R.C. Millington, L.A.M. Nejad, Godunov Methods, Springer, 2001, pp. 907–940.
[91] S. Busto, E.F. Toro, M.E. Vázquez-Cendón, Design and analisis of ADER–type schemes for model advection–diffusion–reaction equations, J. Comput. Phys. 327 (2016) 553–575.
[92] I.G. Petrovskii, Partial Differential Equations, London Iliffe Books Ltd., 1967.
[93] E.F. Toro, Riemann Solvers and Numerical Methods for Fluid Dynamics: A Practical Introduction, Springer, 2009.
[94] P. Roe, Approximate riemann solvers, parameter vectors, and difference schemes, J. Comput. Phys. 43 (1981) 357–372.
[95] L. Pareschi, G. Russo, Implicit–explicit Runge–Kutta schemes and applications to hyperbolic systems with relaxation, J. Scien. Comput. 25 (2005) 129–155.
[96] G. Scovazzi, A discourse on Galilean invariance, SUPG stabilization, and the variational multiscale framework, Comput. Method. Appl. M. 196 (2007) 1108–1132.
[97] P. Woodward, P. Colella, The numerical simulation of two-dimensional fluid flow with strong shocks, J. Comput. Phys. 54 (1984) 115–173.
[98] M. Dumbser, E.F. Toro, On universal Osher-type schemes for general nonlinear hyperbolic conservation laws, Commun. Comput. Phys. 10 (3) (2011) 635–671.
[99] U. Ghia, K.N. Ghia, C.T. Shin, High-Re solutions for incompressible flow using the Navier-Stokes equations and a multigrid method, J. Comput. Phys. 48 (3) (1982) 387–411.
[100] O. Faltinsen, O. Rognebakke, I.L. n.A. Timokha, Adaptive multimodal approach to nonlinear sloshing in a rectangular tank, J. Fluid Mech. 407 (2000) 201–234.
[101] M. Dumbser, W. Boscheri, High-order unstructured Lagrangian one–step WENO finite volume schemes for non–conservative hyperbolic systems: applications to compressible multi–phase flows, Comput. Fluids 86 (2013) 405–432.